Master's thesis

NTNU
Norwegian University of Science and Technology
Faculty of Natural Sciences
Department of Physics

Tone Alsvik Finstad

Modeling of Temperature for Mono- and Bifacial Photovoltaics in Nordic Conditions

Master's thesis in Applied Physics and Mathematics
Supervisor: Magnus Moe Nygård
Co-supervisor: Turid Reenaas
June 2025

NTNU
Norwegian University of Science and Technology

IFE Institute for Energy Technology

Tone Alsvik Finstad

Modeling of Temperature for Mono- and Bifacial Photovoltaics in Nordic Conditions

Master's thesis in Applied Physics and Mathematics
Supervisor: Magnus Moe Nygård
Co-supervisor: Turid Reenaas
June 2025

Norwegian University of Science and Technology
Faculty of Natural Sciences
Department of Physics

NTNU
Norwegian University of
Science and Technology

ABSTRACT

The aim of this thesis was to study the performance of commonly used temperature models for photovoltaic (PV) modules, and perform further model development to enhance the performance of the models for applications in a Nordic climate. The temperature models are commonly used in energy yield estimations, especially in the design phase, as the temperature greatly affects the performance. All testing and parameter tuning were performed for two outdoor PV test sites that are located in different climates, at Kjeller and Gålå, Norway. The datasets contain 5 different monofacial modules, as well as three different bifacial modules. First, an evaluation of the accuracy of existing models with their default parameters was performed, as this is a common practice in the industry today. A selection of models is readily available through the open-source Python library `pvlib`, and the following models for module temperature were studied: (1) Sandia Array Performance Model, (2) Fuentes, (3) Faiman, and (4) Faiman with a radiative loss term. Additionally, the following cell temperature models were studied: (5) PVsyst and (6) Ross.

This uncovered that for our two test sites, there is a clear positive bias in the models, which we believe is due to the default parameters being determined for older PV modules installed in PV test sites in climates different from the Nordic. The existing model performing the best was the Fuentes model, which is the only model not empirically determined by test sites in other climates. We therefore wanted to see whether a simple parameter tuning using data from the two test sites could improve the empirical models to perform as well as, or even better than, the more complex Fuentes model. As we showed that the Sandia model, the PVsyst model, and the Faiman model were nearly equivalent models; only the Faiman model was tuned. Additionally, tuning was performed for the Faiman model with a radiative term, which accounts for a radiative loss to the sky. The model parameters were tuned with different subsets of the timeseries to investigate the influence of climate, site, and module technology on the results. It was found that all parameters gave a significant improvement compared to the default models. For instance, for the models tuned and tested for daytime data, the Faiman model with a radiative term with default parameters had a mean RMSE of 5.58 °C and a mean |MBE| of 3.87 °C when averaged over all modules, while with climate-specific parameters, the model had a mean RMSE of 2.24 °C and a mean |MBE| of 1.03 °C. As expected, the module-specific parameters generally had the best performance, but were often closely followed by the other tuned parameters. The results did not show a clear advantage of using either site- or bifacial-specific parameters, however, further investigation is encouraged. However, the results for a climate-specific model were promising, and parameters based on measurements from the two PV test sites were proposed.

SAMMENDRAG

Målet med denne masteroppgaven var å undersøke hvor godt eksisterende temperaturmodeller for fotovoltaiske (PV) moduler fungerer, og å videreutvikle modellene for å forbedre deres nøyaktighet under nordiske forhold. Temperaturmodellene brukes ofte i estimater av energiproduksjon, ofte i designfasen av PV-systemer, da temperatur påvirker modulenes ytelse i stor grad. All testing og parametertilpasning ble gjennomført ved bruk av to utendørs testanlegg for PV i ulike klimasoner i Norge, på Kjeller og Gålå. Datasettene inneholder data fra 5 ulike monofacial-moduler, og 3 ulike bifacial-moduler. Først ble eksisterende modeller med sine standardparametere evaluert for de to testanleggene, da bruk av standardparametere er vanlig i solcellebransjen i dag. Et utvalg modeller er tilgjengelig gjennom Python-biblioteket `pvlib`, og følgende modeller for modultemperatur ble testet: (1) Sandia Array Performance Model (SAPM), (2) Fuentes, (3) Faiman og (4) Faiman med et strålingsledd. I tillegg ble følgende modeller for celletemperatur studert: (5) Pvsyst og (6) Ross, da modul- og celletemperatur ofte antas å være sammenlignbare.

For våre to testsystemer så vi en tydelig positiv bias i modellen, antatt å skyldes at standardparametrene er tilpasset målinger fra testsystemer i svært annerledes klimaer. Av de eksisterende modellene presterte Fuentes-modellen best, som er en eneste modellen som ikke er empirisk tilpasset for testsystemer i andre klimaer. Det var derfor ønskelig å se om en enkel parametertilpasning ved bruk av data fra de to testsystemene i Norge kunne forbedre de empiriske modellene til å yte like godt eller bedre enn den mer komplekse Fuentesmodellen. Da det ble vist at SAPM, PVsyst og Faiman var tre tilnærmet ekvivalente modeller, ble kun Faiman-modellen tatt med i parametertilpasningen. I tillegg ble Faiman-modellen med et strålingsledd tatt med, som tar høyde for et strålingstap til atmosfæren. Klima-, steds-, modul- og bifacialspesifikke parametere ble tilpasset for hver modell og testet for alle moduler. Alle disse parameterene ga en betydelig forbedring i forhold til modellenes standardparametere. For eksempel, for modellene som kun er tilpasset og testet på dagtidsdata, hadde Faiman-modellen med et strålingsledd en gjennomsnittlig RMSE på 5.58 °C og en gjennomsnittlig |MBE| på 3.87 °C for alle moduler med standardparametrene. Med klima-spesifikke parametere forbedret modellen seg til en gjennomsnittlig RMSE på 2.24 °C og en gjennomsnittlig |MBE| på 1.03 °C. De modulspesifikke parametrene ga generelt de best resultatene, men var ofte tett fulgt av de andre tilpassede parameterene. Resultatene viste ingen klare fordeler ved bruk av steds- og bifacialspesifikke parametere, men det oppfordres til videre undersøkelser rundt dette. Derimot, viste resultatene tydelig at et generelt sett med klimaspesifikke parametre for Norden er lovende, og parametere basert på målinger fra de to testsystemene ble foreslått.

PREFACE

This thesis marks the completion of my MSc. degree in Applied Physics at The Norwegian University of Natural Science (NTNU). The thesis was carried out at the Department of Physics in collaboration with the Institute for Energy Technology (IFE). This thesis builds on the project thesis *Modeling of temperature for mono- and bifacial photovoltaics in Nordic conditions* completed in the fall of 2024 by the same author.

I would like to thank my supervisor, Magnus Moe Nygård (IFE), for invaluable guidance and thorough feedback throughout the whole year. His dedication and commitment have been greatly appreciated. I also want to extend my thanks to Mari Øgaard (IFE) for her valuable input and insightful discussions during the course of my work. Both Magnus and Mari have made the collaboration with IFE seamless, despite the geographical distance from Trondheim. I also want to thank my supervisor at NTNU, Turid Reenaas, for her guidance and feedback on my work on both the project and master's thesis.

A special thanks goes to all my friends who have made these years in Trondheim and Padova unforgettable. These years have been full of great experiences that I would not be without. Additionally, I want to thank my teammates in NTNUI volleyball for providing a much-needed break from academic life, and for all the fun experiences.

Last but not least, I am deeply thankful to my family for their support and encouragement.

CONTENTS

LIST OF FIGURES

LIST OF TABLES

ABBREVIATIONS AND SYMBOLS

Abbreviations

List of all abbreviations in alphabetical order:

- **PV** Photovoltaics
- **PERC** Passivated Emitter and Rear Contact
- **IBC** Interdigitated Back Contact
- **HIT** Heterojunction with Intrinsic Thin Layer
- **POA** Plane of array
- **MPP** Maximum power point
- **SAPM** Sandia Array Performance Model
- **RMSE** Root Mean Square Error
- **MBE** Mean Bias Error
- **GHI** Global Horizontal Irradiance
- **GTI** Global Tilted Irradiance
- **GVI** Global Vertical Irradiance
- **GRI** Global Reflected Irradiance
- **DNI** Direct Normal Irradiance
- **DHI** Diffuse Horizontal irradiance

Nomenclature

T_m - Module temperature [°C]
T_c - Cell temperature [°C]
T_a - Ambient temperature [°C]
v - Wind speed [m/s]
G_{poa} - Plane of array irradiance [W/m^2]
G - Global horizontal irradiance [W/m^2]
G_{dh} - Diffuse horizontal irradiance [W/m^2]
G_{dn} - Direct normal irradiance [W/m^2]

CHAPTER

ONE

INTRODUCTION

1.1 Background and motivation

Globally, 2024 was the warmest year on record, with a mean near-surface temperature exceeding the pre-industrial conditions (1850–1900 average) by 1.55 °C ± 0.13 °C [1]. In 2023, the atmospheric levels of carbon dioxide, methane, and nitrous oxide reached the highest levels in the last 800,000 years, and increased further in 2024 [1]. In recent years, record highs have also been recorded in sea surface temperatures, mean sea levels, and negative glacier mass balance [1]. Thus, we are already seeing significant consequences of global warming. To prevent the most severe impacts of climate change, global emissions should be reduced to almost half by 2030, and reach net-zero by 2050 [2]. In order to achieve this, the use of fossil fuels needs to be reduced, and renewable energy sources, such as solar power, wind energy, and hydropower, need to be utilized further. Renewables are predicted to account for close to half of the global electricity generation by 2030, with the share of wind and solar photovoltaics (PV) expected to double to 30% [3]. Solar PV is predicted to become the largest renewable energy source by the end of the decade, surpassing both wind and hydropower [3]. The Norwegian Parliament has adopted a target of reaching 8 TWh of solar energy by 2030 [4]. As of April 2025, Norway has solar power installations with an installed capacity of 800 MWp, which corresponds to around 0.6 TWh of annual production [5]. A target of 8 TWh of solar power generation in Norway implies that solar installations with an installed capacity of approximately 10,000 MWp must be developed [4]. This suggests an expansion of more than 12 times the current level over the next five years. Most current installations in Norway today are roof-mounted PV, however, there is an increasing interest in the development of utility-scale ground-mounted PV [4]. These will be important in order for Norway to reach the goal of 8 TWh, and are the main focus of this thesis.

This expansion of solar energy production requires good energy yield estimations in both the planning phase and for production forecasting. The power production is primarily dependent on the plane-of-array (POA) irradiance, but also on the operating temperature of the module [6]. Thus, these estimations rely on temperature measurements or accurate temperature estimation models. In the industry today, it is common to use simple empirical models, where the parameters have been adjusted to measurements performed for a single PV test site. The test sites are often located in vastly different climates from the Nordic climate, yet they are used for Nordic PV

systems without any adaptation. As an example, the Faiman model was developed using a PV test site in the Negev desert in Israel [7]. The values tuned for this test site in a hot desert climate, with minimal precipitation and a mean annual temperature of over 18 °C, are used all over the globe today [8]. This includes the Nordic countries, where we have snow, warm temperate, and polar climate zones [9]. Other empirical models, like the Sandia Array Performance model and the PVsyst model, are also tuned using data from PV test sites in specific climate zones. As none of these are developed for the Nordic climate, we want to evaluate these for PV test sites in a Nordic climate, and explore the possibilities of improving their performance by developing a climate-specific model. In the author's previous specialization project, where the existing empirical models were evaluated for a test site at IFE, Kjeller, there appeared to be a clear bias in the models, as they all tended to overestimate the temperature, possibly due to the big differences in climate factors like the irradiance, temperature, humidity, and wind [10].

1.2 Research definition

This thesis aims to evaluate existing temperature models using data from outdoor PV test sites in a Nordic climate and to explore further model development. To evaluate the existing models further, the analysis performed for the Kjeller test site in the specialization project will be repeated for a PV test site at Gålå. The test sites consist of a variety of rack-mounted PV modules, including both monofacial and bifacial types. To improve the models, the model parameters will be tuned using data from the two PV test sites. This will be done for the Faiman model with and without an additional radiative term. We want to explore the opportunity of creating a climate-specific set of parameters for the Nordic climate, for use for PV test sites located all over the Nordic countries, and possibly other areas with similar climates, like Alaska, Canada, Russia, etc [9]. In addition, we will explore whether site- and module-specific parameters will increase the performance further. As there are bifacial modules at both PV test sites, a set of bifacial-specific parameters will also be tuned and evaluated. Additionally, a small analysis on the effect of incorporating backside irradiance for the bifacial modules during tuning and testing will be performed. An additional analysis on the effect of removing nightly values in the tuning will be performed, as well as an evaluation of the effect of improving the temperature model on DC power estimations.

1.3 Structure of the thesis

The thesis is structured as follows: The relevant background theory for the thesis is presented in Chapter 2, before the methods and tools used in the thesis are explained in Chapter 3. Chapter 4 presents the relevant results from the author's previous work in the project thesis, for completeness, as the thesis is a natural continuation of this work. All results, as well as discussion and interpretation of the results, are presented in Chapter 5. Chapter 6 concludes the work and results, and suggestions on further work that can be done on the topic are presented in Chapter 7. There are also appendices with links to the GitHub repositories for the thesis and project thesis work, and additional relevant results.

CHAPTER

TWO

THEORY

This chapter presents the relevant background theory for the project. In the project, module temperature measurements are used, as this is more convenient to measure than cell temperature. However, in the theory describing the relation between the module's effectivity and temperature, this description involves the cell temperature. As the temperature of the cell and the temperature of the back surface of the modules can differ, this is worth noticing. Sections 2.1, 2.2.4 and 2.3.1–2.3.6, are adapted from the authors' specialization project [10].

2.1 Photovoltaic (PV) Technology

2.1.1 Solar cells

A solar cell is a device that converts solar energy directly into electric energy. Conventional solar cells consist of a semiconductor wafer, with electrodes attached to it. Figure 2.1.1 shows a simplified visualization of a solar cell. The semiconductor absorbs photons from the sunlight, transferring the photon energy to valence electrons, and exciting them to the conduction band. For this to occur, the photon energy needs to be larger than the bandgap of the semiconductor. The photovoltage pulls the excited electrons out of the cell and into a circuit, and a built-in electric field prevents them from de-exciting to the valence band. This electric field can be created by a pn-junction, meaning that we have one p-doped and one n-doped layer in our semiconductor wafer [12]. N-doped materials have an increased number of available electrons, for instance, due to the addition of an element with an extra electron, such as Phosphorus. P-type materials have an increased number of holes present, for example, due to the addition of Boron, which has fewer electrons.

Traditional solar cells are made with a silicon wafer and a screen-printed full-area aluminum layer in contact with the complete back surface of the silicon [13]. The recombination of photo-generated charge carriers at the rear contact with the aluminum is marginally suppressed by the local aluminum doping of the wafer surface, called the aluminum back-surface field [13]. Additionally, the aluminum layer partly absorbs the infrared light, which reduces the light absorption of the solar cell. These two loss mechanisms cause the efficiency of traditional silicon solar cells to be limited to around 20% [13].

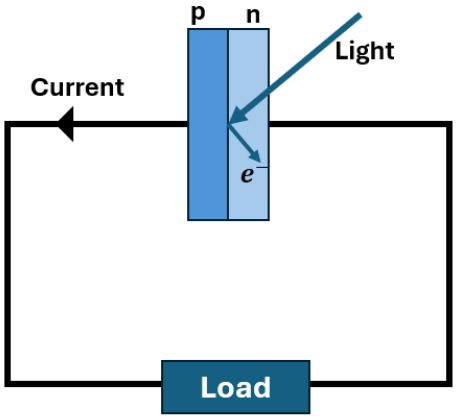

Figure 2.1.1: Simple visualization of the operation of a solar cell. The left layer is a p-type semiconductor, and the right layer is n-type. Figure created by the author, inspired by [11]

Silicon p-type Passivated Emitter and Rear Contact (PERC) solar cells, are an upgraded iteration of these traditional solar cells, which can produce 6 to 12% more energy [13]. The PERC solar cell technology includes a dielectric surface passivation layer that reduces the charge carrier surface recombination. In addition, the PERC solar cell reduces the semiconductor-metal area of contact, and increases the internal rear reflectivity by including a dielectrically displaced rear metal reflector [14].

The Interdigitated Back Contact (IBC) solar cell technology has all metal contacts on the rear end of the cell, leaving the front surface free from any shading materials [15]. The main layer of the cell is the n- or p-type crystalline silicon (c-Si) wafer functioning as an absorber layer. An anti-reflective and passivation layer is placed on one or both sides of the cell. A modification for IBC cells is the addition of a diffusion layer, featuring interdigitated n-type and p-type layers allowing for installation of all metal contacts on the rear end of the cell [15].

The Heterojunction with Intrinsic Thin-layer (HIT) solar cells consist of an intrinsic amorphous-Si layer, a doped amorphous-Si layer, and a transparent conducting oxide layer that is placed on both sides of a crystalline-Si substrate [16]. Grid electrodes are fabricated on both sides of the doped amorphous-Si layer. These cells have achieved an open circuit voltage of more than 700 mV, and additionally, all process temperatures are low, which preserves a high quality of the crystalline silicon [16].

Bifacial PV modules are made to absorb radiation through both the front and the rear surface. The rear surface can absorb irradiation reflected from the ground, direct irradiation at low solar angles, and diffuse sky radiation [17]. Unless the PV module is tilted vertically, the reflected irradiance from the ground accounts for most of the irradiation received at the back surface [17]. This suggests that the ground albedo has a significant impact on the efficiency of bifacial modules.

The test sites studied in this thesis also include several half-cell modules, which has become the industry standard today [18]. The production of half-cells is done by producing a standard full cell with a possible adaptation of the metalization layout [19]. These cells are then cut in half by laser scribing and cleavage or thermomechanically induced cell separation. This has been shown to increase the module power by up to 5 – 8 %, as it reduces resistive losses and gives a higher current at the module

level [19].

2.1.2 Temperature dependence of PV performance

This section is based on Ref. [6]. The I-V and P-V characteristics of a solar cell are important when analyzing the performance of a solar cell. The I-V curve shows the relationship between the current and voltage generated by the cell. Figure 2.1.2 shows the I-V curve and the corresponding P-V curve for different irradiances and temperatures. For $V = 0$, we have the short-circuit current I_{sc}, which is the maximum current the cell would generate with no load. For $I = 0$, we have the open-circuit voltage V_{oc}, which is the maximum voltage at zero current. The maximum power point (MPP) is the point on the curve where the product of the current and the voltage, i.e., the power, is at its maximum P_{mpp}. The fill factor (FF) is the ratio between the P_{mpp} and the product $I_{sc}V_{oc}$, indicating how square the curve is. A higher FF is a sign of a high-quality cell. Studying Figure 2.1.2, we see that an increase in irradiance leads to a rise in both the short-circuit current and the open-circuit voltage, with the increase larger for the current. For an increase in temperature, we see that the open-circuit voltage decreases significantly, while the short-circuit current increases slightly. The MPP is increasing significantly for an increasing irradiance, and decreasing for an increasing temperature.

Increasing the operating temperature has a linear negative effect on the electrical efficiency of PV modules [20]. The temperature dependence of the efficiency is described by the temperature coefficient of power, which is given in the data sheets of the modules. These coefficients are given for specific modules, typically in the range -0.25–0.50%/°C.

2.1.3 Temperature of bifacial modules

This section is based on Ref. [21]. The temperature of a bifacial PV module affects the power generation as for a monofacial PV module. However, as they have a different bill-of-material and a different effective irradiance, they do not necessarily have the same temperature behavior. In general, factors such as solar radiation, ambient temperature, panel composition, and mounting structure affect the PV module operating temperature. Many studies have investigated the temperature of the monofacial PV module, and then developed models to estimate the module temperature, some of which will be studied in this project. As there are differences in structure and material between monofacial and bifacial modules, even under equal installation conditions, there are differences in the heat transfer characteristics. Figure 2.1.3 shows three different sources of backside irradiance, the irradiance reflected from the ground, irradiance reflected from other PV modules, and diffuse irradiance from the sky. The same amount of backside irradiance is present for monofacial modules, but they usually have a backsheet with a high reflectance to absorb as little of the irradiance as possible. This potentially makes the temperature effect from backside irradiance minimal for monofacial modules. Bifacial modules, on the other hand, are designed to absorb as much of the backside radiation as possible, and the backside absorption therefore contributes to the heating of the modules. The amount of backside irradiance depends on factors like the albedo of the ground, the distance to the back-row racks, the hub height, the racking, the topography, and the tilt of the module.

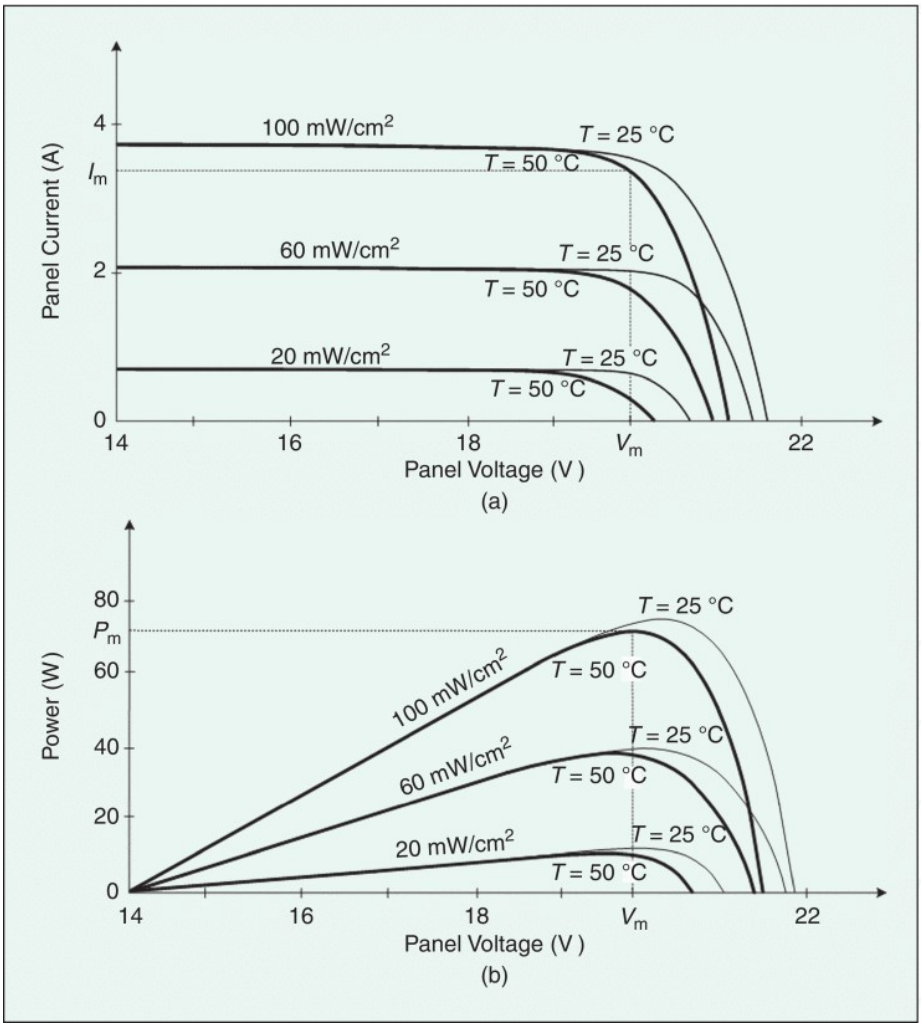

Figure 2.1.2: (a) I-V and (b) P-V curve for different irradiances and temperatures. Taken from Ref. [6]. © [2020] IEEE.

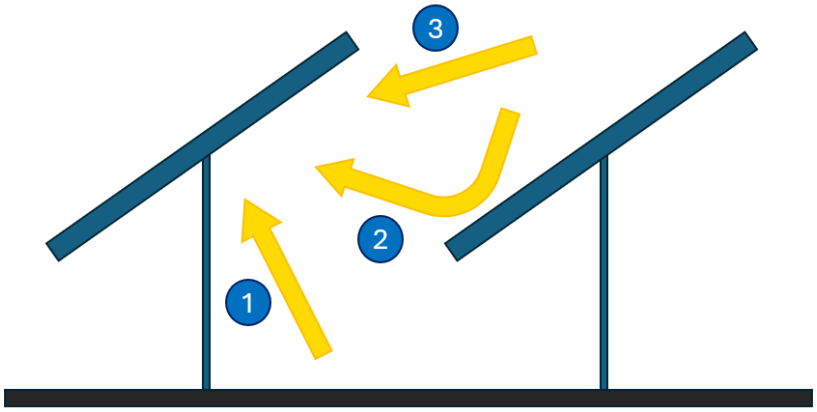

Figure 2.1.3: Sources of backside irradiance, (1) ground reflected, (2) PV reflected, and (3) sky diffuse. Figure created by the author, inspired by [21].

There can also be differences in the materials' insulating properties, as monofacial modules usually have an opaque backsheet, while bifacial modules have either glass or a transparent backsheet. For modules with a glass rear surface, the thickness of

the glass has a big impact on the cell temperature, as thicker glass insulates more and leads to a higher cell temperature. ANSYS Workbench simulations performed by Zhang et al. found that by increasing the thickness of both the front and rear glass by 0.5 mm, the cell temperature increased by 0.41 °C [21]. The simulations found that there were more transmissions of infrared irradiation from bifacial modules, leading to less internal heat absorption in the modules. The operating temperature of bifacial modules was therefore found to be 1.89 °C lower than for monofacial modules when there is no reflection from the ground [21]. The module temperature models that will be studied in this report, which are commonly used in the industry, are all developed for monofacial PV modules. An example is the thermal model developed by PVsyst v.7, for which in the declaration it is stated that the relevant value for incoming irradiance is the effective irradiance, but that for simplicity the incoming front-side irradiance is used [22]. This is the irradiance received in the front-side POA, and thus, the rear-side contribution is discarded. Thus, PVsyst modeling results for bifacial PV systems could be biased. The use of only the front-side POA irradiance is also seen in the other models studied in this project [23].

2.2 Solar irradiance

Photovoltaic technologies are fueled by solar radiation, which is a heterogeneous and variable combination of electromagnetic waves with wavelengths ranging from 0.3 to 4 μm [24]. This section will present some central principles about solar irradiance.

2.2.1 Extraterrestrial irradiance

For solar radiation reaching the Earth, the atmosphere in principle works as a filter that modifies the spectral power distribution of the solar radiation at the top of the atmosphere, referred to as extraterrestrial irradiance [24].

The extraterrestrial radiation is the radiation unaffected by the atmosphere, and will vary throughout the year due to the distance from the sun varying [25]. The extraterrestrial irradiance measured on a plane normal to the radiation on the Nth day of the year is given by

$$G_{on} = G_{sc}\left[1 + 0.33\cos\left(\frac{360N}{365}\right)\right]. \tag{2.1}$$

G_{sc} is the solar constant, i.e., the amount of solar energy per unit time, at the Earth's mean distance from the sun, received on a unit area of a surface normal to the sun outside the atmosphere [25]. The latest value of G_{sc} is 1366.1 W/m^2 [25].

2.2.2 Effect of the atmosphere

When irradiance travels through the atmosphere, various scattering processes occur. These scattering processes originate from inhomogeneities in the propagation medium's optical properties [26]. The propagation medium in the atmosphere is air, which mainly consists of the two diatomic gases nitrogen and oxygen. Rayleigh scattering is a process where scattering occurs for small spherical particles with a diameter much smaller than the wavelength of light [26]. The diameter of a nitrogen

molecule (∼0.3 nm) is, for instance, about 3 orders of magnitude smaller than the wavelength of visible light (∼500 nm) [26].

When Rayleigh scattering occurs, the oscillating electric field of the wave incident on the particle modifies the states of motion of the electrons in the atoms or molecules, initiating forced oscillations of the electrons at a frequency equal to that of the incident wave [27]. These oscillating electrons release part of their energy as electromagnetic radiation, appearing as scattered light. Scattering by significantly larger particles is called Mie scattering, giving distinct features to the scattered light from the Rayleigh scattering. A difference from Rayleigh scattering is that as the scatterer increases in size, the tendency to scatter shorter wavelengths more strongly decreases, and when the size reaches about 10–100 times the wavelength, all wavelengths are scattered equally [27]. This is why clouds appear white, as the aggregates of water molecules scatter all components of the light equally. Mie scattering has a pronounced scattering in the forward direction, while Rayleigh scattering spreads evenly in all directions [27]. Both Rayleigh and Mie are examples of scattering in the atmosphere that will create diffuse light by scattering the direct beam of light from the sun.

2.2.3 Irradiance components

Global Horizontal Irradiance (GHI) is the total solar radiation, i.e., the sum of Direct Normal Irradiance (DNI), Diffuse Horizontal Irradiance (DHI), and ground-reflected radiation received in a unit plane horizontal to the surface of the earth [28]. However, as ground-reflected radiation is often insignificant compared to direct and diffuse, for all practical purposes, GHI is often said to be the sum of direct and diffuse radiation only, as

$$\mathrm{GHI} = \mathrm{DHI} + \mathrm{DNI} \cdot \cos(Z), \tag{2.2}$$

where Z is the solar zenith angle [28]. Though small, the ground-reflected can also be relevant when studying irradiance for PV purposes, especially for bifacial modules. Its magnitude will depend on the albedo of the ground. The albedo is the fraction of incident irradiance that is reflected by the surface [29]. The albedo can vary a lot for different surfaces. Examples of surfaces with low albedos are oceans, lakes, and forests, while snow, sea ice, and deserts reflect relatively large fractions of the irradiance and have large albedos [29]. Snow has an albedo of 0.66, while short grass has an albedo of 0.20 [29].

2.2.4 Clearsky irradiance

The clearsky irradiance is the irradiance we would have if there were no cloud cover, meaning it can be seen as an upper limit for the irradiance at a given time and position. However, on occasion, the irradiance can exceed this clearsky irradiance during events of forward scattering of irradiance from clouds, which is called cloud-enhanced irradiance [30]. This occurs under partially cloudy conditions and can last from a few seconds to several minutes, depending on the cloud motion. Clearsky models can be used to approximate Global Horizontal Irradiance (GHI), Direct Normal Irradiance (DNI), and Diffuse Horizontal Irradiance (DHI). DNI is the light arriving directly from the sun to the surface. DHI is all light that does not arrive directly from the sun, i.e., the diffuse light scattered from clouds or particles in the air. GHI is the

total irradiance arriving on a horizontal plane, meaning that both DNI and DHI are components of GHI as follows $GHI = DNI \cdot \cos(\theta_z) + DHI$, where θ_z is the solar zenith angle [31].

The Ineicen–Perez model is a model that estimates the clearsky GHI using the zenith angle and some atmospheric state variables such as air pressure, temperature, relative humidity, aerosol content, and Reyleigh scattering [32]. The Ineichen–Perez model is given by

$$\begin{aligned} GHI_{clearsky} = c_{g1} \cdot I_0 \cdot \cos(z) \\ \cdot \exp(-g_{g2} \cdot AM \cdot (f_{h1} + f_{h2}(TL - 1)) \cdot \exp(0.01 \cdot AM^{1.8}), \end{aligned} \tag{2.3}$$

where $c_{g1} = 5.09e-9 \cdot h + 0.898$ and $c_{g2} = 3.92e-5 \cdot h + 0.0387$. h is the elevation, AM is the air mass, and TL is the Linke Turbidity [32]. For a further description of the air mass and the Linke Turbidity see Ref. [32]. A measure of the ratio of measured GHI and the clearsky GHI often used is the clearsky index, given by [33]

$$k = \frac{GHI_{measured}}{GHI_{clearsky}}. \tag{2.4}$$

This clearsky index will be 0 for zero irradiance and 1 for the clearsky irradiance. The index can also exceed 1 for conditions with cloud-enhanced irradiance. To have a measure of how much the weather varies, we introduce a variability index for the clearsky index, defined as

$$V = \sqrt{\frac{1}{N}\sum_{i=1}^{N}(k_{i+1} - k_i)^2}, \tag{2.5}$$

where we sum over all N measurements within the hour or day, depending on the time period we are studying [34].

2.3 Temperature models

Below, all temperature models that will be evaluated and further developed in the project are explained. As an observant reader might discover through dimension analysis, there are unit inconsistencies in some model equations in this section. This stems from the fact that these are empirical formulas. As some variables and abbreviations are repeated several times in this section, they will only be introduced at first encounter and can be found in the list of abbreviations and symbols. Derivation details for the models will be included in this section for completeness, however, only the main features and the assumptions made by the models will be included in further discussions.

Figure 2.3.1 shows the commonly included parameters in the temperature models, i.e., the POA irradiance, radiative loss to the sky, heat exchange with the surroundings, and wind.

2.3.1 Sandia Array Performance Model

This section is based on Ref. [35]. The Sandia Array Performance Model (SAPM) is an estimation model for the module temperature of a PV module developed by Sandia National Laboratories for purposes such as system engineering and performance

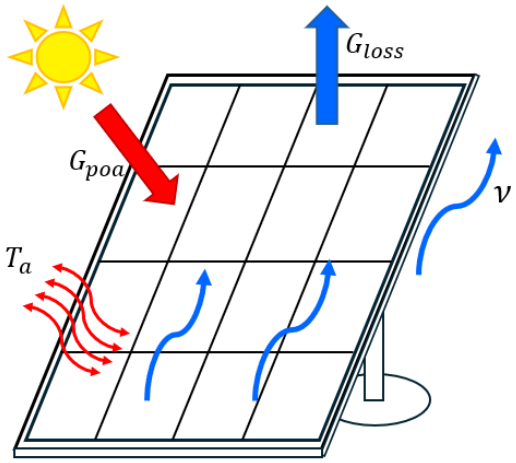

Figure 2.3.1: Main parameters included in the temperature models.

modeling. The first thermal model was developed in the mid-1980s, but was later found to be unnecessarily complex and not as adaptable as was wanted. This led to a simpler empirical model, that only requires the irradiance, temperature, and wind speed. The back-surface module temperature is given by

$$T_m = G_{poa} \cdot \exp(a + b \cdot v) + T_a, \tag{2.6}$$

where G_{poa} is the POA irradiance, T_a is the ambient air temperature, and v is the wind speed measured at 10 meters height. The model parameters a and b are determined empirically and are dependent on the module surface materials and the mounting. a represents an upper limit for the module temperature at low wind speeds and high solar irradiance, while b represents the rate of change in the module temperature with increasing wind speed. The parameters were determined using temperature measurements conducted over several different days with the modules in near thermal equilibrium conditions. The measurements were performed at Sandia National Laboratories in Albuquerque, New Mexico. The model parameters are given in Table 2.3.1.

Table 2.3.1: Model parameters for the SAPM module temperature. a and b are the model parameters, and ΔT is the temperature difference used in Eq. (2.7) to estimate the cell temperature. [35]

Module	Mounting	a [∅]	b [s/m]	ΔT [°C]
glass/glass	open rack	-3.47	-0.0594	3
glass/glass	close roof	-2.98	-0.0471	1
glass/polymer	open rack	-3.56	-0.075	3
glass/polymer	insulated back	-2.81	-0.0455	0

The authors found that this model predicted the module temperature with an accuracy of about ±5 °C, which is of a magnitude that results in less than a 3% effect on the predicted power output from the module. The wind direction was found to have a small influence on the temperature, but it was believed to be unnecessarily complex to include in the model.

The Sandia Array Performance Model can also be used to estimate the cell temperature, by using a provided relation given by

$$T_c = T_m + \frac{G_{poa}}{G_0} \cdot \Delta T. \tag{2.7}$$

This relation says that the cell temperature is equal to the module temperature with an additional term, where the temperature difference between the cell and the back surface at a reference irradiance G_0 of 1000 W/m^2 is multiplied by the measured irradiance G_{poa} divided by the reference irradiance G_0. The proposed values for the temperature difference ΔT are given in Table 2.3.1.

2.3.2 Faiman Model

This section is based on Ref. [7]. The Faiman model is a temperature model that can be used to calculate cell and module temperature, as they are assumed to be equal. The model uses an empirical heat loss factor model, with two heat transfer coefficients, determined by Faiman for 7 silicon modules installed on an open rack at a 30.9° tilt, facing due south. The setup was located at Sede Boqer in the Negev Desert, Israel, at an altitude of 470 meters above sea level. The temperature and irradiance measurements were logged every 10 seconds for 1 week in November, 2006, and stored as 5-minute averages.

The Faiman model is based on the Hottel–Whillier–Bliss equation, which is developed for a solar-thermal collector, given by

$$\eta = \eta_0 - (U/H)(T_m - T_a). \tag{2.8}$$

This shows that the efficiency η of a solar-thermal collector with steady-state conditions is the difference between a temperature-independent optical part η_0 and a thermal part. The thermal part increases with an increasing temperature difference between the collector and the surroundings. This difference is multiplied by the heat transfer coefficient U divided by the total incident irradiance on the collector.

Faiman found that the Hottel–Whillier–Bliss equation could be employed to predict module temperatures within an accuracy comparable to the small temperature differences typically encountered within a module. The resulting expression for the module temperature is given by

$$T_m = T_a + \frac{G_{poa}}{U_0 + U_1 \cdot v} \tag{2.9}$$

where

$$U_0 = U_0'/(\eta_o - \eta_e) \text{ and } U_1 = U_1'/(\eta_o - \eta_e). \tag{2.10}$$

As the optical efficiency η_o of a glass-covered water-heating collector is typically a constant in the range 0.8 – 0.9 and the electrical efficiency η_e of a PV module typically lies around 0.1, $(\eta_o - \eta_e)$ typically fluctuates around 0.7. As the efficiencies will not vary much, we can view U_0 and U_1 as constants, so our module temperature given by Eq. (2.9) only depends on T_a, G_{poa}, and v. The values proposed by Faiman for U_0 and U_1 are 25.0 W/(m^2 °C) and 6.84 W/(m^2 °C (m/s)), which are the combined fit for the measurements done by Faiman in the Negev desert. The combined fit gave an RMSE of 1.86 °C for the data set used in the parameter fitting.

2.3.3 Faiman Model with Radiative Loss

This section is based on Ref. [36]. The Faiman Model is an example of a steady-state thermal model, which is a one-dimensional, linear, lumped parameter model with coefficients determined empirically. These models represent all aspects of the heat exchange between the module and its surroundings, as well as the generation and transfer of heat inside the module, with only a few parameters. In such models, the heat loss rate is assumed to be linearly dependent on the temperature difference between the module and its surroundings, which means that the module temperature can never drop below the ambient temperature. In reality, we see that the module temperature frequently drops below the ambient temperature at night, due to emission of long-wave radiation to the cold sky. As this also occurs during the day, not accounting for this effect can cause the models to overestimate the module temperature. To avoid this, the Faiman Model can be augmented with a radiative loss term, which was proposed by Anton Driesse.

The model is based on the following high-level, steady-state, thermal energy balance (disregarding thermal capacitance)

$$q_{sun} - q_{elec} - q_{rad} - q_{conv} - q_{cond} = 0, \tag{2.11}$$

where q_{sun} is the energy flux from the sun, q_{elec} is the energy flux extracted to electrical power, and q_{rad}, q_{conv} and q_{cond} are heat losses due to radiation, convection, and conduction. Conduction is assumed negligible, due to the small area of contact between the PV module frame and the mounting. By simply lumping the radiative losses together with the convective losses, one ends up with a model that does not allow for the module temperature to drop below the ambient temperature. As module temperatures below the ambient temperature are common in reality, another approach is used in the Faiman model with a radiative term. To formulate the radiative exchange between the module and the sky, we can introduce an effective sky temperature T_s. The radiative heat exchange is given by

$$q_{rad} = F \cdot \epsilon \cdot \sigma \cdot (T_m^4 - T_s^4), \tag{2.12}$$

where F is the view factor between the module and the sky, ϵ is the emissivity of the module and σ is the Stefan Boltzmann constant. We can then split the radiative loss to the sky into two parts, $q_{rad,m}$ and $q_{rad,s}$, with the ambient temperature as a common reference temperature as follows

$$q_{rad} = q_{rad,m} + q_{rad,s} \tag{2.13}$$
$$q_{rad,m} = F \cdot \epsilon \cdot \sigma \cdot (T_m^4 - T_a^4) \tag{2.14}$$
$$q_{rad,s} = F \cdot \epsilon \cdot \sigma \cdot (T_a^4 - T_s^4) \tag{2.15}$$

$q_{rad,s}$ can be kept as is, as T_a and T_s are known, but $q_{rad,m}$ is linearized in the following way

$$q_{rad,m} = u_{rad,m} \cdot (T_m - T_a), \tag{2.16}$$

introducing a heat transfer coefficient $u_{rad,m}$, and a thermal energy balance equation as follows

$$q_{sun} - F \cdot \epsilon \cdot \sigma \cdot (T_a^4 - T_s^4) - (u_{rad,m} + u_{conv}) \cdot (T_m - T_a) = 0. \tag{2.17}$$

By solving this equation for the module temperature, we arrive at

$$T_m = T_a + \frac{q_{sun} - F \cdot \epsilon \cdot \sigma \cdot (T_a^4 - T_s^4)}{U}, \tag{2.18}$$

where $u_{rad,m}$ and u_{conv} are joined together as U. Combining this with the Faiman model in Eq. (2.9), we get

$$T_m = T_a + \frac{G_{poa} - F \cdot \epsilon \cdot (\sigma \cdot T_a^4 - q_{dr})}{U_0 + U_1 \cdot v}, \tag{2.19}$$

where q_{dr} is the down-welling infrared radiation from the sky, measured on a horizontal surface. The U_0 and U_1 values were estimated for the new Faiman model with a radiative loss term, using measurements performed for a reference cell at two locations: Albuquerque, New Mexico, and Freiburg, Germany. This was done using an estimated value for $F \cdot \epsilon$ equal to 0.76, and down-welling radiation data obtained from the ERA5 database, the resulting values proposed are $U_0 = 20.74$ W/(m^2 °C) and $U_1 = 2.91$ W/(m^2 °C (m/s)). The model also requires a view factor F, which for a tilted array can be approximated by

$$F = \frac{1 + 3\cos(\theta)}{4}, \tag{2.20}$$

where θ is the array tilt.

2.3.4 Fuentes Model

This section is based on Ref. [37]. The Fuentes model is a first-principles heat transfer energy balance model for cell or module temperature modeling. The Fuentes model includes the effects of the heat capacity of the module and includes a numerical integration between each timestep to account for thermal lag transient behavior. [38] The model was developed at Sandia National Laboratories, for usage in PVFORM, which is a PV performance model. The required inputs are POA irradiance, ambient temperature, wind speed, average array height above ground, anemometer height and the Installed Nominal Operating Cell Temperatures (installed NOCT) at NOCT conditions (800 W/m^2 irradiance, 20 °C ambient temperature, and 1 m/s wind speed). The model uses installed NOCT to estimate heat gain and convection and radiation losses at NOCT conditions.

The following derivation follows that of Ref. [37]. As the reader will be pointed to Ref. [37] for further explanations and derivations of some model variables, the original notation is kept in the derivation for simplicity. By modeling the PV module as a single piece of solid material at a uniform temperature T_c, we can write the energy balance as

$$hc \cdot (T_c - T_a) + \epsilon \cdot \sigma \cdot (T_c^4 - T_s^4) + \epsilon \cdot \sigma \cdot (T_c^4 - T_g^4) - \alpha \cdot S + m \cdot c \cdot \frac{dT_c}{dt} = 0, \tag{2.21}$$

where hc is the overall convective coefficient of the module, ϵ is the emissivity of the module, σ is Boltzmann's constant, α is the absorptivity of the module, m is the mass of the module per unit surface area, and c is the overall specific heat of the module. Here we see that the module receives heat from insolation S, and loses heat

by convection to ambient temperature, T_a, and radiation to the sky and ground, T_s and T_g.

By noticing that the radiation terms can be expanded as

$$\begin{aligned}(T_c^4 - T_s^4) &= (T_c^2 + T_s^2) \cdot (T_c + T_s) \cdot (T_c - T_s) \\ (T_c^4 - T_g^4) &= (T_c^2 + T_g^2) \cdot (T_c + T_g) \cdot (T_c - T_g),\end{aligned} \tag{2.22}$$

we can linearize Eq. (2.21). Since the products $(T_c^2 + T_s^2) \cdot (T_c + T_s)$ and $(T_c^2 + T_s^2) \cdot (T_c + T_s)$ change by less than 5% for a 10°C change T_c, this is assumed to be nearly constant. This makes the radiation terms in Eq. (2.21) linear, making it easier to solve. After 5 iterations of solving for T_c and reevaluating the values of these constants, we can obtain a nearly exact solution. We can simplify Eq. (2.21) with the following coefficients

$$\begin{aligned}hr_s &= \epsilon \cdot \sigma \cdot (T_c^2 + T_s^2) \cdot (T_c + T_s) \\ hr_g &= \epsilon \cdot \sigma \cdot (T_c^2 + T_g^2) \cdot (T_c + T_g),\end{aligned} \tag{2.23}$$

where hr_s is the radiative coefficient to the sky, and hr_g is the radiative coefficient to the ground. To be able to model the insolation profile as a continuous function, we assume that it varies linearly between the time steps as

$$S = S_0 + \Delta S \cdot \frac{t}{\Delta t}. \tag{2.24}$$

This is done instead of modeling it as a step function, which would not be a realistic behavior for the insolation, leading to an additional error in the calculation of T_c. The resulting heat equation is

$$hc \cdot (T_c - T_a) + hr_s \cdot (T_c - T_s) + hr_g \cdot (T_c - T_g) - \alpha \cdot (S_0 - \Delta S \cdot \frac{t}{\Delta t}) + m \cdot c \cdot \frac{dT_c}{dt} = 0. \tag{2.25}$$

By integration of Eq. (2.25), the following expression for T_c is obtained

$$T_c = \frac{(hc \cdot T_a + hr_s \cdot T_s + hr_g \cdot T_g + \alpha \cdot S_0 + \alpha \cdot \Delta S/L) \cdot (1 - e^L) + \alpha \cdot \Delta S}{hc + hr_s + hr_g} + T_{c_0} \cdot e^L. \tag{2.26}$$

T_{c_0} is the module temperature at the beginning of the time step, and L is a factor that characterizes the thermal lag of the module, given by

$$L = -(hc + hr_s + hr_g) \cdot \Delta t/(m \cdot c). \tag{2.27}$$

All parameters on the right hand side of Eq. (2.26) is either known or can be obtained. For further explanations and derivations of the variables in Eq. (2.26), see Ref. [37].

2.3.5 PVsyst Cell Temperature Model

This section is based on Ref. [22]. The PVsyst cell temperature model is derived from the following energy balance, accounting for energy fluxes in and out of the module,

$$G_{poa} \cdot \alpha \cdot (1 - \eta_m) = U \cdot (T_c - T_a), \tag{2.28}$$

where U is an empirical heat loss factor, η_m is the module efficiency, and α is the absorbance, i.e. $(1 - \text{reflection})$. The heat loss factor is split into a constant component U_c and a factor proportional to the wind velocity U_v, as follows

$$U = U_c + U_v \cdot v. \tag{2.29}$$

The model parameters U_c and U_v depend on factors like the bill-of-materials, the structure of the frame, and the mounting of the module. However, having reliable wind measurements at a height of 10 m, which is required for the wind speed, is seldom in the datasets used, and it is therefore recommended to use the model without wind dependency, i.e., with $U_v = 0$. Table 2.3.2 shows the parameters for open (freestanding) and closed (insulated) mounting configurations. These represent the combined heat loss effect of convection, radiation, and conduction, and are determined assuming a constant wind speed of 3.3 m/s. The empirical values have been determined using measurements from 7 different test sites in Switzerland [39]. Solving Eq. 2.28 for T_c we find that

$$T_c = T_a + \frac{\alpha \cdot G_{poa}(1 - \eta_m)}{U_c + U_v \cdot v}. \tag{2.30}$$

Table 2.3.2: Model parameters for PVsyst cell temperature model. [22]

Mounting	U_c	U_v
freestanding	29.0	0.0
insulated	15.0	0.0

2.3.6 Ross Cell Temperature Model

This section is based on Ref. [40]. The Ross model incorporates the NOCT, as it quantifies the thermal design of the modules, and works as a reference temperature for rating power output. The NOCT value is the cell temperature of a module at 800 W/m^2 irradiance, air temperature of 20 °C, and a wind speed of 1 m/s. These conditions are determined such that the annual energy produced by a module is well approximated by its efficiency at the NOCT conditions multiplied by the incident irradiance on the module, in kWh/year. The Ross model was developed at the Jet Propulsion Laboratory at the California Institute of Technology.

The model assumes that the temperature difference between the cell and its surroundings is proportional to the irradiance, and that the wind speed is constant at 1 m/s. The Ross model is given by

$$T_c = T_a + \frac{NOCT - 20\ ^\circ\text{C}}{800\ \text{W/m}^2} G_{poa}. \tag{2.31}$$

2.3.7 Driesse model

This section is based on Ref. [41]. Anton Driesse recently presented a model establishing a useful link between the steady-state and dynamic worlds. It demonstrates that the effect of the thermal mass can be modeled by applying a first-order low-pass filter to either the inputs or the output of a simple steady-state model.

The model is based on a variety of temperature models that are algebraically identical to the following equation

$$T_m = T_a + \frac{G_{poa}}{U}, \tag{2.32}$$

where U is a heat transfer coefficient representing the combined average effect of all heat loss mechanisms. To incorporate a thermal mass or capacitance C, Eq. 2.32 can be rearranged as the following thermal balance,

$$G - (T_m - T_a)U - C\frac{dT_m}{dt} = 0. \tag{2.33}$$

T_a and G are time-varying quantities, and by solving Eq. 2.33 for a time-varying T_m we get the following exact solution,

$$T_m(t) = (f * T_a)(t) + \frac{(f * G)(t)}{U} + c_0 e^{-\frac{U}{C}t} \tag{2.34}$$

, where

$$f(t) = \frac{U}{C} e^{-\frac{U}{C}t} \tag{2.35}$$

is the impulse response of a first-order low-pass filter and $*$ is the convolution operator. This effectively applies a low-pass filter to each of the two model inputs T_a and G. C/U is the time constant for the lowpass filter, and can be replaced by τ as

$$f(t) = \tau^{-1} e^{-\frac{t}{\tau}},\ t \geq 0. \tag{2.36}$$

In Eq. 2.34 the c_0 term accounts for a possible start-up transient. As time-series for PV modeling usually have an initial low irradiance, this term will be insignificant after a short time. U and τ can be found by using a non-linear optimization algorithm.

A significant fraction of the irradiance absorbed by a module is radiated back to the sky. This radiative loss has been included in the Faiman model with a radiative term, given by Eq. 2.19.

We can define

$$G_{net} = G_{poa} \cdot (1 - \rho - \eta - \tau_0) \tag{2.37}$$

and

$$L_{net} = \sigma T_a^4 - q_{dr}, \tag{2.38}$$

where we reduce the incoming irradiance by the fractions that are reflected, ρ, converted to electricity, η, and transmitted, τ_0. By including G_{net} and L_{net}, and by allowing for F and ϵ to be replaced by a single empirical parameter Fe, we get the following steady-state equation

$$T_m = T_a + \frac{G_{net} - Fe \cdot L_{net}}{u_c + u_w \cdot v}. \tag{2.39}$$

This can be rewritten as an energy balance with added capacitance, giving

$$G_{net} - Fe \cdot L_{net} - (T_m - T_a)(u_c + u_v \cdot v) - C\frac{dT_m}{dt}. \tag{2.40}$$

This leaves us with two approximate solutions, given by

$$T_m(t) = (f * T_a)(t) + \frac{(f * G_{net})(t) - Fe(f * L_{net})(t)}{u_c + u_w \cdot (f * v)(t)} \tag{2.41}$$

and

$$T_m(t) = \left(f * \left(T_a(t) + \frac{G_{net}(t) - FeL_{net}(t)}{u_c + u_w \cdot v(t)} \right) \right)(t). \tag{2.42}$$

The final model then has three empirical parameters, u_c, u_v, and Fe, which are proposed to be tuned using measurement data.

2.4 Temperature model equivalence

This section is based on Ref. [42], and will demonstrate how three of the temperature models presented in this thesis, the Faiman model, the Sandia Array Performance model, and the PVsyst model, have identical or very similar characteristics and differ mostly in parameterization. All the models describe a thermal balance between the module and its environment. A high-level thermal balance, expressing that the heat gains must equal the heat losses, is given by

$$q_{sun} - q_{elec} - q_{rad} - q_{conv} - q_{cond} = 0, \tag{2.43}$$

where q_{sun} is the energy flux from the sun, q_{elec} is the energy flux turned into electricity, and q_{rad}, q_{conv}, and q_{cond} are heat loss fluxes due to radiation, convection and conduction. As the contact area between the module and its mounting is small, the conduction is assumed to be negligible. The convection and radiation losses are then lumped together as q_{cr}, giving

$$q_{sun} - q_{elec} - q_{cr} = 0. \tag{2.44}$$

q_{qr} is dependent on a large number of parameters and properties. However, its main tendency is to increase as the module temperature rises above the ambient temperature. Using a one-dimensional, linear approximation of this tendency, we get the following thermal balance equation

$$q_{sun} - q_{elec} - U_{cr}(T_m - T_a) = 0, \tag{2.45}$$

where U_{cr} is a combined heat transfer coefficient. Rearranging this, we are left with a model for the module temperature, given by

$$T_m = T_a + \frac{q_{sun} - q_{elec}}{U_{cr}}. \tag{2.46}$$

As q_{elec} and q_{sun} are approximately proportional, we can simplify by scaling U_{cr} to U, leaving us with

$$T_m = T_a + \frac{q_{sun}}{U}. \tag{2.47}$$

The Faiman model, the Sandia Array Performance model, and the PVsyst model are all variations of this equation. As all models use G_{poa} as input, we can rewrite Eq. 2.47 as

$$T_m = T_a + \frac{G_{poa}}{U}. \tag{2.48}$$

From this equation we can obtain the Sandia Array Performance model given by Eq. 2.6 by setting

$$U = \exp(-a - b \cdot v). \tag{2.49}$$

The Faiman model given by Eq. 2.9 can be obtained by setting

$$U = U_0' + U_1' \cdot v. \tag{2.50}$$

To obtain the PVsyst model given by Eq. 2.30, U has to be defined as

$$U = \frac{U_c + U_v \cdot v}{\alpha \cdot (1 - \eta_m)}. \tag{2.51}$$

The model parameters of each model can then be adjusted so that the Faiman model and the PVsyst model are equal, as they are both linearly dependent on the wind speed. The SAPM model, on the other hand, cannot become exactly equal, as it is exponentially dependent on the wind speed. However, it can provide a near approximation of the two other models. We can, therefore, conclude that the Faiman model, the PVsyst model, and the Sandia Array Performance model are three nearly equivalent models. For demonstration of how Faiman parameters can be translated to SAPM and PVsyst parameters, see Ref. [42].

2.5 PVWatts DC power model

This section is based on Ref. [43].

PVWatts is a web application that estimates the electricity production of a PV system based on a few inputs, developed by National Renewable Energy Laboratory. PVWatts combines several sub-models predicting the factors that affect the energy production. PVWatts is a useful tool for performing quick estimates of energy production from PV systems.

PVWatts computes the DC power P_{dc} generated by the module using the power generated by the module at a reference temperature T_{ref} and irradiance $G_{poa,ref}$, P_{dc0}. The standard values are a T_{ref} of 25 °C and a $G_{poa,ref}$ of 1000 W/m^2. The efficiency of the module is assumed to decrease linearly as a function of an increase in temperature, with a module-specific temperature coefficient γ. The DC power is then given by

$$P_{dc} = \frac{G_{poa,eff}}{1000 \text{ W/m}^2} P_{dc0}(1 + \gamma(T_c - T_{ref}), \tag{2.52}$$

where $G_{poa,eff}$ is the irradiance transmitted to the PV cells, and T_c is the cell temperature. In the PVWatts implementation, a fixed temperature coefficient is used, which was determined from a statistical analysis of over 11 000 modules. However, in the PVlib implementation used in this thesis, the temperature coefficients of the specific modules are required.

2.6 Climate classification

This section is based on Ref. [8]. Wladimir Köppen presented the first quantitative classification of world climates in 1990. This was made available as a world map

updated in 1954 and 1961 by Rudolph Geiger. This is known as a Köppen–Geiger map. Köppen based his classification on five vegetation groups, determining the first letter in the classification: plants of the equatorial zone (A), the arid zone (B), the warm temperate zone (C), the snow zone (D), and the polar zone (E). The second and third letters in the classification represent the precipitation and the temperature, e.g., Dfc for snow zone, fully humid with a cool summer. Table 2.6.1 gives the specific criteria for the climate classes. Figure 2.6.1 shows a world map colored by the Köppen–Geiger climate classifications. The marked locations are those relevant for this thesis, meaning the locations of the PV test sites used in the development of the empirical models and the two test sites for which they will be tested and modified. The two test sites in Norway, Kjeller and Gålå, are in two different climate classes: Dfb and Dfc. Dfb is a warm-summer humid continental climate, while Dfc is a subarctic climate [9].

The Sandia Array Performance Model was tuned for measurements performed at Sandia National Laboratories in Albuquerque, New Mexico. Albuquerque has a BSk climate classification, a cold steppe climate, meaning a low annual precipitation and a mean annual temperature below 18 °C.[44]

The Faiman model was tuned for measurements performed at a PV test site in the Negev desert, which has a BWh climate. BWh is a hot desert climate, meaning we have minimal precipitation and a mean annual temperature of over 18 °C. [44]

The Faiman model with a radiative term was tuned with data from Albuquerque, New Mexico and Freiburg, Germany. Freiburg has a Cfb climate, a warm temperate fully humid climate with a warm summer. [44]

The PVsyst cell temperature model is tuned for measurements from 7 different test sites in Switzerland, which mostly has a Cfb climate.[44]

The Ross cell temperature model is derived from laboratory tests, meaning that the location's climate zone does not apply.

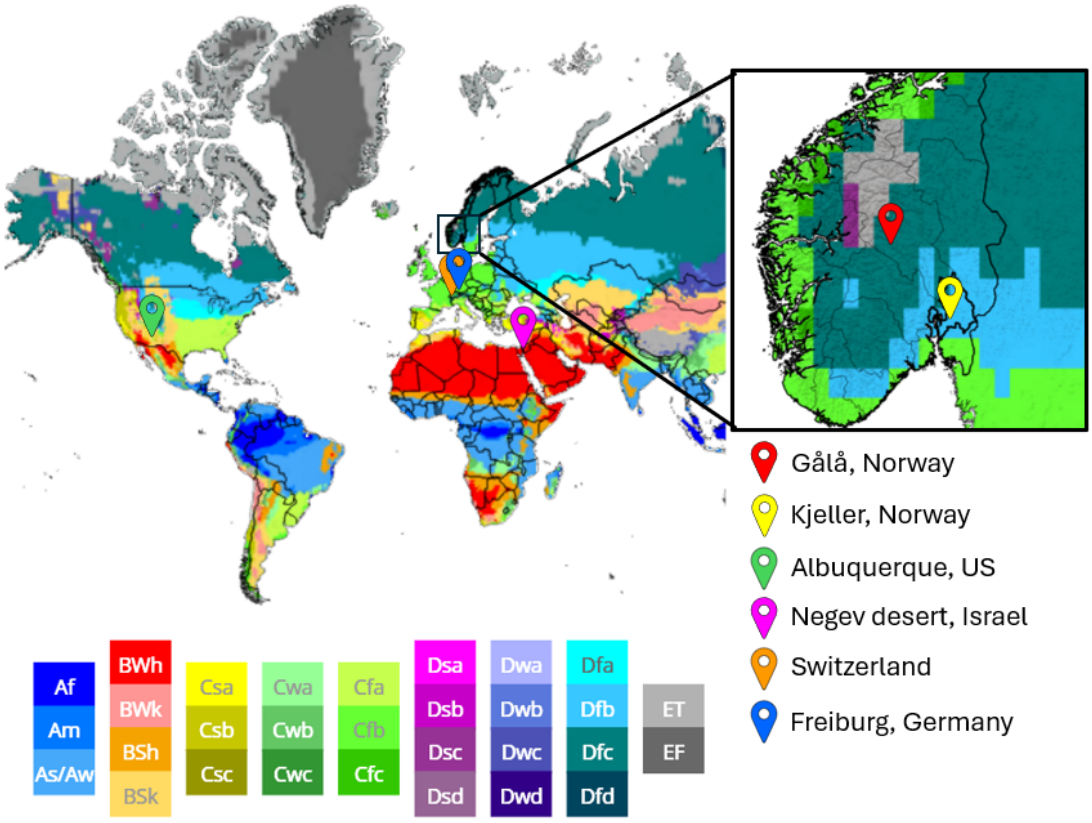

Figure 2.6.1: Köppen-Geiger climate classification for the time period 1991–2020. The relevant areas for the thesis are marked on the map to highlight the climate differences. Figure reproduced from [9] and modified by the author.

Table 2.6.1: Climate Classification Table, recreated from [8]. T_{min} and T_{max} denote the minimum and maximum temperature, P_{min}, P_{max}, and P_{ann} denote the minimum, maximum, and annual precipitation. P_{th} is a dryness precipitation threshold. w and s denote winter and summer.

Type	Description	Criterion
A	**Equatorial climates**	$T_{\text{min}} \geq +18°\text{C}$
Af	Equatorial rainforest, fully humid	$P_{\text{min}} \geq 60$ mm
Am	Equatorial monsoon	$P_{\text{ann}} \geq 25(100 - P_{\text{min}})$
As	Equatorial savannah w/ dry summer	$P_{\text{min}} < 60$ mm in summer
Aw	Equatorial savannah w/ dry winter	$P_{\text{min}} < 60$ mm in winter
B	**Arid climates**	$P_{ann} < 10\ P_{th}$
BS	Steppe climate	$P_{ann} > 5\ P_{th}$
BW	Desert climate	$P_{ann} \leq 5\ P_{th}$
C	**Warm temperate climates**	$-3°\text{C} < T_{\text{min}} < +18°\text{C}$
Cs	Warm temperate w/ dry summer	$P_{s,\text{min}} < P_{w,\text{min}}, P_{w,\text{max}} > 3P_{s,\text{min}}, P_{s,\text{min}} < 40$ mm
Cw	Warm temperate w/ dry winter	$P_{w,\text{min}} < P_{s,\text{win}}, P_{s,\text{max}} > 10P_{w,\text{min}}$
Cf	Warm temperate, fully humid	Neither Cs nor Cw
D	**Snow climates**	$T_{\text{min}} \leq -3°\text{C}$
Ds	Snow climate w/ dry summer	$P_{s,\text{min}} < P_{w,\text{min}}, P_{w,\text{max}} > 3P_{s,\text{min}}, P_{s,\text{min}} < 40$ mm
Dw	Snow climate w/ dry winter	$P_{w,\text{min}} < P_{s,\text{min}}, P_{s,\text{max}} > 10P_{w,\text{min}}$
Df	Snow climate, fully humid	Neither Ds nor Dw
E	**Polar climates**	$T_{\text{max}} < +10°\text{C}$
ET	Tundra climate	$0°\text{C} \leq T_{\text{max}} < +10°\text{C}$
EF	Frost climate	$T_{\text{max}} < 0°\text{C}$

CHAPTER

THREE

METHODS

This chapter will address the project's methodologies and tools, from data acquisition to the evaluation and further development of the temperature models. Sections 3.1.1 and 3.2 – 3.3.2 are adapted from the authors' specialization project [10].

3.1 Data acquisition

All data used in the evaluation of the models and further model development are collected at two PV test sites located at Kjeller and Gålå. As the two test sites are different in both module and measurement configurations, they will be presented separately.

3.1.1 Kjeller test site

The first dataset consists of measurements performed at the outdoor PV test site at IFE, Kjeller. Figure 3.1.1 shows the relative positions of the different modules and sensors in the PV system.

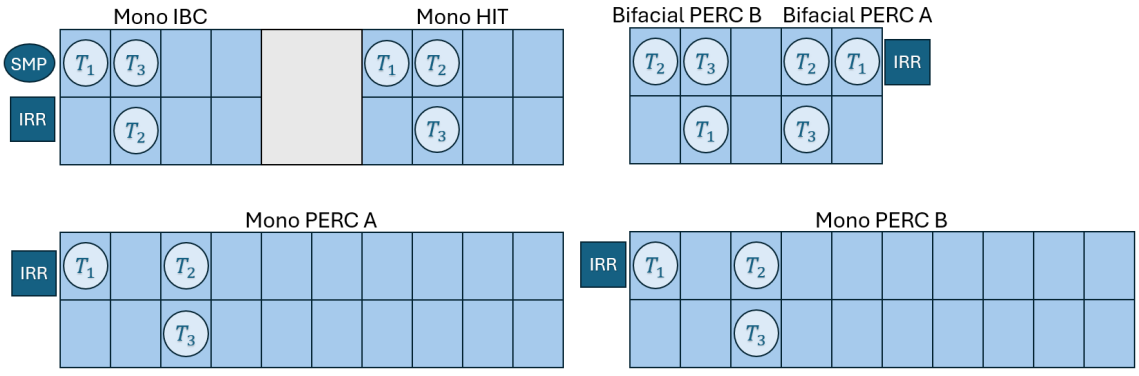

Figure 3.1.1: Map of the outdoor PV test site at IFE, Kjeller, notice that the relative placement of the different module types and sensors are approximate. The temperature sensors are annotated with a "T", while "IRR" denotes reference cell irradiance sensors and "SMP" denotes pyranometers. Reproduced from [10].

All modules are installed in an open rack configuration with a tilt of 45° facing due south with an azimuth of 180° [45]. The test site is located at 59.972 °N, 11.052

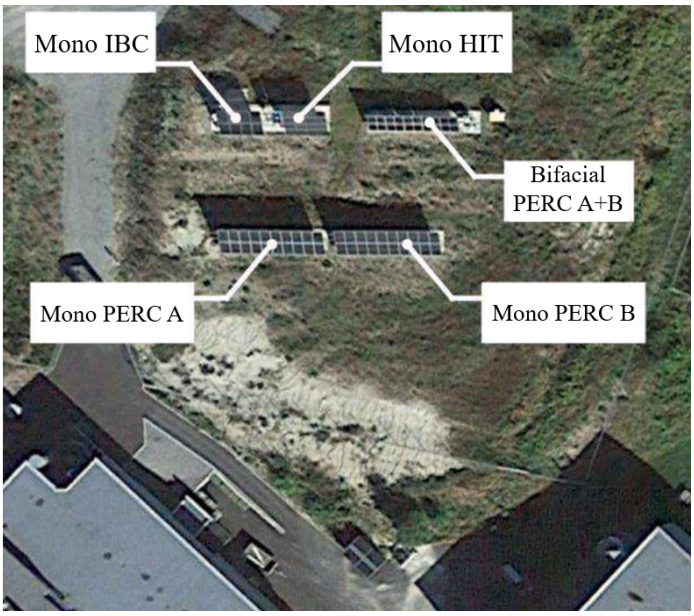

Figure 3.1.2: Satellite image showing the PV test site at IFE, Kjeller. Adapted from [45]

°E, and a height of 130 meters above sea level. The modules are installed in a 2P configuration, and have clearance heights in the range 0.70 – 0.75 m. The key properties of the modules are listed in Table 3.1.1.

Table 3.1.1: Key properties of the module technologies in the PV test site at IFE Kjeller [45]. Reproduced from [10].

Manufacturer	Cell technology	Features	Dimensions	Installed NOCT	Temperature coefficient of power
A	Mono PERC A	Full cell	1665×1002 mm	45 ± 2 °C	-0.37 %/°C
A	Mono PERC B	Half-cell	1684×1002 mm	45 ± 2 °C	-0.36 %/°C
B	Mono IBC	Full cell	1690×1046 mm	Not specified	-0.29 %/°C
C	Mono HIT	Half-cell	1721×1016 mm	44 ± 2 °C	-0.26 %/°C
D	Bifacial PERC A	Half-cell	1715×1045 mm	43 ± 2 °C	-0.36 %/°C
D	Bifacial PERC B	Half-cell	1645×1045 mm	43 ± 2 °C	-0.36 %/°C

The measurements were carried out between January 1st, 2021, and August 12th, 2024. All measurements of temperature and weather parameters are given as 5-minute mean values, while the raw data were collected at a 1-second resolution. There are three temperature sensors per panel type, which are PT1000 adhesive sensors [46]. These sensors consist of a sensor element placed in an aluminum cuboid that is glued to the back of the PV modules. According to the datasheet, they have

a measuring range from -20 °C to 70 °C, and have a measurement accuracy of 1% [46].

From each rack, we also have measurements of the irradiance in the POA of the module, these measurements are carried out with reference cells of the type SI-series [47]. Irradiance received in the POA is also measured at two locations by pyranometers of the type SMP10 [47]. The GHI is also measured by a SMP10 pyranometer placed in the horizontal plane. We also have measurements from a WS500-UMB Smart Weather Sensor placed at 5 meters height, which measures temperature, relative humidity, air pressure, wind direction, and wind speed [48].

3.1.2 Gålå test site

The PV test site at Gålå is located at 61.512°N, 9.787°E at approximately 1000 meters above sea level [49]. The test site consists of two module types, one bifacial and one monofacial. In the test site, there are two modules of each type next to each other, as shown in Figure 3.1.3. The modules are installed in an open rack configuration with a tilt of 30° facing due south with an azimuth of 180°. In front of the monofacial modules, a weather station is placed, consisting of various weather measurement tools.

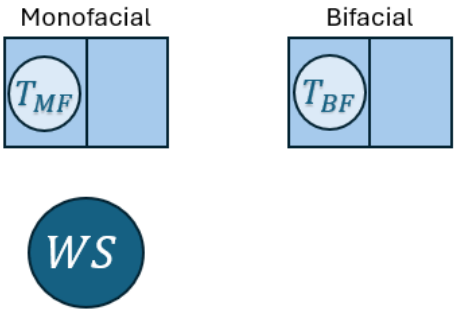

Figure 3.1.3: Map of the outdoor PV test site at Gålå. Note that the relative placement of the different module types and measurement tools is approximate. "WS" denotes the weather station with reference cells, pyranometers, an anemometer, and a temperature sensor. The backside temperature sensors are annotated with a "T".

The measurements were carried out between October 1st, 2023, and December 30th, 2024. All measurements of temperature and weather parameters are given as 10-minute mean values. The key properties of the modules are listed in Table 3.1.2. The module data sheets do not state explicitly that the modules are of PERC cell technology. Still, it is a reasonable assumption based on the year of production, and the two modules are hereby referred to as Mono PERC C and Bifacial PERC C.

The weather station features three reference cells of the type Si-mV-85, two of which measure the irradiance in the module planes and one measures the backside irradiance for the bifacial modules [52]. Additionally, there are four pyranometers of the type MS-80S, measuring the Global Horizontal Irradiance (GHI), Global Tilted Irradiance (GTI), Global Vertical Irradiance (GVI), and Global Reflected Irradiance (GRI) [53]. The weather station also includes an anemometer of the type NRG 40, measuring the wind speed at a height of 3.9 m [54]. The ambient temperature is

Figure 3.1.4: Image showing the PV test site at Gålå. The rack to the left is the two Mono PERC C modules, while the rack to the right are Bifacial PERC C modules. Photo: IFE

Table 3.1.2: Key properties of the module technologies in the PV test site at Gålå [50, 51].

Manufacturer	Cell technology	Features	Dimensions	Installed NOCT	Temperature coefficient of power
E	Mono PERC C	Full cell	1778×1057 mm	45 ± 2 °C	-0.40 %/°C
E	Bifacial PERC C	Full cell	1782×1061 mm	46 ± 2 °C	-0.47 %/°C

measured by a temperature and relative humidity sensor of the type HygroVue5 [55]. The module temperatures are measured by PT100 sensors adhered to the back of the modules [56].

3.2 Data Quality

To ensure good datasets for testing and improving the models, a set of quality checks was done before the analysis. This was done to avoid problems, such as unphysical measurements, stale values, faulty sensors, or drift. The datasets were visually inspected and filtered using functionality embedded in version 0.2.0 of the open-source Python library `PVAnalytics`. The `PVAnalytics` library was used to quality check the data, and to remove any values that indicate incorrect measurements, like stale values or unphysical weather measurements. It is a Python library for quality control, filtering, feature labeling, and other tools supporting data analysis for PV systems. The quality module in `PVAnalytics` contains several submodules for data quality checks for different PV system data. This section is based on Ref. [57].

3.2.1 Gap detection

The *quality.gaps* submodule has functions that identify gaps in the data, such as missing or stale values. The function `quality.gaps.stale_values_diff` was used

to detect any stale values in the data. The default values were kept, meaning that 6 consecutive unchanged data points indicate stale values, and that all stale values except the first in each window are marked as stale. We also have a relative tolerance of 1e-5 and an absolute tolerance of 1e-8 for detecting a change in the values. This means that two consecutive measurements, a and b, are detected as unchanged if

$$|a - b| \leq (tol_{abs} + tol_{rel} \cdot |b|), \tag{3.1}$$

where tol_{abs} and tol_{rel} are the absolute and relative tolerances [58].

3.2.2 Check of weather parameters

The weather module contains several quality checks for weather data, by checking if the values are physically plausible. `quality.weather.relative_humidity_limits`, `quality.weather.temperature_limits`, and `quality.weather.wind_limits` are functions that check if the measurements for, respectively, relative humidity, ambient temperature, and wind speed are within any set boundaries. As the relative humidity is a percentage, this ensures that it is a number between 0 and 100. The boundaries for the ambient temperature and the wind speed were based on the recorded temperatures and wind speed by the Norwegian Meteorological Institute (MET) [59].

3.2.3 Finalizing the dataset

After the removal of data points filtered out by the `PVAnalytics` functions, a resampling was performed to get hourly data as required by the temperature models presented in chapter 2. The hourly value was set as the mean value of all measurements done within the hour. As we have removed data points in our quality assurance, we want to ensure that all hourly values are the mean of values spread throughout the hour. To do this, a demand for at least 8 valid measurements of all relevant features within an hour was set when resampling the data. For the Gålå data, this demand was set to 4 instead of 8 valid measurements, as it is on a 10-minute basis. All hours with fewer measurements were not included in the filtered dataset.

3.3 PVlib

`PVlib` is a community-developed toolbox for PV system modeling implemented in Python, providing functions and classes for simulating the performance of photovoltaic energy components and other related calculations. The library includes implementations of solar position algorithms, thermal models, irradiance models, and PV electrical models [60].

3.3.1 Weather study

This section is based on Ref. [61]. `PVlib`'s location class objects have containers for latitude, longitude, timezone, and altitude. A location object was created for each of the two PV test sites. These were used to calculate the clearsky conditions at the given locations by using the class function `get_clearsky()`. The `get_clearsky()`

function estimates the clearsky GHI, DNI, and DHI at the location given. The function allows for the usage of different clearsky models, and the default model, Ineichen, was used. `PVlib` also has a function, `irradiance.clearsky_index` that calculates the clearsky index, which is the ratio of measured horizontal irradiance and the modeled clearsky GHI.

3.3.2 Temperature models

`PVlib` has implemented several models for estimating the PV module and cell temperature from other, more commonly available measurements. These implementations were used for the models studied in this project. This section is based on Ref. [23].

Input parameters for the temperature models

Table 3.3.1: Input parameters for the temperature models in the `PVlib` implementation.

Model	G_{poa} [W/m^2]	T_a [°C]	v [m/s]	Additional parameters
`sapm_module`	X	X	X	a, b
`faiman`	X	X	X	U_0, U_1
`faiman_rad`	X	X	X	ir_down, U_1, U_1, sky_view, $emissivity$
`fuentes`	X	X	X	$noct\_installed$, $module\_height$, $wind\_height$, $emissivity$, $absorption$, $surface\_tilt$, $module\_width$, $module\_length$
`pvsyst_cell`	X	X	X	u_c, u_v, $module\_efficiency$, $alpha\_absorption$
`ross`	X	X		$noct$

Table 3.3.1 shows the model parameters for the different temperature models used in the project. All models require the total incident irradiance and the ambient temperature, moreover, all models, except the Ross model, require the wind speed. As the models are developed for hourly data, all measurement data used in the testing are, as mentioned in Section 3.2.3, resampled to hourly data.

For the Sandia Array Performance Model (sapm_module) the a and b values were set to the values given in Table 2.3.1. For the Bifacial PERC B, the values for glass/glass modules with an open rack were used, while for the rest of the modules, the values for glass/polymer modules with an open rack were used.

For the Faiman model, the default values for U_0 and U_1 were used. However, for the Faiman model with a radiative term (faiman_rad), the values proposed by

Driesse were used; $U_0 = 2.74$ and $U_0 = 2.91$ [36]. For the radiative term we need the downwelling infrared radiation from the sky, which was retrieved from the era5 dataset. The sky_view variable was set using Eq. 2.20, where the θ in our case is 45° for the Kjeller test site, and 30° for the Gålå test site. For the emissivity, the default value of 0.88 was used, which represents the middle of a range of values found in the literature. During further parameter development of the Faiman model and the Faiman model with a radiative term, the values for the model parameters U_0 and U_1 are tuned to better fit the two data sets.

For the Fuentes model, the installed NOCT was needed, which is given in Table 3.1.1 for all module types except for the full cell IBC, where the default value was used. The model also uses the module width, length, height, and tilt, as well as the height at which the wind speed is measured. For the emissivity and absorption of the module, the default values were used.

For the PVsyst Cell Temperature model, all the additional parameters were set to the default values, and for the Ross Model the installed NOCT value was set as for the Fuentes model.

3.3.3 DC power model

To evaluate the effect that an improvement in the temperature estimation has on the DC power, the `PVlib` function `pvwatts_dc` was used. The model requires several input parameters: the irradiance transmitted to the cells, the cell temperature, the power of the modules at 1000 W/m^2 and cell reference temperature, the temperature coefficient of power, and the cell reference temperature. The last three were obtained from the module data sheet, while the irradiance transmitted to the cell and the cell temperature were assumed equal to G_{poa} and T_m.

3.4 Evaluation methods

To evaluate the models' performances, in addition to visual inspection, the following metrics were used: Root Mean Square Error (RMSE) and Mean Bias Error (MBE). Root Mean Square Error is given by

$$RMSE = \sqrt{\frac{1}{n}\sum_{i=1}^{n}(y_{pred,i} - y_i)^2}, \tag{3.2}$$

and shows the square root of the average squared error for the model predictions [62]. The Mean Bias Error is given by

$$MBE = \frac{1}{n}\sum_{i=1}^{n}(y_{pred,i} - y_i), \tag{3.3}$$

which shows the average deviation, and thus, the bias in the error [62].

3.5 Parameter tuning

When tuning the models, we want to find the combination of the empirical parameters that leaves us with a model that estimates the temperature with the highest accuracy.

MSE was chosen as the objective function to be minimized, given by [62]

$$MSE = \frac{1}{n}\sum_{i=1}^{n}(y_{pred,i} - y_i)^2. \tag{3.4}$$

It can be shown that MSE can be rewritten as the sum of the variance and the squared bias [63]. As a high bias can lead to underfitting, and a high variance can lead to overfitting, using the MSE as an objective function in the minimization seems reasonable.

The `SciPy Optimize` library provides functions for minimizing or maximizing functions, and includes solvers for nonlinear problems, linear programming, constrained and non-linear least squares, root finding, and curve fitting. [64] The `minimize` function minimizes a function with respect to one or more variables. The L-BFGS-B algorithm was used for the minimization. As there is a risk of such optimization functions finding local minima, a simple grid search was performed in addition to the optimization function. By ensuring that the point found from the grid search is close to the optimization function, we can say with higher certainty that the point is a global minimum. The grid search was performed by creating a grid with combinations of the parameters, and finding the point giving predictions with the smallest MSE. For a point (i, j) found by the grid search, the search was then repeated in the area around this first point [i-1, i+1], [j-1, j+1] to get a more accurate result. If the grid search finds the same point as the `optimize` function, the values are kept as tuned parameters.

CHAPTER

FOUR

PREVIOUS WORK

As the work in this thesis is a continuation of the author's previous work in Ref. [10], a summary of the main findings and discussions of this project will be presented in this chapter for completeness.

The project thesis aimed to evaluate the performance of several commonly used temperature models for a PV system in a Nordic climate. The dataset used was the measurements from the outdoor PV test site at IFE, Kjeller, presented in Section 3.1.1, and the models tested were those presented in Chapters 2.3.1 – 2.3.6, i.e., (1) Sandia Array Performance Model, (2) Fuentes, (3) Faiman, (4) Faiman with an extra radiation term, (5) Pvsyst, and (6) Ross. The models were all tested using their default parameters, as this is a common practice in the PV industry today.

4.1 Data quality

To ensure high data quality for testing, a series of data quality checks was performed on the dataset. At first, a visual inspection of time series plots of the data was performed to look for any clear errors. An example plot from the visual inspection is shown in Figure 4.1.1, conveying the typical diurnal trend in the data for a clearsky day and two overcast days in summer 2022. Here we see the module temperature (blue curve) following the ambient temperature (red curve) quite closely in the early morning, but deviating when there is a high irradiance (green curve), making the module temperature significantly higher than its surroundings. At night, it drops below the ambient temperature, which can be due to a radiative loss. The visual inspection did not display any clear errors in the data.

The dataset was then filtered using data quality functions from `PVAnalytics`. A large number of irradiance measurements were identified as stale values, which is seemingly simply due to the irradiance being 0 at night. There were also stale values detected for other parameters. The dataset has 380,136 measurements, and for all module temperature sensors, around 500 measurements were filtered out, i.e., 0.13% of the data. By studying these, they seem like mostly stable temperatures, but to ensure a high data quality, they were removed. However, for the ambient temperature, 11,494 measurements were filtered out, i.e., 3% of the data. Figure 4.1.2 shows examples of temperature measurements that were filtered out. Here, it is hard to determine if we simply have a stable temperature or a stale value. As it is

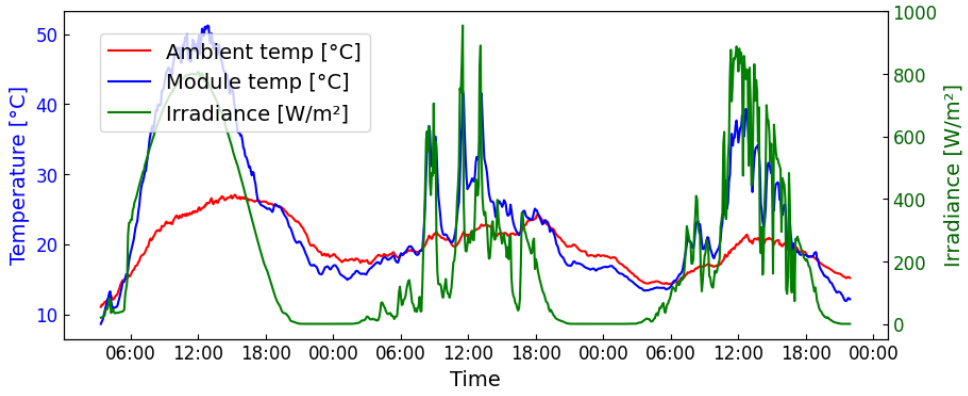

Figure 4.1.1: An example plot from the visual inspection performed for the Kjeller dataset. The measured ambient temperature, module temperature, and irradiance are plotted for 2022-06-30, 2022-06-31, and 2022-07-01. The measured module temperature is for the Mono IBC cell technology. Taken from [10].

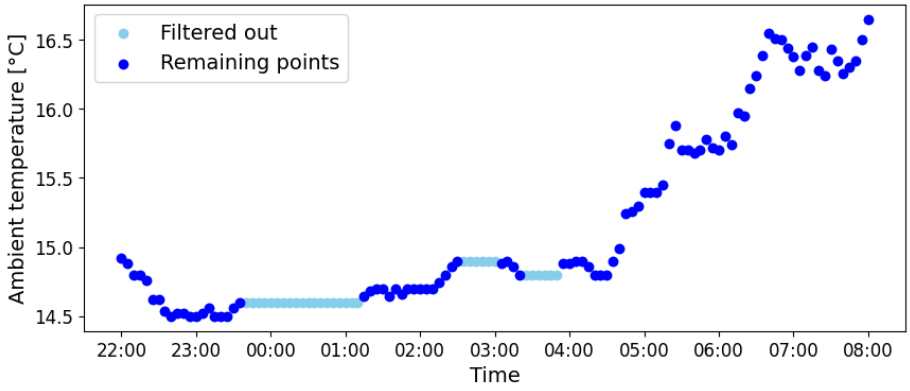

Figure 4.1.2: 5-minute mean measurements of the ambient temperature, compared to the remaining points after the application of the filter for stale values. The displayed time period is the night between 2024-07-10 and 2024-07-11.

still a relatively small fraction of the total measurements, it was decided to remove them from the dataset. All detected values were removed for the other parameters as well, to ensure all stale values are removed. The weather filters, on the other hand, did not detect any data points with nonphysical values, meaning that all values were within the set boundaries.

4.2 Weather study

A weather study was done before the model evaluation to ensure that we were looking at representative days when studying time series data. The data set at a 5-minute resolution was used to calculate a daily clearsky index and a daily variability index. The daily clearsky index indicates how close the day was to a perfect clearsky day, and the variability index indicates how much the clearsky index varies throughout the day. Three consecutive days with different weather were chosen for use in the evaluation: one cloudy day (low clearsky index), one day with variable weather (high variability index), and one day with nearly perfect clearsky conditions (high clearsky

index). The three days are highlighted in Figure 4.2.1, showing that they are days with different weather conditions while still being representative.

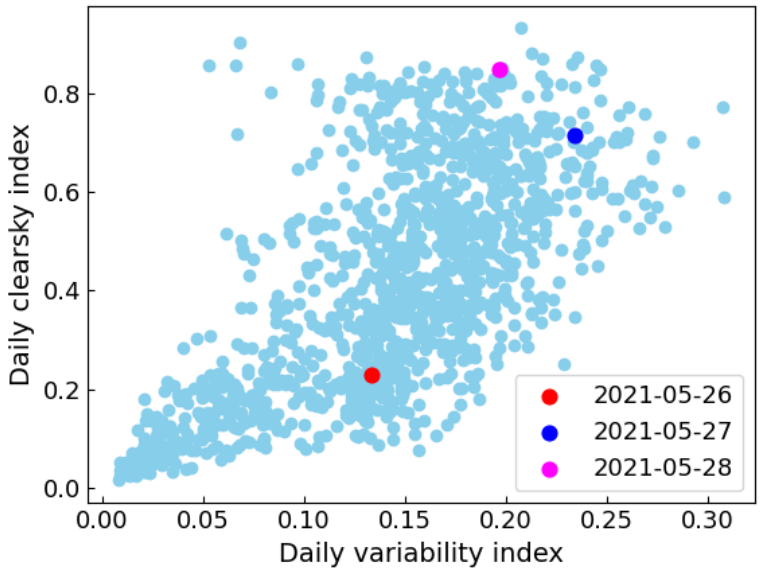

Figure 4.2.1: Every day in the data set is plotted as a function of its daily mean clearsky index and variability index. The three days 2021-05-26, 2021-05-27, and 2021-05-28 are highlighted in opaque colors. Taken from [10].

Figure 4.2.2 shows the three days highlighted in Figure 4.2.1 as a timeseries. Here we see the measured GHI compared to the estimated clearsky GHI for the location, as well as the clearsky index and daily variability in the lower panel.

A study of other weather parameters in the dataset from the PV test site at Kjeller is presented in Table 4.2.1.

Table 4.2.1: The minimum, mean, and maximum value for the ambient temperature, wind speed, and relative humidity for the measurements performed at the PV test site at IFE Kjeller. The values are for the measurements with a 5-minute resolution performed from the 1st of January 2021 until the 12th of August 2024. Reproduced from [10].

Weather parameter	Minimum value	Mean value	Maximum value
Ambient temperature [°C]	-26.16	6.62	29.44
Wind speed [m/s]	0.0	1.82	12.74
Relative humidity [%]	11.58	74.12	100.0

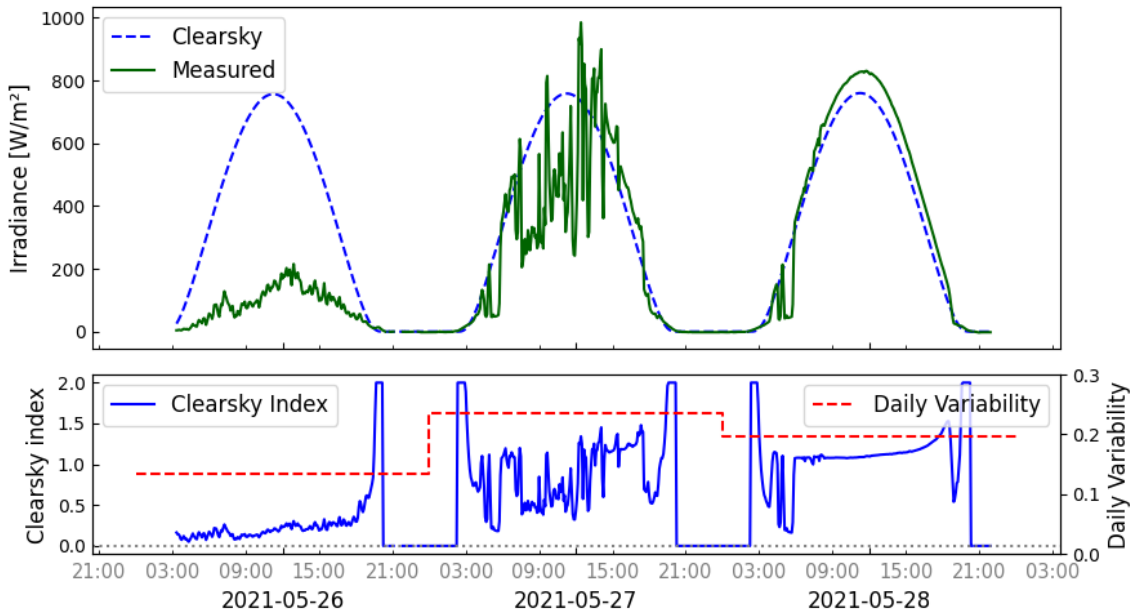

Figure 4.2.2: Comparison of measured GHI and the estimated clearsky GHI at a 5-minute resolution for the three days 2021-05-26, 2021-05-27, and 2021-05-28. The lower panel shows the corresponding clearsky indices and the daily variability. Taken from [10].

4.3 Measurement uncertainty study

As the Kjeller data set has three temperature measurements for each module type, a study of measurement uncertainty was performed to assess the significance in different sensor positions and differences between modules. The three temperature sensors are placed on different panels in each rack, and it is therefore interesting to see if this causes a significant difference in the temperature. To study this, 5 days, including the three days found in Section 4.2 and the two following days, were studied.

The temperature sensors used in the test site have an uncertainty of $p_T = \pm 1\%$ of the temperature measured in °C, and a resolution of $2|\delta_T| = 0.1$ °C. Using uncertainty propagation, we are left with an uncertainty for each measurement T_i of

$$\sigma_{T_i} = max(|\delta_T|; |\delta_T| + |p_T| \cdot T_i) \tag{4.1}$$

[65]. For two temperature measurements T_i and T_j, and their difference $f = T_i - T_j$, we then have a uncertainty of

$$\sigma_f = \sqrt{\sigma_{T_i}^2 + \sigma_{T_j}^2} \tag{4.2}$$

for the temperature difference [65].

Figure 4.3.1 shows the difference in the three measurements performed for the Mono PERC A modules. Figure 3.1.1 shows that T_1 and T_2 are measured at the top modules in the 2P configuration, whereas T_3 is measured for the lower module. The shaded area around the difference shows the estimated measurement uncertainty, meaning that if the differences are statistically insignificant, 0 should be within the uncertainty around the line. Looking at the plot, we see that for the measurements T_1 and T_2, the difference is centered around 0, usually being $\sim$0 at nighttime and

deviating during the day. We can therefore say that the difference is insignificant during the night and close to insignificant during the daytime. We do, however, see that the difference is significant during the day for high irradiances. We also see from the two lower panels that measurement T_3 is significantly different from the two other measurements most of the time. Similar behavior for the temperature measurements was also found for other module types, but there was no clear consistency between which measurement deviated from the others and their relative placement. As the cause of the differences is unknown, a decision to only use the measurements from the lower row in each rack was made to minimize any potential effects of different placements.

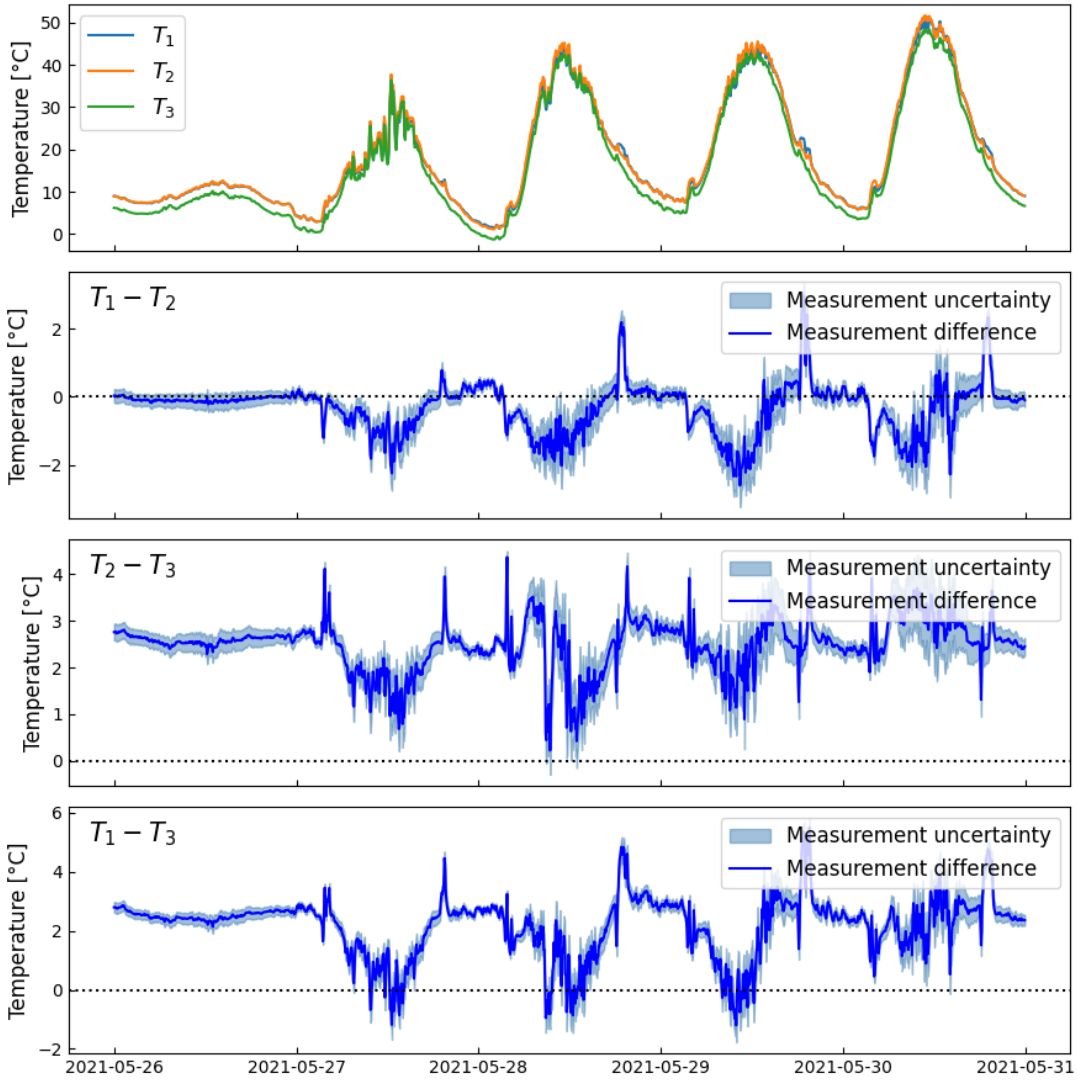

Figure 4.3.1: Comparison of three module temperature measurements done for the Mono PERC A modules. The upper plot shows the measurements, while the three plots below show the temperature difference between the combinations of these measurements, with their corresponding measurement uncertainty indicated by a shaded area. Taken from Ref. [10].

4.4 Bifacial and monofacial study

To investigate whether there are significant differences in the temperature behavior between bifacial and monofacial modules, we can do a similar analysis as in Section 4.3. The two bifacial module types will be studied to see if there is a similarity in temperature behavior despite the differences in material, as the Bifacial PERC A modules have a transparent backsheet, while the Bifacial PERC B modules have glass. We compare their temperatures to Mono PERC B, which, according to the datasheet, has many similar properties, e.g., half-cell technology, PERC cell architecture, and temperature coefficient of power. Figure 4.4.1 shows that all the measurement differences are statistically significant. We see that the differences are generally smaller

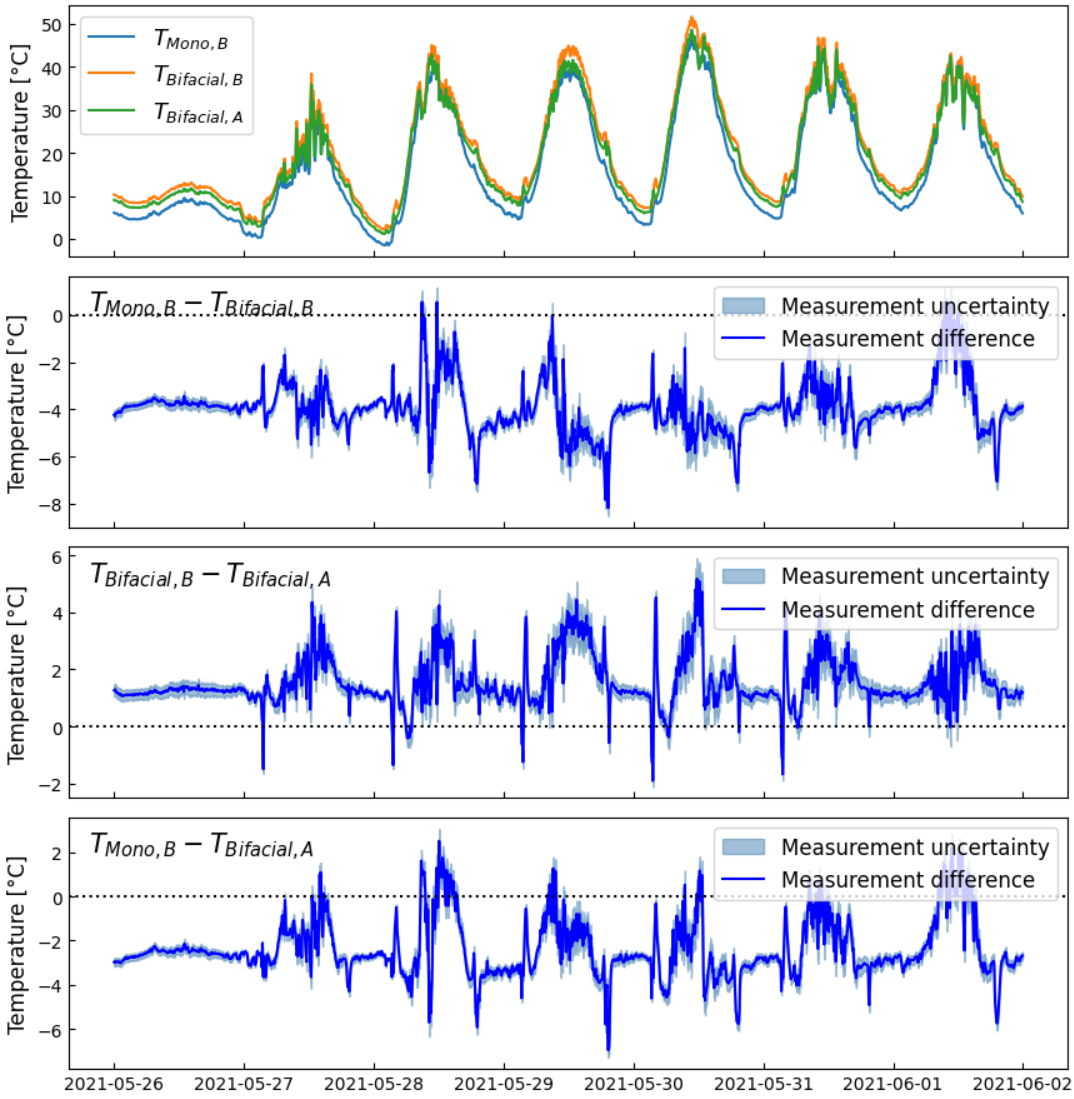

Figure 4.4.1: Comparison of three module temperature measurements done for a Mono PERC B module, a Bifacial PERC A module, and a Bifacial PERC B module. The upper panel shows the three measurements, while the three bottom plots show the temperature difference between the three combinations of the measurements, with their corresponding measurement uncertainty as a shaded area. Taken from Ref. [10].

between the two bifacial module types than with the monofacial module type. However, the differences found in Figure 4.4.1 are not bigger than some of the differences found in Section 4.3 between measurements done for the same cell technology. It is therefore difficult to say with certainty if the temperature behavior for mono- and bifacial modules is significantly different, to an extent where we would need a specific temperature model for bifacial modules.

4.5 Model performances

The 6 models presented in Sections 2.3.1 – 2.3.6 were implemented and tested for the 6 module types in the PV test site at Kjeller. The model estimates were then evaluated by comparing them to the measured module temperature. Figure 4.5.1 shows the comparison for the Mono PERC A module for three selected days with variable irradiance in May 2021. Here we see that all models tend to overestimate the temperature, as there is a clear bias throughout the three days, with estimated temperatures lying systematically higher than the measured temperature. We also see that the errors are generally bigger on the high-irradiance days, compared to the first day with a low clearsky index. We, however, see considerable differences between the model performances. On the cloudy day (2021-05-26), the Fuentes model has lower residuals than the other models throughout the whole day. The Fuentes model also performs well on the other days, but overestimates the temperature during midday with high irradiance. On the clearsky day (2021-05-28), we see that the Faiman model with a radiative term greatly overestimates the temperature, while the Sandia Array Performance model performs similarly as it does on the two prior days with different weather conditions. As the Sandia model seemingly has a relatively stable bias even with different weather conditions, it seems likely that this model could perform well with some parameter tuning. All in all, from Figure 4.5.1, we would expect the Fuentes model to have the lowest error, and the Ross model to have the highest error for the Mono PERC A module. We also see that the Fuentes model and the Faiman model with a radiative term lie significantly closer to the measured temperature at night. This can be related to that these models take radiative losses to the sky into account, and thereby allow for the module temperature to drop below the ambient temperature.

Figure 4.5.2 shows the model estimates and the measured temperature on the day 2021-05-28. The lower panel shows the wind speed, which explains much of the temperature behavior seen in the measured temperature. As an example, at 12:00, indicated by the vertical line, the temperature drops rapidly, as the wind speed doubles between 11:00 and 12:00. Looking at the model estimates, this temperature drop is captured by all except the Ross and the PVsyst models. As we know, these are the only models that assume constant wind in their default values, which is shown here to be too strict of an assumption for our dataset.

Time series plots showing the model performances for the remaining module types can be found in Appendix B.1. Much of the same behavior can be seen for the other modules, with some variation. As such a detailed visual inspection would be difficult to visualize for the entire period considered, we want to quantify the model performances in terms of RMSE and MBE. The RMSE and MBE were calculated for each model and each module type for easier comparison. Figure 4.5.3 shows

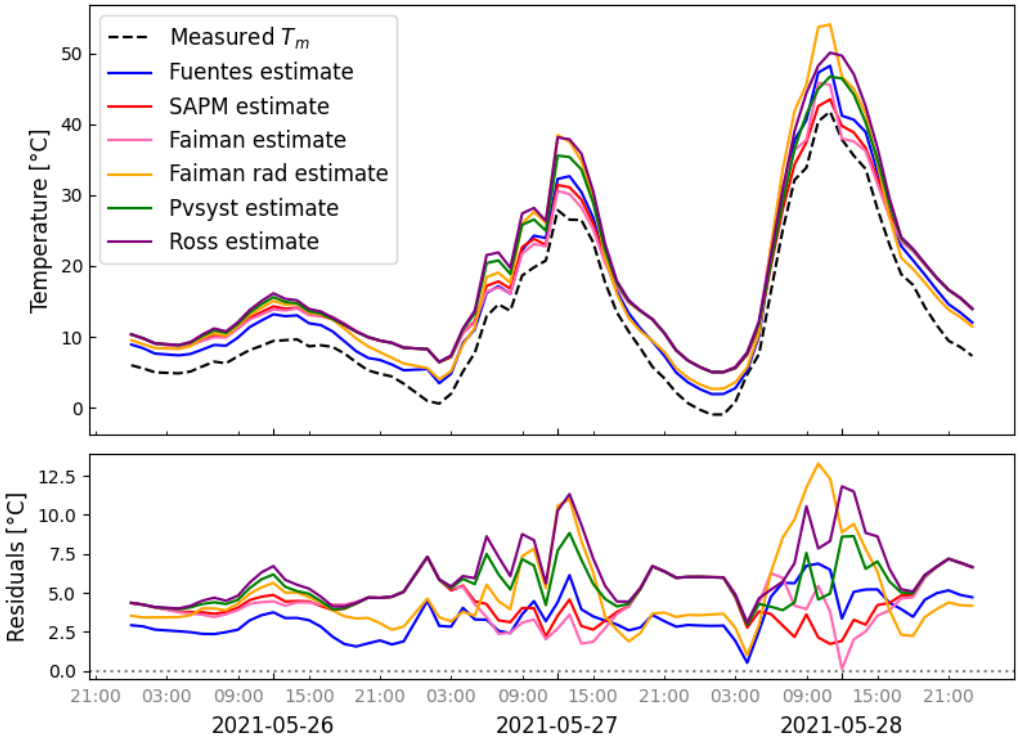

Figure 4.5.1: Comparison of the measured module temperature and the temperature estimated by the models implemented with their default parameters for module Mono PERC A. The lower panel shows the residuals for each model. Taken from [10].

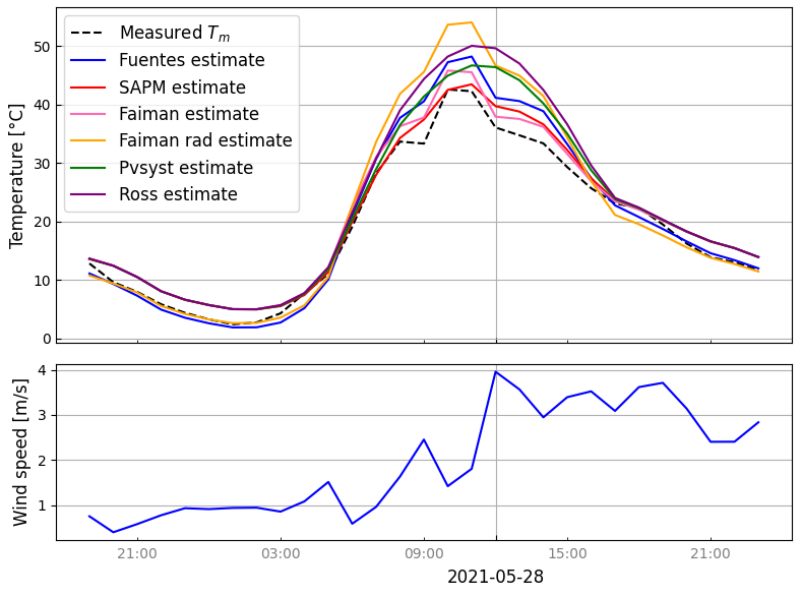

Figure 4.5.2: Comparison of the measured module temperature and the model estimates for a module with Bifacial PERC B cell technology, plotted for 2021-05-28. The lower panel of the figure shows the corresponding wind speed. The vertical line indicates 12:00. Taken from [10].

each model as a function of its RMSE and MBE for each module type. A perfect

temperature estimation would give a point in (0,0). Figure 4.5.3 shows that for all module types, the Fuentes model performs significantly better than the other models. We also see that for all monofacial modules, the Ross model performs the worst with default parameters, while for the bifacial modules, the Faiman model with a radiative term has the worst performance. We also see a lower error in the estimates for bifacial modules than for monofacial modules, indicating that there might be a difference that should be taken into account.

A surprising result is that the Faiman model performs better than the Faiman model with a radiative term, as the radiative term is added as an improvement to the original model. We would expect it to perform significantly better due to the extra complexity added to the model by the radiative term. It would therefore be interesting to see if this still would be the case with tuned model parameters for both models.

We also see that the Ross and PVsyst models generally have a worse performance than the other empirical models. As we suspected from Figure 4.5.2, the assumption of constant wind could be a source of error.

In the time series plots in Figure 4.5.1 and in Appendix B.1, we saw a positive bias in the models with default parameters. This corresponds well with the results presented in Figure 4.5.3, as we see a trend of a positive MBE, with just one exception, being the Fuentes model for the Bifacial PERC B cell technology. This clear bias indicates that tuning the empirical parameters of the models could improve their performance.

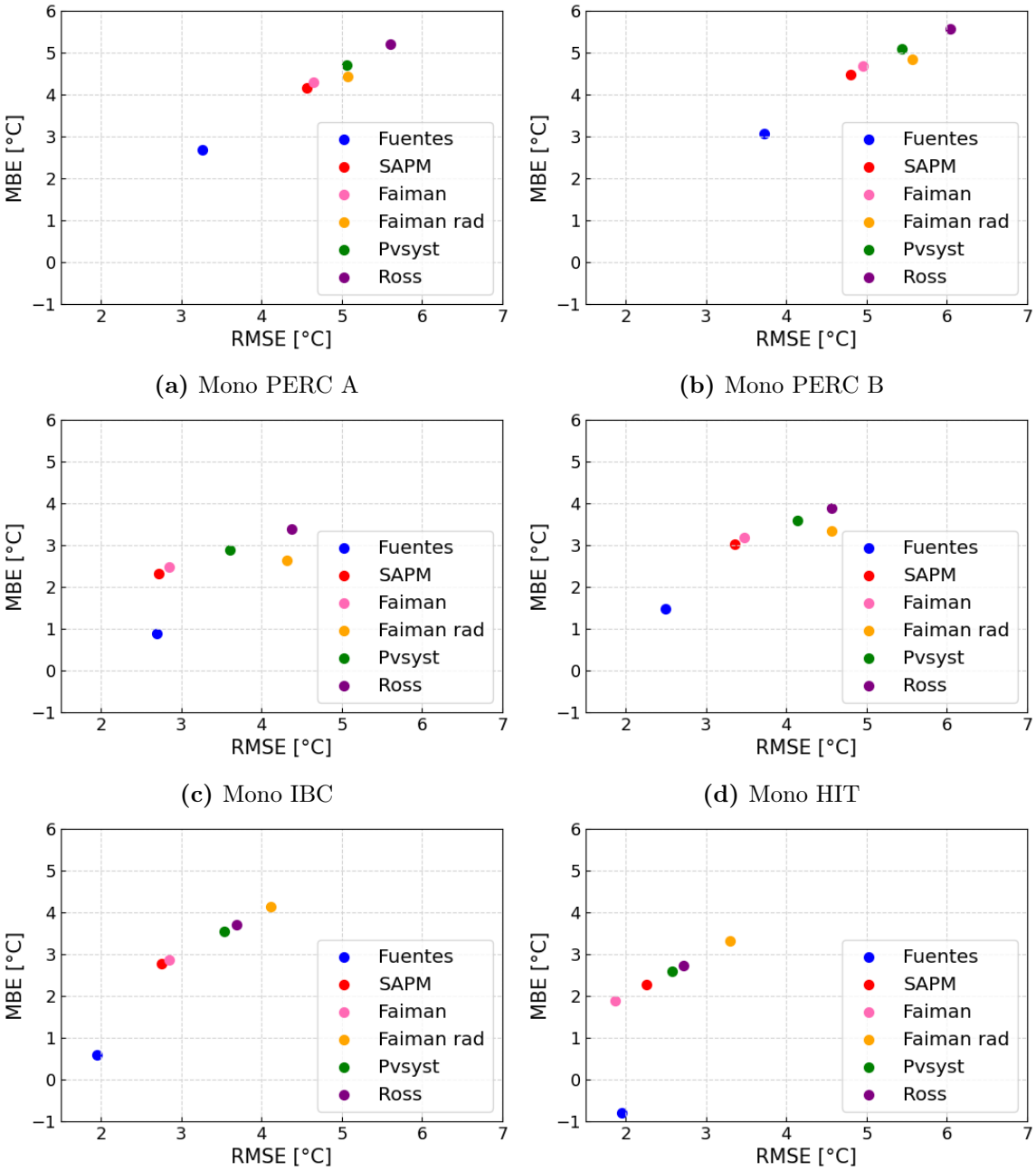

(a) Mono PERC A

(b) Mono PERC B

(c) Mono IBC

(d) Mono HIT

(e) Bifacial PERC A

(f) Bifacial PERC B

Figure 4.5.3: The RMSE and MBE of the different models for Mono PERC A, Mono PERC B, Mono IBC, Mono HIT, Bifacial PERC A, and Bifacial PERC B module technologies installed at Kjeller are shown in Figures (a) – (f), respectively. The models tested are the Fuentes model, Sandia Array Performance Model (SAPM), Faiman model, Faiman model with a radiative term (Faiman rad), PVsyst cell temperature model, and the Ross cell temperature model. Taken from [10].

4.6 Summary of project thesis results

The project thesis has evaluated the performance of 6 commonly applied models for estimating the operating temperature of PV modules, using over 3 years of data from the outdoor PV test site at IFE, Kjeller, Norway, with 6 different module technologies. The results show that there are significant errors between the measured and modelled temperatures when the module temperature is estimated using their default parameters.

As we see that the empirical formulas have a clear bias, all overestimating the temperature, it is believed that tuning the model parameters could improve their performance greatly. The empirical models have default parameters determined for PV test sites localized in different climate conditions than the test site at Kjeller, and a climate-specific set of parameters could therefore be beneficial for the model performances. It is proposed to do a parameter tuning for one of the simple empirical modules with wind-dependency, i.e., Faiman or SAPM, and the Faiman model with a radiative term, to see if these can perform similarly to or better than the Fuentes model. It was also proposed to study whether technology- or site-specific parameters could improve the performance further.

CHAPTER

FIVE

RESULTS AND DISCUSSION

5.1 Data quality

The data quality analysis performed in Section 4.1 was reused in this thesis for the Kjeller dataset. The stale value filter was, however, not applied to the irradiance columns. This was done as we expect the irradiance to be stable at nighttime.

5.1.1 Gålå data quality

To ensure a high data quality, the `PVAnalytics` functions described in Section 3.2 were applied to the Gålå dataset. This was already performed for the Kjeller dataset, as described in Section 4.1. As for the Kjeller dataset, there were no unphysical values detected for the ambient temperature, wind speed, and relative humidity. However, the `quality.gaps.stale_values_diff` function detected some stale values. As the irradiance is expected to remain stable at night, the stale value filter was only applied to the wind speed and the different temperature measurements. For the data set of 65,802 measurements, 41, 56, and 43 measurements were filtered out for the ambient, bifacial, and monofacial temperature, respectively. This is less than 0.09% of the data. However, for the wind speed, 5,748 stale values were detected, i.e., 9% of the data. Figure 5.1.1 shows a 6-day period with many detected stale values. The detected stale values remain stable at 0.39 m/s for long periods up to a full day, which seems unrealistic. All stale values are therefore removed from the dataset before further model evaluations and development.

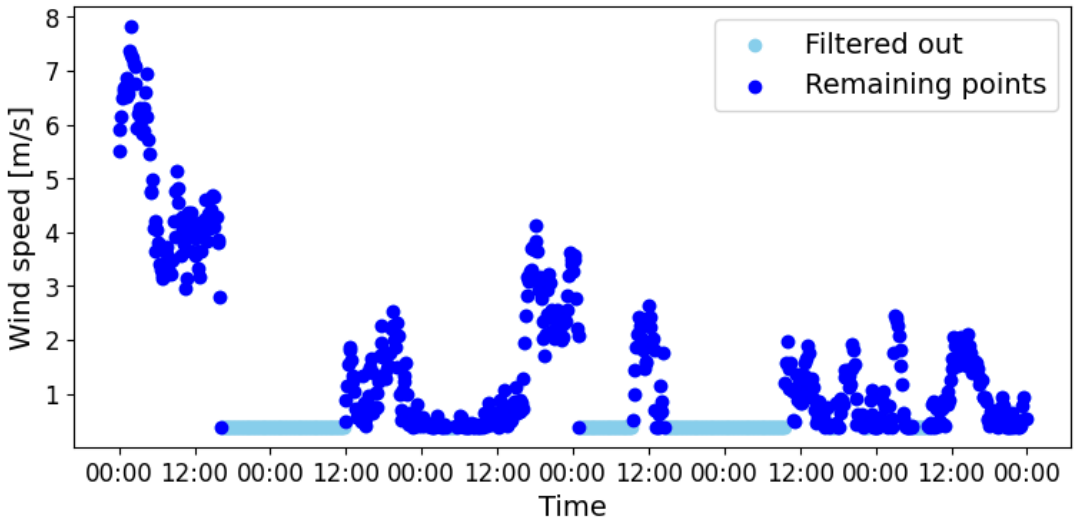

Figure 5.1.1: Wind speed measurements on a 10-minute resolution, where the measurements filtered out by the stale value filter are indicated by a light blue color. The period shown is 2024-03-01 – 2024-03-06.

5.2 Weather studies

As was performed for the Kjeller data set in Chapter 4, a weather study was performed for the Gålå data set. As the Kjeller and Gålå locations can have completely different weather, we need to find a new set of representative days for studying time series data specifically for Gålå. Figure 5.2.1 shows all days in the Gålå data set in a scatter plot, placed by their daily mean clearsky index and variability index. We

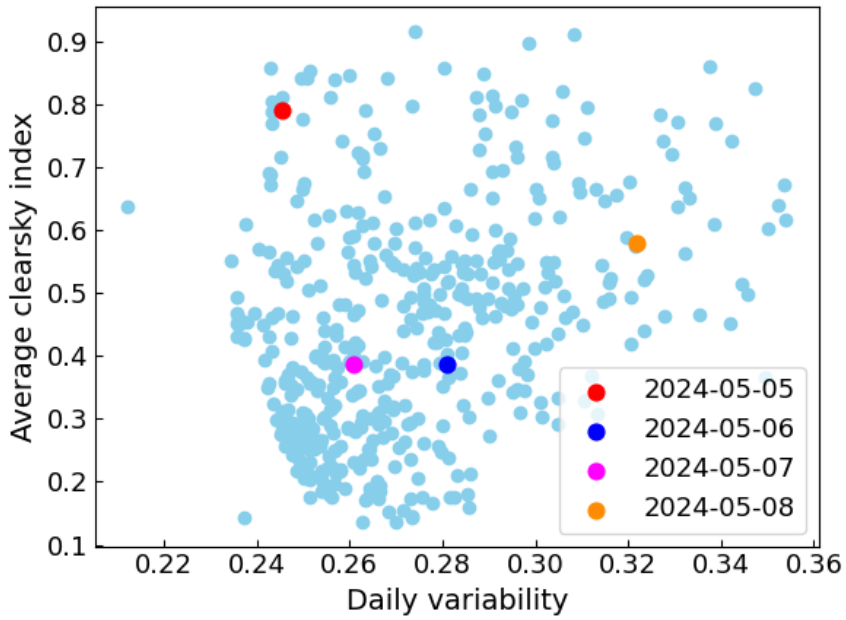

Figure 5.2.1: All days in the data set as a function of their average clearsky index and their variability index. The four days highlighted are further discussed in the text.

see that we have daily clearsky indices varying between 0.13 and 0.92, and variability indices between 0.20 and 0.36. The days highlighted in bright colors are four consecutive days that were found to have varying irradiance.

The four days highlighted in Figure 5.2.1 are plotted in Figure 5.2.2, where we see their GHI plotted against a clearsky estimate of the GHI. We also see their clearsky and variability indices in the lower panel on a 10-minute resolution. From the two figures, we see that 2024-05-05 is a nearly perfect clearsky day, with a low variability in the clearsky index. The two following days, 2024-05-06 and 2024-05-07, are both cloudy, with a relatively low clearsky index and a slightly increased variability. The last day, 2024-05-08, is a variable day, with a significantly higher variability index. This leads us to believe that these four days are a suitable choice for studying model performances, as they allow us to examine the model's behavior under various irradiance conditions.

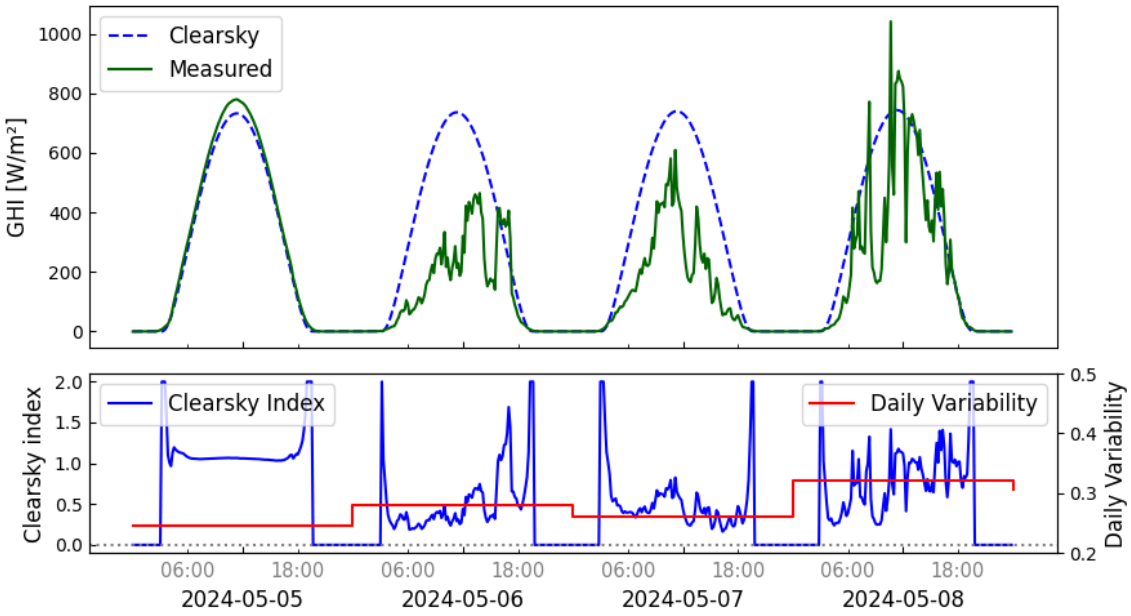

Figure 5.2.2: Measured GHI compared to the clearsky estimate of the GHI for the Gålå test site. The data is at a 10-minute resolution.

5.2.1 Comparison of weather conditions for Kjeller and Gålå

A summary of the range and mean ambient temperature, wind speed, and relative humidity is presented in Table 5.2.1 for the Gålå test site. We see that the PV test site at Gålå has a lower mean temperature, higher mean wind speed, and higher mean relative humidity than those found for the test site at Kjeller, which was presented in Table 4.2.1.

As we saw in Section 2.6, the two test sites studied in this thesis are also in two different Köppen–Geiger climate zones, Dfb and Dfc. To compare the two test sites further, Figure 5.2.3 compares the distribution of some central weather parameters measured at each test site. The distributions of the GHI, ambient temperature, wind speed, and relative humidity are plotted for each test site. The weather distributions for Kjeller are in the upper row, while the lower row has the distributions for the

Table 5.2.1: The minimum, mean, and maximum value for the ambient temperature, wind speed, and relative humidity for the measurements performed at the PV test site at Gålå. The measurements are at a 10-minute resolution.

Weather parameter	Minimum value	Mean value	Maximum value
Ambient temperature [°C]	-25.55	0.23	23.58
Wind speed [m/s]	0.39	2.48	12.78
Relative humidity [%]	24.33	83.88	100.00

corresponding measurements at the Gålå test site. For the GHI, the nightly values, i.e., GHI < 5 W/m^2, have been removed. We see that the relative frequency is reduced with an increasing GHI for both test sites, but with a slightly steeper gradient for the Gålå test site. This implies that high irradiances are somewhat less probable at Gålå. We also see that for temperature, the distribution for Gålå is centered around a lower temperature than for Kjeller. We observe that the ambient temperature distributions for both test sites are bimodal, possibly due to seasonal differences. We also see that the Kjeller test site reaches temperatures of up to 30 °C, while the Gålå temperatures do not reach higher than 24 °C, which can also be seen from the maximum temperatures in Tables 4.2.1 and 5.2.1. For the wind speed, we see that both test sites have a clear peak at under 1 m/s. We, however, see that the lowest values are not present in the Gålå data set as in the Kjeller data set. This might be due to the resolution, as the Kjeller data set is on a 5-minute resolution and thus can capture short-term conditions. Both test sites have similar maximum

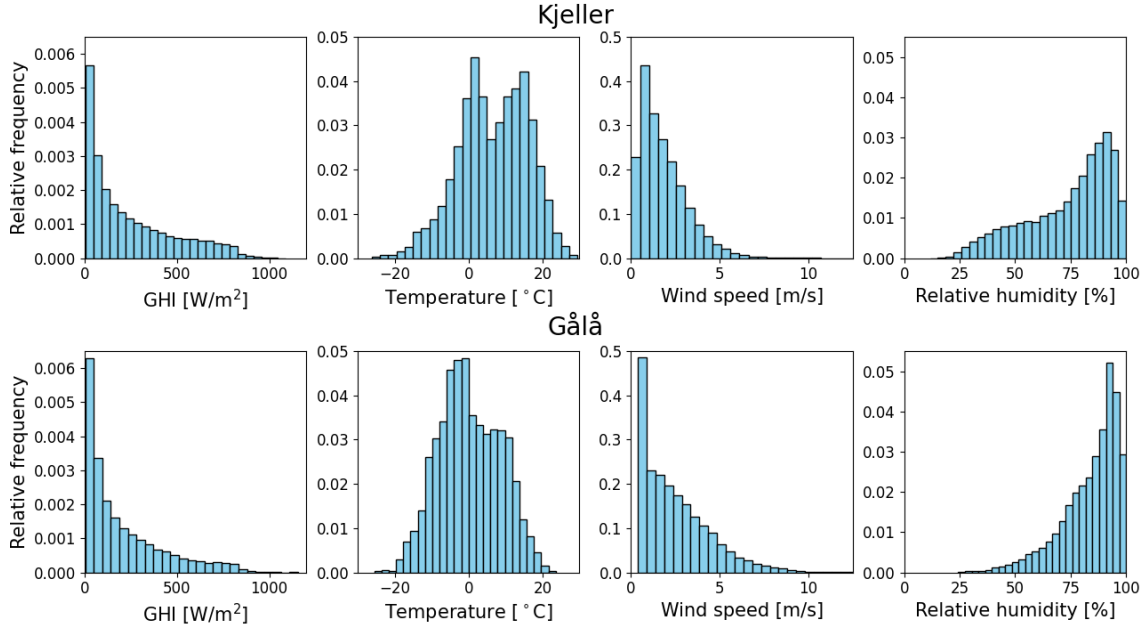

Figure 5.2.3: Histograms showing the distributions for the GHI, ambient temperature, wind speed, and relative humidity measured at each of the two test sites at Kjeller and Gålå. The Kjeller measurements are at a 5-minute resolution performed in the period 2021-01-01 – 2024-08-12, while the Gålå measurements are at a 10-minute resolution performed in the period 2023-10-01 – 2024-12-30. Note that the distributions have been normalized to facilitate comparison.

values, but the Gålå test site has a higher frequency of high wind speeds, explaining the higher average wind speed. For relative humidity, we see that both distributions peak at a similar value of around 90%, but that lower relative humidities have a higher frequency for Kjeller, while Gålå rarely has a relative humidity under 50 %. As a conclusion, Figure 5.2.3 shows that the Gålå test site has slightly lower GHI, lower temperatures, higher wind speeds, and higher relative humidity when compared to the test site at Kjeller. The differences are, however, generally not large, and a general Nordic model being suitable for both appears plausible.

5.3 Model performances with default values

To verify that the results seen in the project thesis were not a unique case for the PV test site at Kjeller, we want to perform a similar analysis for the data set from the test site at Gålå. Figures 5.3.1 and 5.3.2 show time series plots comparing the different model estimates with default parameters and the measured temperatures for the bi- and monofacial modules at the Gålå test site. We are studying the performances for the four days found in Section 5.2. Here we see that there is notably less bias compared to what we saw for the Kjeller test site, as the residuals are clearly more centered around 0. However, we see that most models have significant errors, especially during high irradiance.

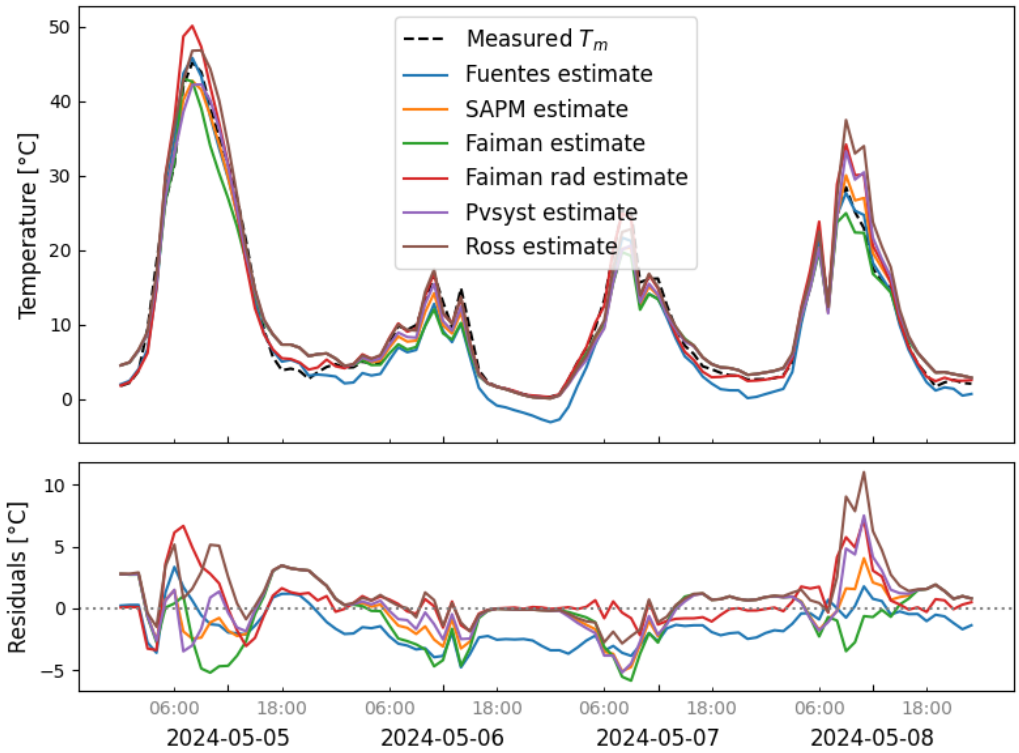

Figure 5.3.1: Comparison of the measured module temperature and the estimates from models with their default parameters, performed for module Bifacial PERC C at Gålå.

As we did for the Kjeller test site, RMSE and MBE are introduced to evaluate the models over the entire data set. Figure 5.3.3 shows a scatterplot of the RMSE

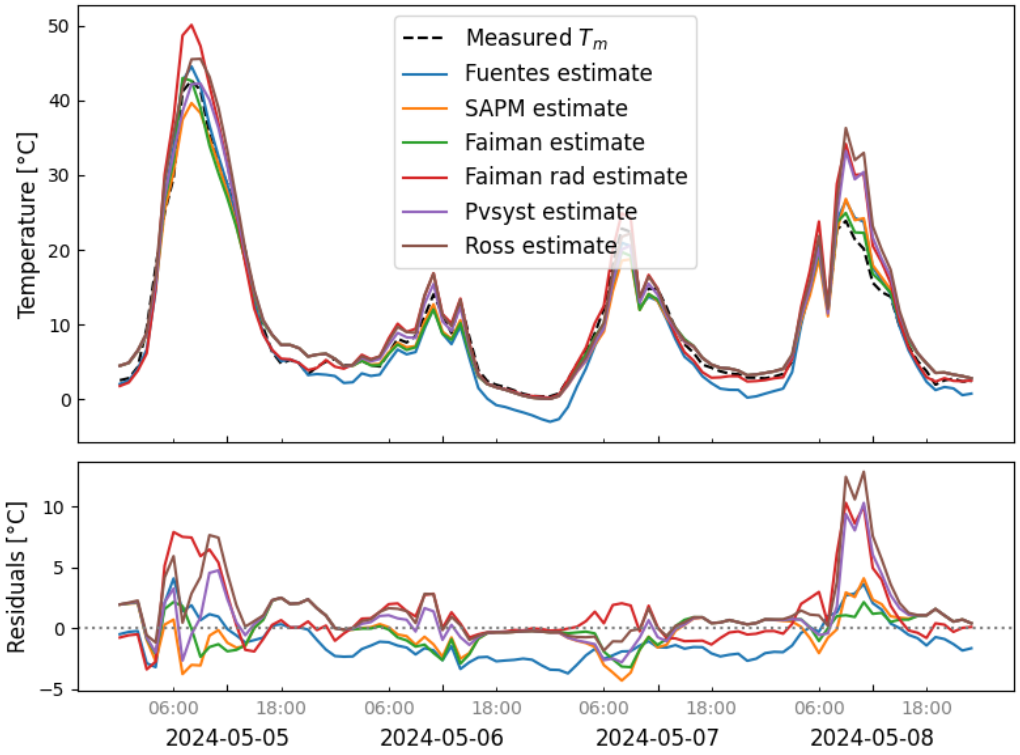

Figure 5.3.2: Comparison of the measured module temperature and the estimates from models with their default parameters, performed for module Mono PERC C at Gålå. The models tested are the Fuentes model, Sandia Array Performance Model (denoted SAPM), Faiman model, Faiman model with a radiative term (denoted Faiman rad), Pvsyst cell temperature model, and the Ross cell temperature model.

and MBE of each model for each of the two module types. As we suspected from Figures 5.3.1 and 5.3.2, we see here that the bias is lower than we saw for the Kjeller modules in Figure 4.5.3. We do, however, see a similar positive bias in all the empirical models. As we saw for the Kjeller test site, the worst-performing models are the Ross model, the PVsyst model, and the Faiman model with a radiative term. We also see again that the Faiman model performs significantly better without the radiative term, which is supposed to be an improvement to the original model. We therefore want to investigate whether this is due to different model parameters or if the radiative term does, in fact, add error to the model. All in all, from studying both the performances of all the temperature models with default parameters, it seems that parameter tuning the empirical models could improve their performance for PV systems in the Nordic climate.

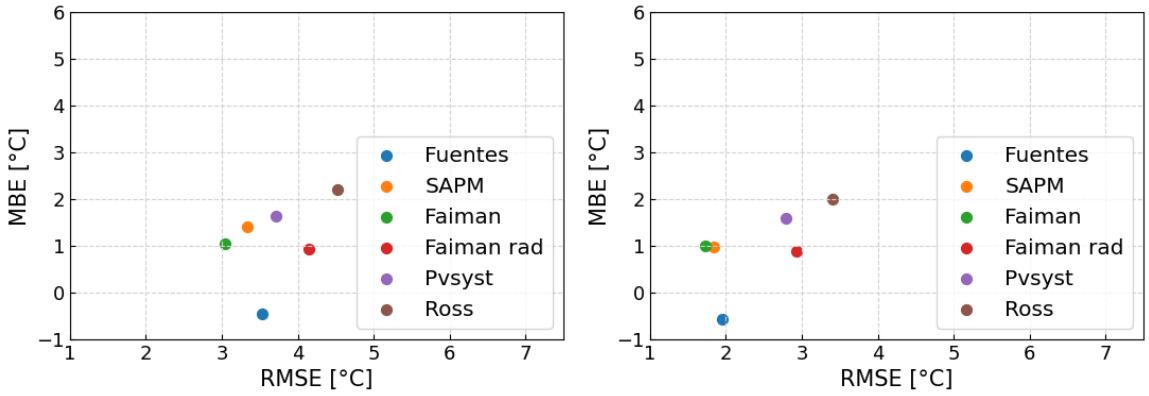

(a) Bifacial PERC C **(b)** Mono PERC C

Figure 5.3.3: The RMSE and MBE of temperature models for Bifacial PERC C and Mono PERC C modules installed at the Gålå test site are shown in Figures (a) and (b), respectively. The models tested are the Fuentes model, Sandia Array Performance Model (denoted SAPM), Faiman model, Faiman model with a radiative term (denoted Faiman rad), Pvsyst cell temperature model, and the Ross cell temperature model.

5.4 Snow filter

As we are studying test sites in the Nordic climate, there will be days present in the data set where the data is affected by snow. A layer of snow will greatly affect the module temperature, as it can cool or insulate the module itself, and block the irradiance, causing it to lose its heating effect. The effect of snow is not considered by the models, and therefore they will not be able to model its presence. As the models are dependent on irradiance measurements from which the snow might affect at different times than the modules, there might be inconsistencies between the measurements that can cause large errors. We therefore want to filter out days where we have snow covering the modules. However, snow cover is not tracked in our dataset, and it is therefore necessary to build a filter based on the other variables in the dataset. As an extra validation, daily values for snow depth and precipitation for each of the two locations were retrieved from senorge.no [66].

For simplicity, an assumption is made that all modules at each location have snow cover on the same days, as all modules are placed relatively close to each other and are tilted at the same angle. To identify the days when there is snow cover on the modules, power output data from the modules were studied. If the module is covered by snow, the power output should be lower than expected for the irradiance measured. Figures 5.4.1 and 5.4.2 show the data sets as scatterplots with irradiance and power output as variables. To more easily see a connection, the snow depth at the location is added as the color of the points. By studying the scatter plots in combination with time series data, a boundary was set for the power-to-irradiance ratio. The resulting boundaries are indicated by a red line in Figures 5.4.1 and 5.4.2. The resulting expression for Gålå was that if the power output is smaller than $0.22 \cdot G_{poa} - 5$, the point was identified as having snow cover. For Kjeller, this was set if the power output was smaller than $2.6 \cdot G_{poa} - 85$. The difference in magnitude is due to the power output data from Kjeller test site being from several series-connected

modules, while the Gålå power output is measured for single modules. In Figure 5.4.2, we see a number of points along the bottom of the plot, with a power of ∼0 W despite there being a nonzero irradiance and no snow. These points could be due to other factors, like shading of the modules. As the Kjeller modules are placed in an area surrounded by office buildings, while the Gålå modules are located in an open area, this seems like a reasonable explanation.

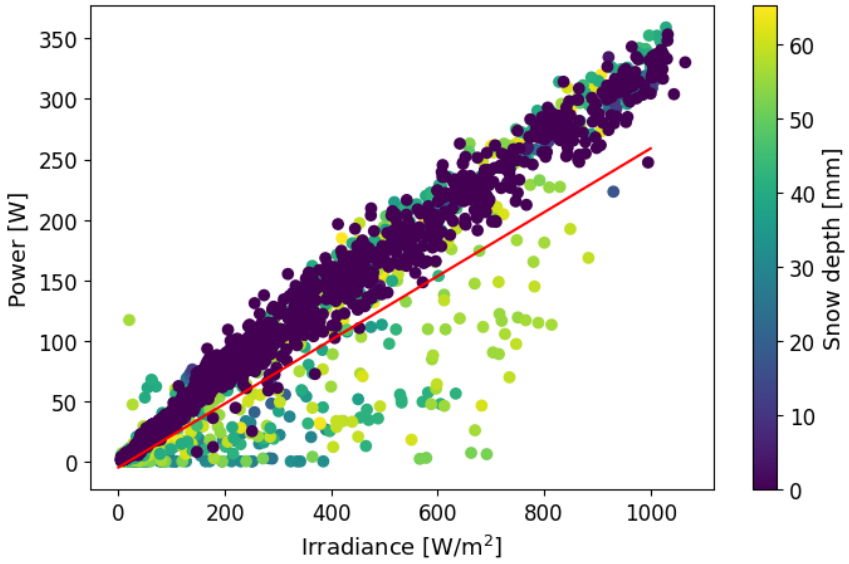

Figure 5.4.1: Hourly values for irradiance and power output plotted as a scatter plot. The color is determined by the snow depth, where a lighter color indicates more snow. The red line indicated the boundary set for the points to be identified as having snow cover. The module studied is Mono PERC C at Gålå.

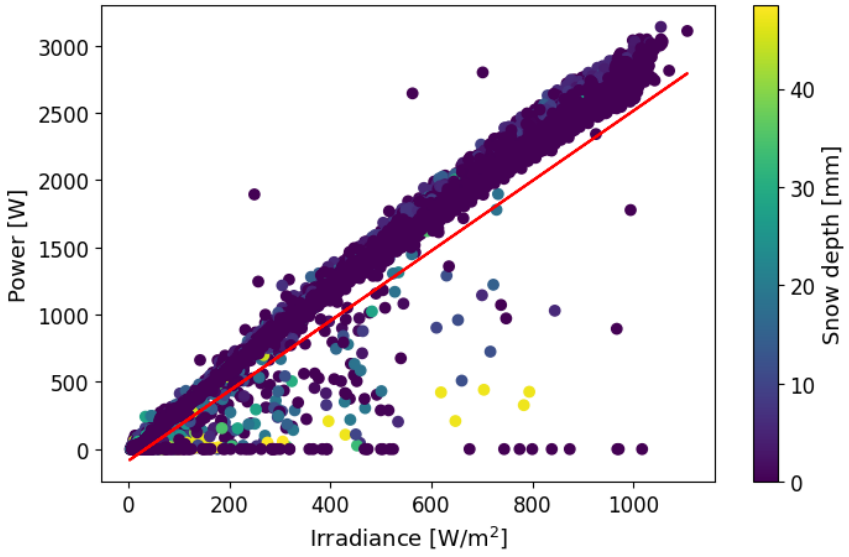

Figure 5.4.2: Hourly values for irradiance and power output plotted as a scatter plot. The color is determined by the snow depth, where a lighter color indicates more snow. The red line indicated the boundary set for the points to be identified as having snow cover. The module studied is Mono PERC A at Kjeller.

To identify the clear snow cover days, a demand was set that if the points were under the red line seen in Figures 5.4.1 and 5.4.2, and the snow depth at the location was nonzero, we identify that point as having snow cover. To be identified as a snow cover day, at least three hours throughout the day have to be snow cover hours. This is done to avoid removing whole days due to single hours with strange behavior.

There are, however, some potential weaknesses to this approach. The reference cells can also potentially have a layer of snow, giving low irradiance values. In these cases, the apparent power-to-irradiance ratio can still be realistic regardless of the snow cover. These points are hard to detect, and we might therefore still have some days with snow cover on the panels in the dataset. Ideally, one would have a more certain snow cover detection, such as camera detection [67]. We have, however, removed the days with the most obvious snow cover.

The assumption that all days with a low power-to-irradiance ratio are due to snow cover might not hold in all cases. Some of the cases might, for instance, be due to shading on the modules. This is somewhat accounted for when also demanding that the snow depth is nonzero. We could, however, still end up removing days where the low power output is due to factors other than snow cover. As for snow, the temperature models are unable to account for these factors, so removing the days filtered out before the parameter tuning still seems reasonable.

Figure 5.4.3 shows an example of how snow can affect measurements of irradiance and module temperature, as well as the estimated temperature with the Faiman model.

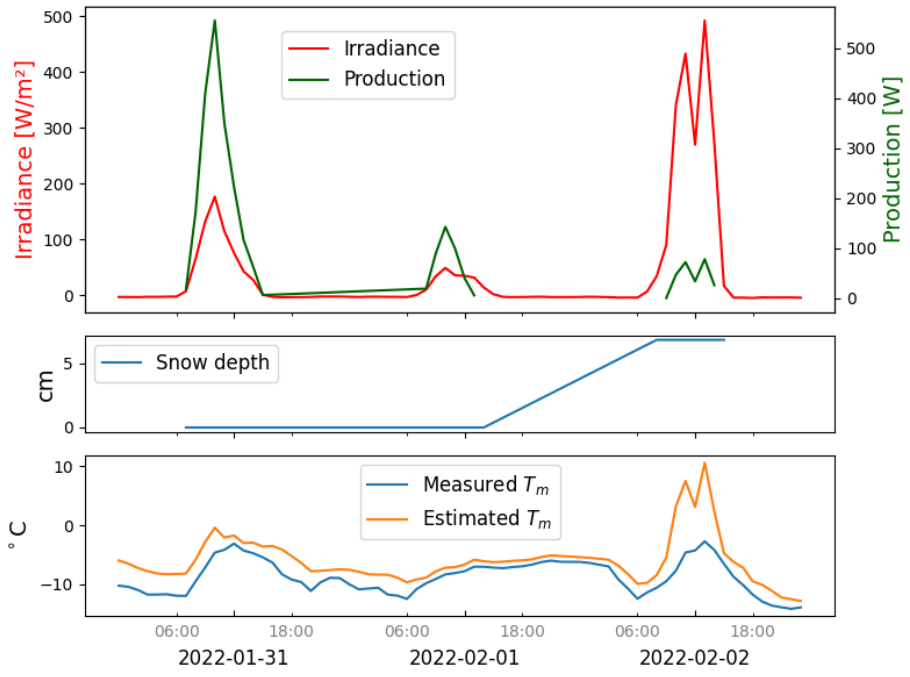

Figure 5.4.3: Irradiance and production plotted for the period 2022-01-31 to 2022-02-02 for the Mono IBC module at the Kjeller test site are shown in the top panel. The middle panel shows the daily snow depth measurement for the location, and the lower panel shows the measured and the Faiman estimate of the module temperature.

The middle panel shows the daily value of the snow depth, which we see increases from 0 cm on 2022-02-01 to well above 5 cm on 2022-02-02. Our snow filter has

detected 2022-02-02 as a day with snow cover, corresponding well with the behavior we see. Looking at 2022-01-31, we see that an irradiance of under 200 W/m^2 gives a production of over 500 W. On 2022-02-02, we see that even with an irradiance of up to 500 W/m^2, we have a power output of less than 100 W. Figure 5.4.4 shows an image taken of the PV test site at Kjeller on 2022-02-02, confirming that the behavior we see is due to snow cover. Having days like these in our dataset during parameter tuning will result in noise and affect the precision of the temperature models as the temperature behavior is affected. Looking at the lower panel in Figure 5.4.3, we see a comparison of the measured temperature and the Faiman estimate. Due to the high measured irradiance, which in reality is blocked by the snow cover, the Faiman model will overestimate the temperature a lot. We therefore want to avoid days like this in the dataset, and therefore remove the days with an abnormally low power output for the measured irradiance.

Figure 5.4.4: Image showing the PV test site at Kjeller, taken on 2022-02-02. Photo: IFE

5.5 Parameter tuning

As we have seen for the PV test site at Kjeller in Section 4.5, and Gålå in Section 5.3, there is seemingly a tendency of overestimation in all the empirical models. We therefore aim to investigate whether simple parameter tuning can enhance the models' performance to match or surpass that of the Fuentes model, which has outperformed the empirical models so far.

As explained in Section 2.4, the Faiman model, the Sandia Array Performance model, and the PVsyst model have identical or very similar characteristics and differ primarily in their parameterization. These parameters can be translated between the models, giving close to equivalent models [42]. Therefore, it was decided that incorporating all the models into the parameter tuning part of the thesis is unnecessary. Additionally, since we want to evaluate the performance of the Faiman model with a radiative term after parameter tuning, we will focus on the Faiman model. This choice allows us to determine whether the radiative term adds error, as observed with the default parameters, or if it improves the Faiman model when tuned for the

same data. The models were tuned using the `Scipy.optimize.minimize` function, with MSE as the objective function to be minimized [64]. To ensure that the function found the global minima, a grid search was performed to ensure that it found approximately the same point. The values from the minimize function were then chosen, as this has a higher accuracy than the grid search performed. All model parameters during the tuning were found by both the minimize function and the grid search. The models were tuned for

- All modules individually
- Only modules at the Kjeller test site
- Only modules at the Gålå test site
- Both test sites combined
- Only bifacial modules

For the tuning for both test sites combined, both test sites were weighted equally, despite there being more modules in the Kjeller test site. This was done as this parameter set is meant to be climate-specific, and we therefore want to weigh both locations equally. The parameter tuning was repeated for only the daytime data, meaning that a demand of an irradiance of at least 5 W/m^2 was set. This was done to study how much this will affect the performance during the daytime, as this is usually the most relevant due to there being no power production at night.

5.5.1 Parameter tuning of the Faiman model

The resulting parameters when tuning for all the data, meaning that both day- and nighttime data are included, and daytime data only, are given in Table 5.5.1.

Figure 5.5.1 shows the two sets of resulting parameters from tuning the Faiman model, as given in Table 5.5.1. We see that the parameters are, to some extent, similar, but that there are small changes between the parameters tuned for all data and for only daytime data. We see that some points are shifted to a higher U_1 for daytime data, e.g., Mono HIT, Mono IBC, and Mono PERC B, indicating a higher wind-dependency, but this is not evident for all the parameters, e.g., Bifacial PERC B, Bifacial PERC C, and Mono PERC C. Studying the figures, there are no clear trends in the points concerning their test site. The two Gålå modules, indicated by a blue color, lie far apart in the parameter space. The Kjeller modules, with a red color, are also widely scattered. This indicates that the location does not necessarily have a big effect on the best-fitting parameters. We also see that the three bifacial modules are spread out far, indicating that a separate model for bifacial modules might not be necessary. The default parameters do not deviate too much from the other parameters, but it is placed by the edge of the cluster, with the lowest U_0-value and a relatively low U_1-value. This leads us to believe that using tuned parameters, even a general set of parameters for the Nordic climate, could be reasonable. As the default parameters lie close to the tuned parameters for modules like Bifacial PERC B, we would expect the default model to perform better for this module than for modules like Mono HIT lying further away. Looking at Figure 4.5.3, we see that for Mono HIT the default Faiman model has an RMSE of around 3.5 °C and a MBE of

Table 5.5.1: Resulting model parameters for the Faiman model from the parameter tuning. Comparison of parameters tuned for all data and for daytime-only data (Irradiance > 5 W/m^2). The units are $W/m^2\,℃$ for U_0, and $W/m^2\,℃\,(m/s)$ for U_1.

Data set	All data		Daytime only	
	U_0	U_1	U_0	U_1
Kjeller	32.878	8.010	32.586	8.112
Gålå	32.726	6.578	32.719	6.579
Combined	33.385	7.111	33.236	7.120
Bifacial	30.797	7.296	30.946	7.252
Mono PERC A	36.821	6.351	36.577	6.429
Mono PERC B	39.433	7.440	38.775	7.653
Mono IBC	33.780	8.640	33.456	8.756
Mono HIT	33.470	9.076	33.021	9.237
Bifacial PERC A	29.555	9.035	29.413	9.087
Bifacial PERC B	26.384	7.595	26.317	7.620
Bifacial PERC C	39.530	5.063	39.524	5.064
Mono PERC C	27.051	7.855	27.044	7.856

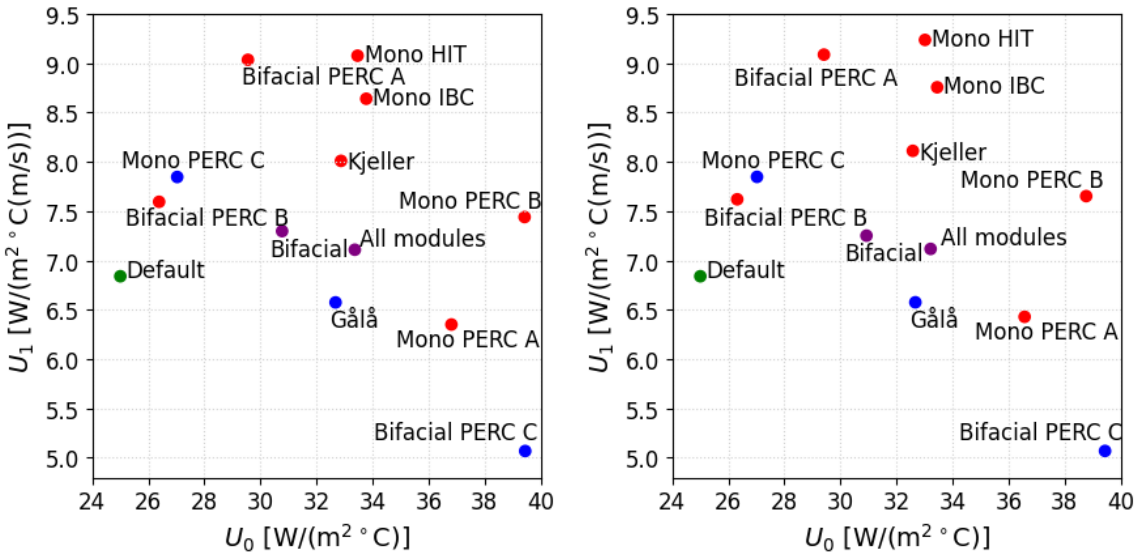

(a) Tuned for all data

(b) Tuned for daytime data

Figure 5.5.1: Tuned Faiman model parameters for different data. The model is tuned for each module individually, all Kjeller modules, all Gålå modules, all bifacial modules, and all modules combined, indicated by the annotations by each point. All Kjeller modules are red, while the Gålå modules are blue.

over 3 °C, while for the Bifacial PERC B both the RMSE and the MBE are under 2 °C. As some module-specific parameters are closer to the default parameters than the parameters tuned for both PV test sites, we can expect the Faiman model with a general Nordic set of parameters to perform worse than the default modules for some

modules. We, however, see that this will only occur for a minority of the modules, and it still seems like a better choice with a Nordic set of parameters.

5.5.2 Parameter tuning of the Faiman model with a radiative term

The Faiman model with a radiative term was tuned in the same manner as the Faiman model, as described in Section 5.5. The resulting parameters for all data and daytime data only are given in Table 5.5.2.

Table 5.5.2: Resulting model parameters for the Faiman model with a radiative term. Comparison of all data vs. daytime-only data (Irradiance > 5 W/m^2). The units are $W/m^2\,℃$ for U_0, and $W/m^2\,℃\,(m/s)$ for U_1.

Data set	**All data**		**Daytime only**	
	U_0	U_1	U_0	U_1
Kjeller	23.509	9.641	27.802	7.980
Gålå	28.456	6.303	28.764	6.187
Combined	26.501	7.691	28.870	6.844
Bifacial	25.781	7.435	27.262	6.890
Mono PERC A	23.607	9.226	30.683	6.569
Mono PERC B	23.766	11.021	32.128	7.827
Mono IBC	25.586	9.786	28.764	8.547
Mono HIT	22.636	11.208	27.786	9.148
Bifacial PERC A	22.346	9.985	25.382	8.779
Bifacial PERC B	22.712	7.483	23.320	7.230
Bifacial PERC C	34.755	4.907	34.930	4.803
Mono PERC C	23.263	7.462	23.629	7.353

Figure 5.5.2 shows the different tuned parameter sets for the Faiman model with a radiative term, tuned for all data and daytime data only. In contrast to Figure 5.5.1 for the Faiman model, we see a big difference in the parameters tuned for all data, and the parameters tuned for daytime data only. For most modules, especially the Kjeller modules, we see a shift towards higher U_0-values and lower U_1-values in the parameters tuned for daytime data compared to for all data. This indicates that the temperature during the day is less wind-dependent.

Another difference we see from the Faiman parameters is that we see a clearer difference between the Kjeller and Gålå modules. Especially when looking at the parameters tuned for all data, we see that the Kjeller modules cluster together quite nicely, while the Gålå modules are spread out more. We do, however, see that the Mono PERC C module lies closer to the Kjeller cluster than to the Bifacial PERC C cluster, so for the Gålå modules, a site-specific set of parameters is not necessarily a good fit. Again, we see that the three bifacial modules are spread out, indicating that tuning specifically for the bifacial modules is not needed. We also see that the default parameters are far away from all tuned parameter sets, indicating that we for all modules will benefit from a parameter tuning. Seeing how

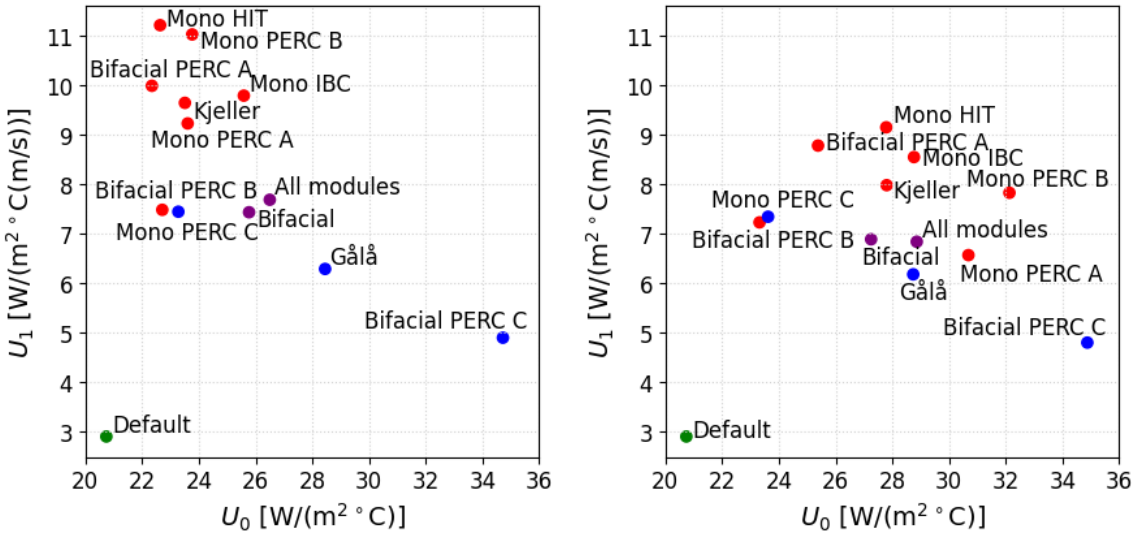

(a) Tuned for all data

(b) Tuned for daytime data

Figure 5.5.2: Tuned Faiman rad model parameters for different data. The model is tuned for each module individually, all Kjeller modules, all Gålå modules, all bifacial modules, and all modules combined.

far the default parameters are from the tuned parameters for the Faiman model with a radiative term, compared to the Faiman model, can be a possible explanation for why the Faiman model generally had a better performance when evaluating the default models in Sections 4.5 and 5.3. It is thus interesting to see if the Faiman model with a radiative term will perform better than the Faiman model with tuned parameters.

5.6 Driesse model with a low-pass filter

The Driesse model, presented in Section 2.3.7, is a model equivalent to the Faiman model with a radiative term with an added lowpass filter. This is added to account for the effect of the thermal mass. As we are generally studying hourly data in this thesis, and this is a common practice in PV modeling tools like PVsyst, it is potentially unnecessary to take the thermal mass into account. The model was, however, implemented, tuned for our data, and tested with and without the low-pass filter to study the effect of the filter. The lowpass filter was implemented as a simple running average filter applied to the input parameters, i.e., irradiance, temperature, wind, and downwelling infrared radiation from the sky.

Figure 5.6.1 compares the Driesse model estimates with and without an added low-pass filter, plotted along with the measured module temperature. Studying the figure, we see that the model without the low-pass filter captures the trends in the data better, while the low-pass filter adds a delay which makes the model performance worse during these days. As we expected, the effect of the thermal mass does not seem to be present in the hourly data, and thus, the low-pass filter simply adds extra error. It was therefore decided to not bring this model along for further tuning and testing.

However, in the derivation of the Driesse model, the product of the view factor

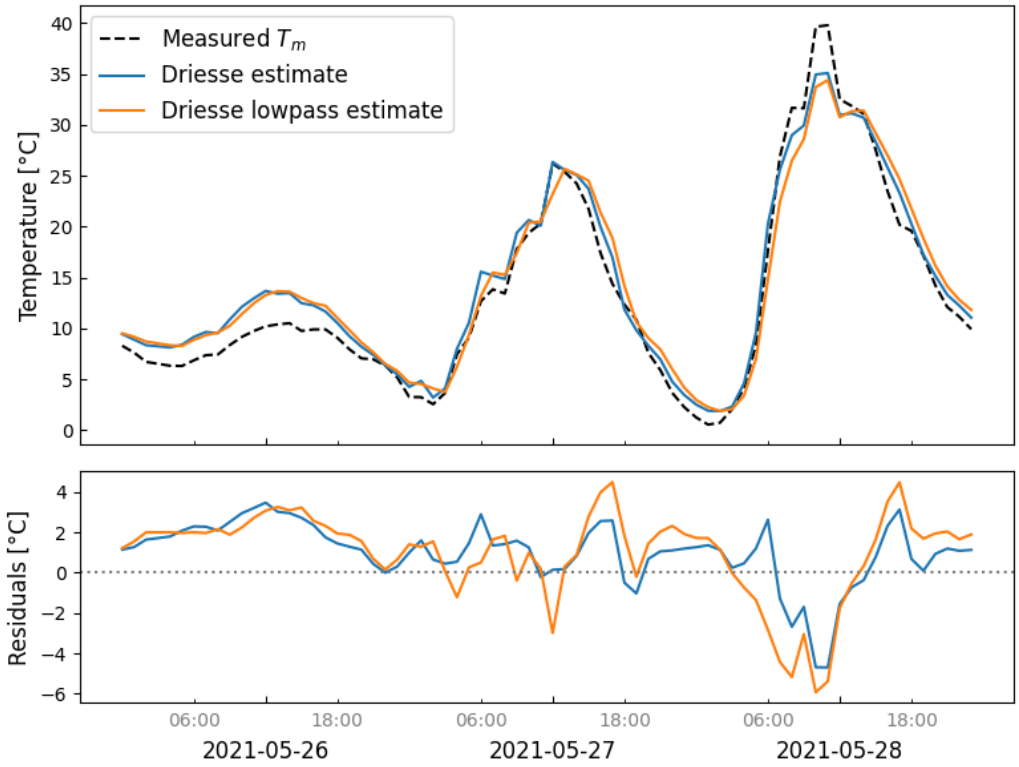

Figure 5.6.1: Comparison of the Driesse model estimates with and without an added lowpass filter, plotted along with the measured module temperature.

and the emissivity $F \cdot \epsilon$ in the Faiman model with a radiative term, is treated as an empirical factor Fe. In the parameter tuning performed for the Faiman model with a radiative term, presented in Section 5.5.2, the view factor was determined from the array tilt as shown in Eq. 2.20, and the default value for the emissivity was used.

5.6.1 Tuning Faiman rad with empirical emissivity

Table 5.6.1 shows the resulting model parameters for the Faiman model with a radiative term, where $F \cdot \epsilon$ is treated as an empirical parameter Fe, tuned for all data and tuned for only daytime data (Irradiance > 5 W/m^2).

Figure 5.6.2 shows the different tuned parameter sets for the Faiman model with a radiative term and an empirical factor Fe, tuned for all data and daytime data only. As for the Faiman model with a radiative term, we see a big difference between the parameters tuned for all data and only daytime data. We again see that by tuning for only daytime data, we get a shift towards higher u_0- and lower u_1-values. As for the Faiman model with a radiative term, we again see that the module-specific parameters for all Kjeller modules are clustered together, while the parameters for the two Gålå modules are spread out widely. Again, there is no clear connection between the parameters for the bifacial modules. In the parameter plots of all three models, we have seen that the parameters for the Bifacial PERC C module generally stand out from the other parameter sets, indicating some difference in temperature behavior. Compared to the other modules, its temperature seems to be less dependent on wind.

Table 5.6.1: Resulting model parameters for the Faiman model with a radiative term from the parameter tuning using all data and daytime-only data (Irradiance > 5 W/m^2). Here, the Fe is treated as an empirical parameter Fe, and tuned. The units are $W/m^2\,℃$ for U_0, and $W/m^2\,℃\,(m/s)$ for U_1, while Fe is dimensionless.

Data set	All data			Daytime only		
	U_0	U_1	Fe	U_0	U_1	Fe
Kjeller	22.161	9.325	1.000	26.245	7.752	1.000
Gålå	28.589	6.336	0.745	29.714	6.301	0.578
Combined	25.340	7.518	1.000	27.536	6.705	1.000
Bifacial	25.460	7.183	0.891	27.607	6.958	0.630
Mono PERC A	20.588	9.553	1.000	28.585	6.494	1.000
Mono PERC B	20.000	11.572	1.000	29.721	7.763	1.000
Mono IBC	24.812	9.231	1.000	27.301	8.264	1.000
Mono HIT	21.055	10.929	1.000	26.082	8.919	1.000
Bifacial PERC A	21.924	9.334	1.000	24.379	8.521	0.941
Bifacial PERC B	22.724	7.517	0.668	24.465	7.456	0.381
Bifacial PERC C	35.211	4.968	0.668	36.186	4.892	0.552
Mono PERC C	23.235	7.450	0.806	24.344	7.481	0.603

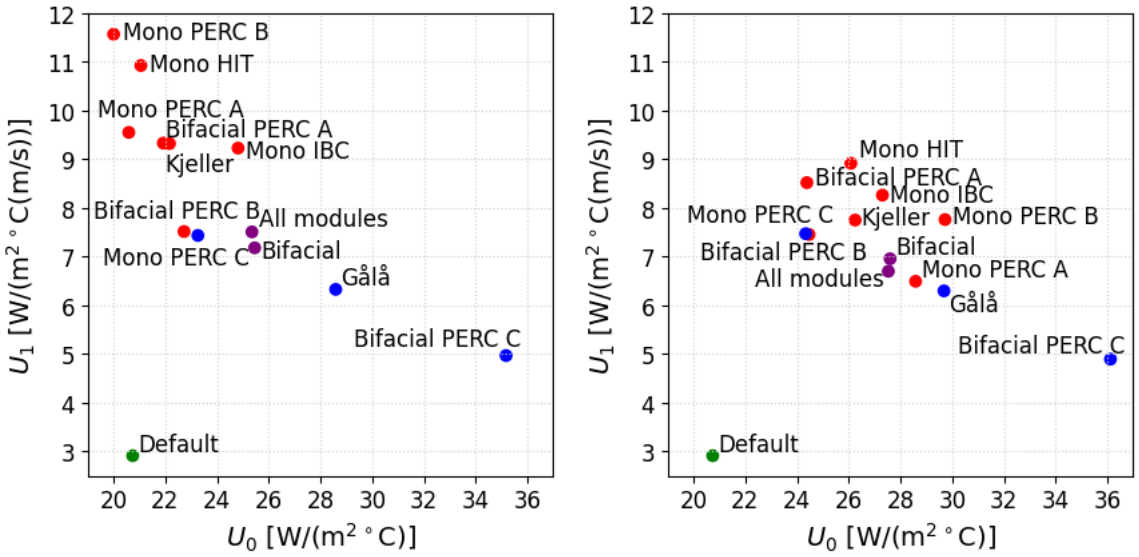

(a) Tuned for all data

(b) Tuned for daytime data

Figure 5.6.2: Tuned parameters for the Faiman model with a radiative term and empirical factor Fe, for all data and only daytime data. The model is tuned for each module individually, all Kjeller modules, all Gålå modules, all bifacial modules, and all modules combined.

5.7 Tuning evaluation for each model

To be able to see the effect of the choice of data for tuning, an evaluation of RMSE and MBE for each model and each module was performed. For each module, the default,

climate-specific (both test sites), site-specific for each test site, bifacial-specific, and module-specific parameters were tested.

5.7.1 Tuned Faiman model

Figure 5.7.1 shows the RMSE and MBE of each set of tuned parameters for the Faiman model for all modules at the Kjeller and Gålå PV test sites. A clear result for the tuning of the Faiman model is that all tuned parameters give a clear improvement in the model performance compared to the default parameters, as the MBE has been improved for all parameters, and the RMSE is improved for most parameters. For all modules, the module-specific parameters give the lowest RMSE, which seems reasonable as they have been tuned for the module by minimizing the MSE. All modules in the Kjeller test sites, except Bifacial PERC B, have the poorest performance for the Gålå site-specific and the bifacial-specific parameters, both in terms of RMSE and MBE. However, for the Bifacial PERC B module, also in the Kjeller test site, the Gålå- and Bifacial-specific parameters perform better than the general climate-specific and the Kjeller site-specific parameters. Seeing a better performance for the site-specific parameters for Gålå than Kjeller is surprising for a module installed at Kjeller, but can be explained by studying Figure 5.5.1. Here we see that the module-specific parameters for the Bifacial PERC B module lie close to the Mono PERC C parameters, and close to the bifacial-specific parameters. This is interesting, as the Bifacial PERC B and Mono PERC C modules are in different locations, and one is bifacial. For the two Gålå modules, there is no clear tendency in the performances. For the Bifacial PERC C module, the site-specific parameters from Kjeller give the lowest MBE, while the Gålå-specific and bifacial parameters have the highest bias, while for the Mono PERC C module, we see the opposite. Overall, the module-specific parameters seem to give the best performance, though the differences are often marginal, and it does not seem to be a clear advantage of site-specific or bifacial-specific parameters for the Faiman model.

5.7.2 Tuned Faiman model with a radiative term

Figure 5.7.2 shows the RMSE and MBE of each set of tuned parameters for the Faiman model with a radiative term for all modules at the PV test sites at Kjeller and Gålå. We see for all modules that there is a clear improvement in both RMSE and MBE for all tuned parameters compared to the default parameters. We again see that the module-specific parameters give the lowest RMSE for all modules, but variation in which parameters give the lowest MBE. Mono PERC A, Mono PERC B, Mono IBC, Mono HIT, Bifacial PERC B, and Mono PERC C have the lowest MBE for the module-specific parameters, and we can conclude that these parameters perform the best for these modules. However, the differences from the other parameters are often small, and any choice of a tuned parameter set would be a significant improvement from the default parameters. For the Bifacial PERC A and Bifacial PERC C modules, the lowest MBE is seen for their respective site-specific parameters. However, for Bifacial PERC B, its site-specific parameter gives the highest MBE, so there is not necessarily a trend. All in all, we again see that generally the module-specific parameters are performing marginally better, but that using a set of climate-specific or site-specific parameters still gives a substantial improvement to the models.

5.7.3 Tuned Faiman model with a radiative term and empirical Fe

Figure 5.7.3 shows the RMSE and MBE of each set of tuned parameters for the Faiman model with a radiative term and an empirical parameter Fe for all modules at the PV test sites at Kjeller and Gålå. We again see a considerable improvement for all tuned parameters compared to the default parameters in both RMSE and MBE. The models with the module-specific parameters again have the lowest RMSE for all modules, as well as the lowest MBE for Mono PERC B, Mono IBC, Mono HIT, Bifacial PERC B, and Bifacial PERC C. While Mono PERC A and Bifacial PERC A have the lowest MBE for their site-specific parameters, and Bifacial PERC C has the lowest MBE for the bifacial-specific parameters. We again see much of the same tendencies as before, that even though the best performance is seen for the module-specific parameters, we can still get a sufficiently accurate model using climate- or site-specific parameters. Site-specific parameters generally perform well for their respective modules, but for Bifacial PERC B, we see that the Gålå parameters have a better performance than the Kjeller parameters, indicating that site-specific parameters might not be necessary.

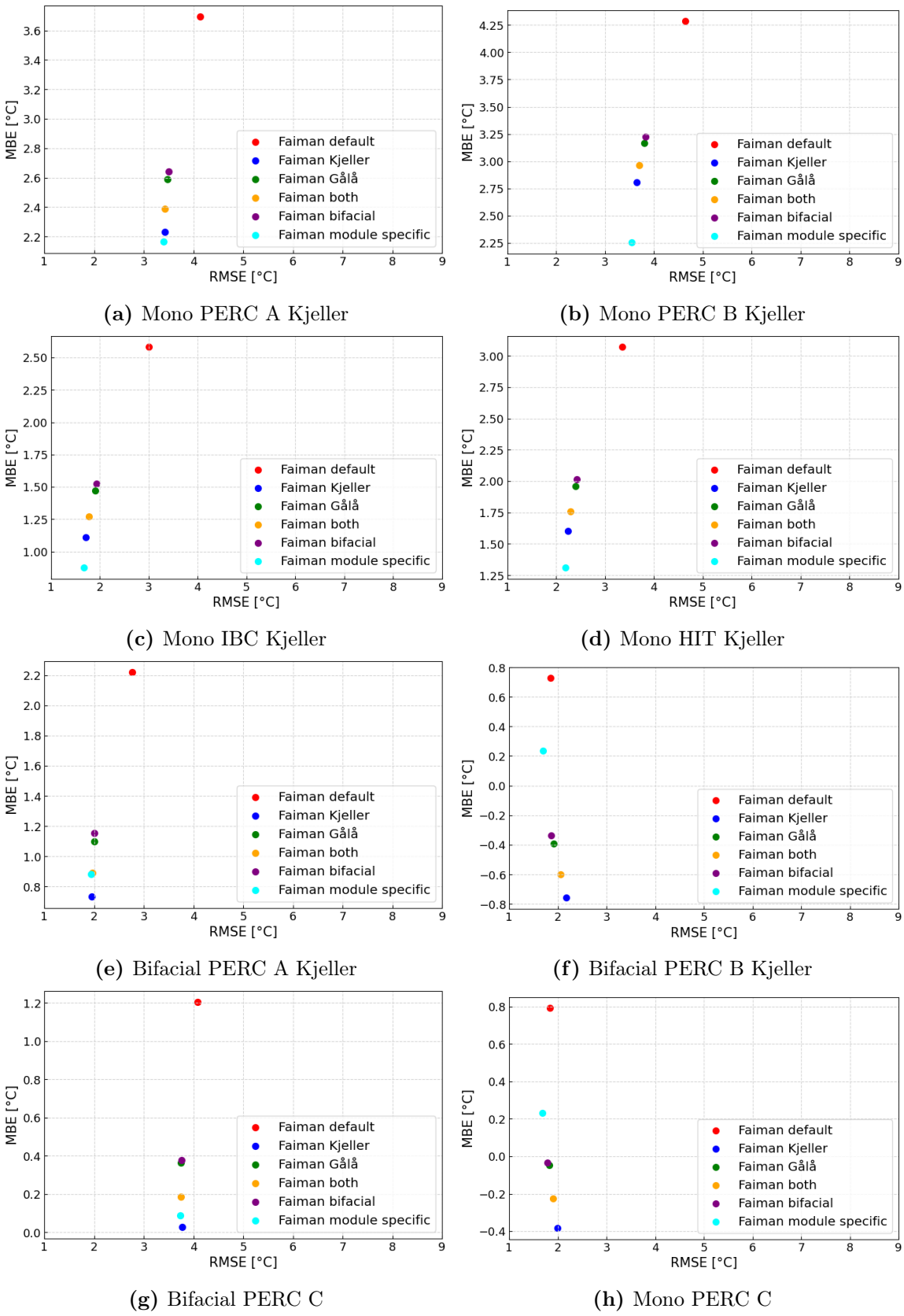

(a) Mono PERC A Kjeller

(b) Mono PERC B Kjeller

(c) Mono IBC Kjeller

(d) Mono HIT Kjeller

(e) Bifacial PERC A Kjeller

(f) Bifacial PERC B Kjeller

(g) Bifacial PERC C

(h) Mono PERC C

Figure 5.7.1: The RMSE and MBE of the Faiman model with different model parameters for all modules at the PV test sites at Kjeller and Gålå. The model parameters tested are tuned for both test sites, only the Kjeller data, only the Gålå data, only bifacial modules, and specifically for the module. The tuning is performed with and tested for daytime data.

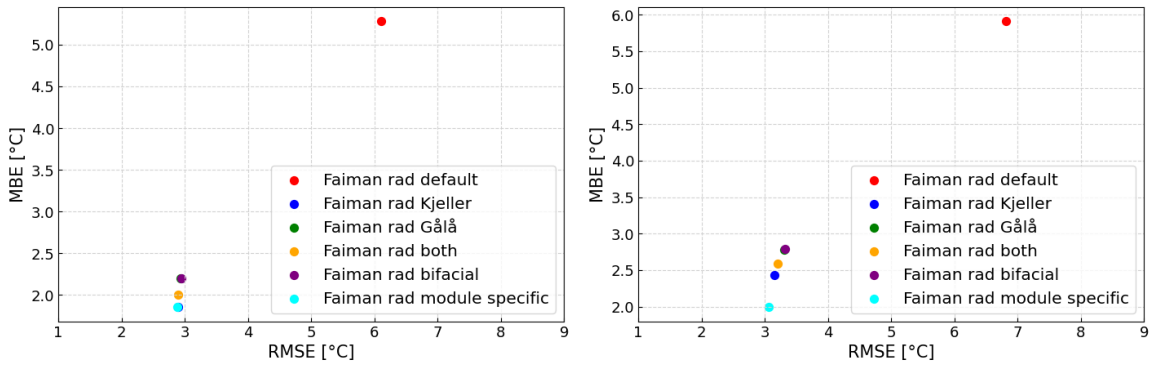

(a) Mono PERC A Kjeller

(b) Mono PERC B Kjeller

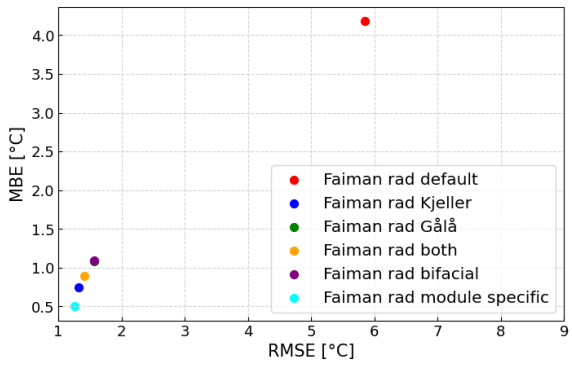

(c) Mono IBC Kjeller

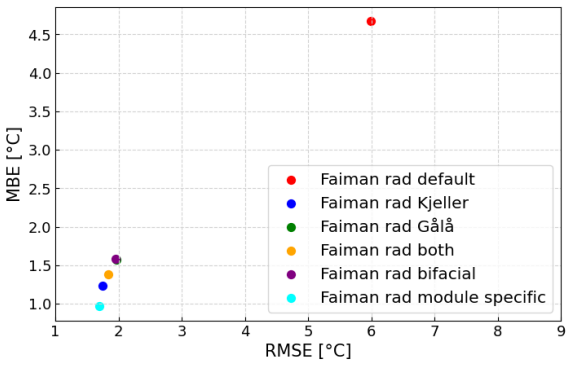

(d) Mono HIT Kjeller

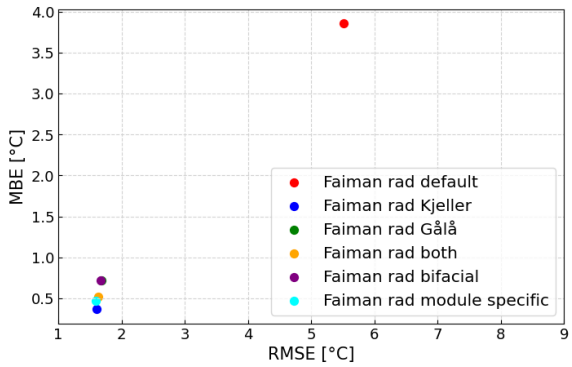

(e) Bifacial PERC A Kjeller

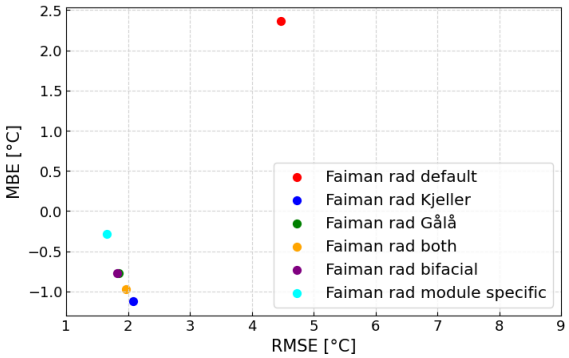

(f) Bifacial PERC B Kjeller

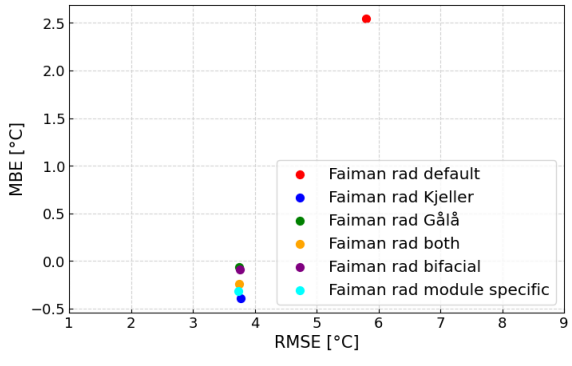

(g) Bifacial PERC C

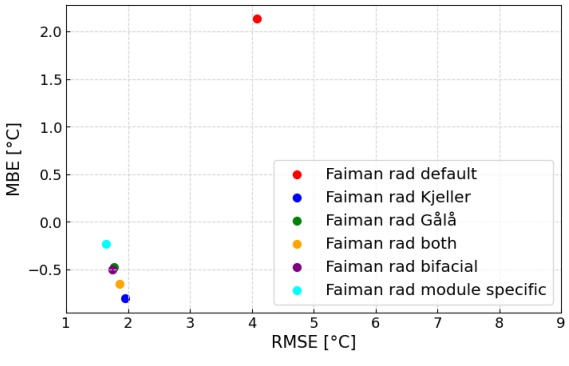

(h) Mono PERC C

Figure 5.7.2: The RMSE and MBE of the Faiman model with a radiative term with different model parameters for all modules at the PV test sites at Kjeller and Gålå. The model parameters tested are tuned for both test sites, only the Kjeller data, only the Gålå data, only bifacial modules, and specifically for the module. The tuning is performed with and tested for daytime data.

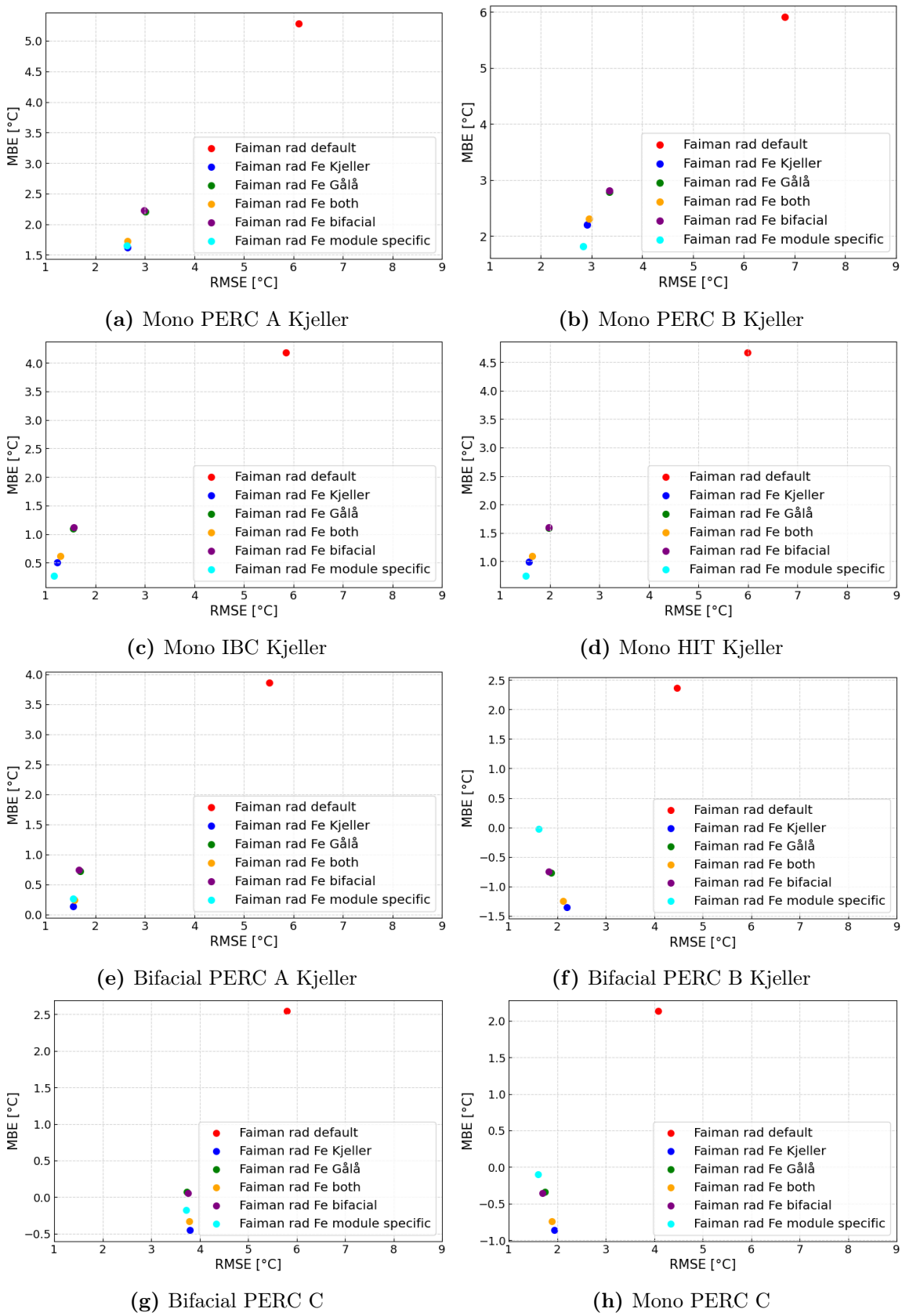

(a) Mono PERC A Kjeller

(b) Mono PERC B Kjeller

(c) Mono IBC Kjeller

(d) Mono HIT Kjeller

(e) Bifacial PERC A Kjeller

(f) Bifacial PERC B Kjeller

(g) Bifacial PERC C

(h) Mono PERC C

Figure 5.7.3: The RMSE and MBE of the Faiman model with a radiative term and empirical $F\epsilon$ with different model parameters for all modules at the PV test sites at Kjeller and Gålå. The model parameters tested are tuned for both test sites, only Kjeller data, only Gålå data, only bifacial modules, and specifically for the module. The tuning is performed with and tested for daytime data.

5.8 Model comparisons

For completeness, comparison plots with all model performances are shown in Appendix B.2. As these contain a lot of information, making them hard to read, the main findings will be summarized in this section.

5.8.1 Comparison between the different models in their tuned version

To compare the three models that we have tuned, i.e., the Faiman model, the Faiman model with a radiative term, and the Faiman model with a radiative term and an empirical $F\epsilon$, we want to study them in their parameter-tuned form. Figure 5.8.1 shows all the models where each color has all tuned versions of each model, meaning the climate-specific, site-specific for each test site, bifacial-specific, and module-specific parameters. This can give an indication of which model generally performs the best. The comparison is done for models tuned and tested for daytime data, but an equivalent figure with models tuned and tested for all data is included in Appendix B.3. We see that all tuned models form a cluster with lower RMSE and MBE than the default models, and even the Fuentes model, which was the model found to perform the best in Sections 4.5 and 5.3. There are, however, differences within this cluster, the most evident being that the Faiman model tends to have higher MBE and RMSE. The two Faiman models with a radiative term lie closer together for most modules, but the model with an empirical Fe often performs slightly better. We do, however, see that for most modules, any choice of tuned model will be a significant improvement from the default Faiman model, the default Faiman model with a radiative term, and the Fuentes model. The corresponding evaluation for models tuned with and tested for all data shows similar results, but a clearer tendency that the Faiman model with a radiative term and an empirical factor Fe performs the best. As this has an additional tuning factor, this is not surprising. When evaluating the default models in Sections 4.5 and 5.3 we also saw that the Faiman model with a radiative term had a poor performance in comparison to the Faiman model, which was surprising due to the radiative term adding complexity to improve the Faiman model. Looking at the parameter tuning in Section 5.5, we saw that the tuned parameters for the Faiman model with a radiative term were far away from the default parameters, leaving us to believe that the tuning could give a significant improvement. This could also explain the poor performance for the default parameters despite the added complexity. By comparing the tuned models, we see that the radiative term does, in fact, improve the performance of the model. Another observation is that the Fuentes model still performs well for the models tuned and tested on all data, which can be found in Appendix B.3, often outcompeting the tuned versions of the Faiman model, but for the models tuned and tested for daytime data, we see that the tuned models generally perform better than the Fuentes model for most modules.

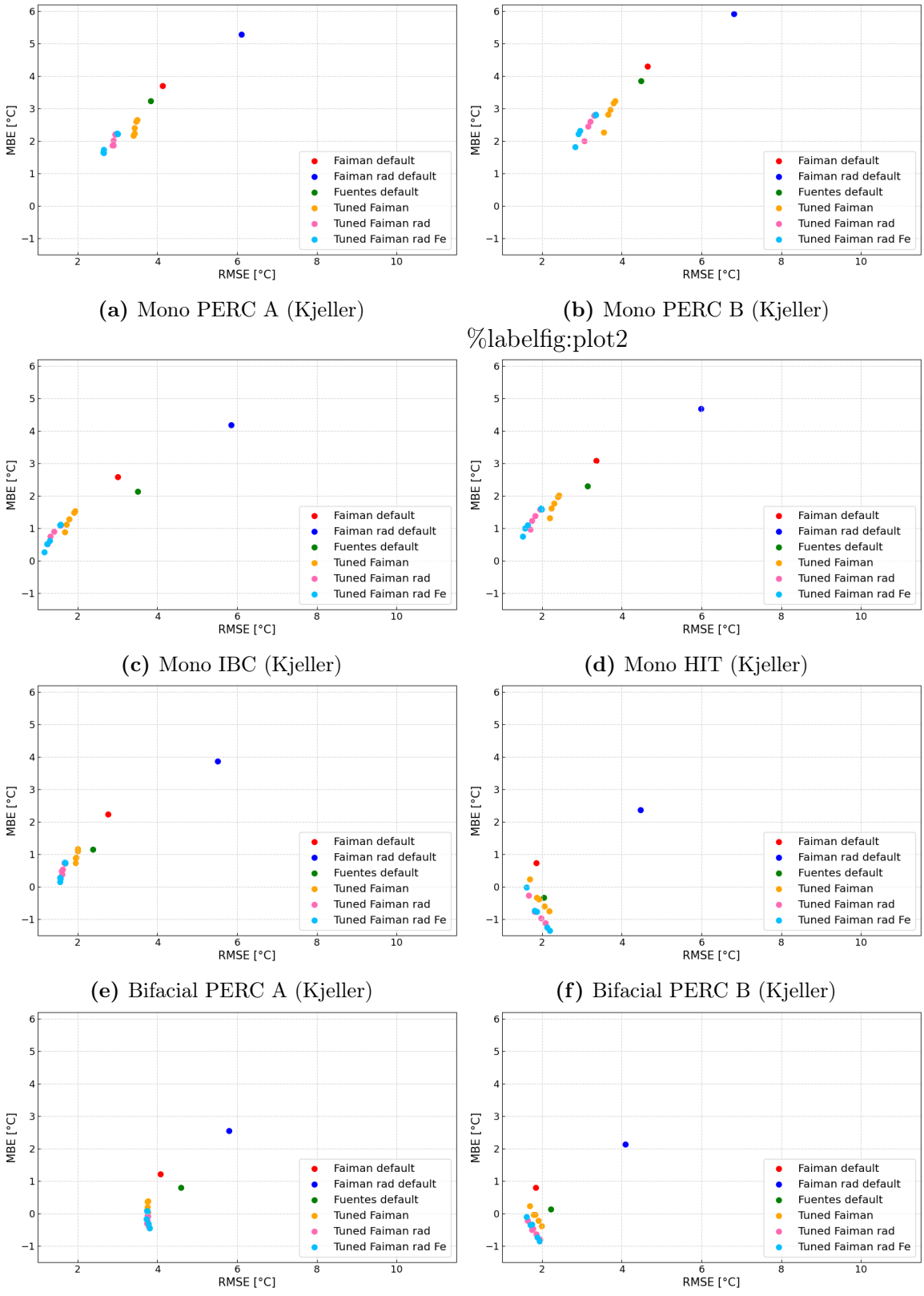

(a) Mono PERC A (Kjeller)

(b) Mono PERC B (Kjeller)

%labelfig:plot2

(c) Mono IBC (Kjeller)

(d) Mono HIT (Kjeller)

(e) Bifacial PERC A (Kjeller)

(f) Bifacial PERC B (Kjeller)

(g) Bifacial PERC C (Gålå)

(h) Mono PERC C (Gålå)

Figure 5.8.1: All tuned models are plotted together, where the colors indicate which model they are tuned versions of. The performances displayed here are for models tuned and tested for daytime data. The Faiman model with a radiative term is denoted by Faiman rad, and the Faiman model with a radiative term and an empirical parameter Fe is denoted by Faiman rad Fe. Note that the different markers for the tuned models correspond to different parameters given in Tables 5.5.1, 5.5.2, and 5.6.1.

5.9 Tuning using all data compared to only daytime data

As we have performed all tuning for both all data and data where the nightly values have been removed, we want to study the difference in these models. As temperature models are mostly used for production estimation, their performance at night is often irrelevant. However, in some cases, temperature models can be used for degradation purposes, where the temperature at night is just as important [68]. If a model can perform well both during the night and day, this would be a good choice, as it can be used for both purposes. However, if including the nighttime values adds error to the daytime estimations, one might need to prioritize the two use cases differently.

Figure 5.9.1 compares the Faiman model with a radiative term and an empirical parameter Fe tuned for daytime data only and tuned for all data. The default Faiman model with a radiative term is plotted for comparison. We see that the two tuned models lie closely together, and only differ in some periods. One would expect to see a difference at night, as the model tuned only for daytime data does not include these values in the tuning. However, though the model tuned for all data performs slightly better at night, we see that the difference is minimal. We see similar results during the day, and we even see on 2021-05-27 that the model tuned for all data performs better midday than the model tuned for only daytime data. On the high-irradiance day, 2021-05-28, we see that the daytime model performs slightly better. Yet, it is evident that both models are a significant improvement from the default, and these small differences might not be worth focusing on. A similar analysis has been performed for all modules at both locations, and it was seen that for all modules, the two tuned models performed quite similarly with some small differences. For the Faiman model, the two models are indistinguishable when plotted, and for the Faiman model with a radiative term, there are some small differences.

To determine the effect of tuning for only daytime data, we want to quantify this result for the entire dataset instead of over a few days. Figure 5.9.2 shows the RMSE and MBE for each model tuned for all data and for only daytime data, tested for the Mono PERC B module. The models are all tuned for both PV test sites combined, and the testing is done for only daytime data. Though seemingly insignificant, for the Faiman model, we see a slight decrease in performance for the model tuned for daytime data only. We also see that for the models tuned for only daytime data, we get a slight increase in the model performance for the two Faiman models with a radiative term. We see a clear decrease in both RMSE and MBE when tuned for only daytime data. This decrease is, however, smaller than 0.1 °C in both RMSE and MBE. This is smaller than a typical measurement uncertainty we saw in Section 4.3, meaning that the difference could be deemed negligible. We see the same tendencies as for Mono PERC B for several of the other modules, while a few even display an opposite effect. All in all, there does not seem to be a significant difference in the daytime performance whether you tune the models for only daytime data or all the data. This means that the daytime estimates are not significantly harmed by including nighttime data in the tuning of the models.

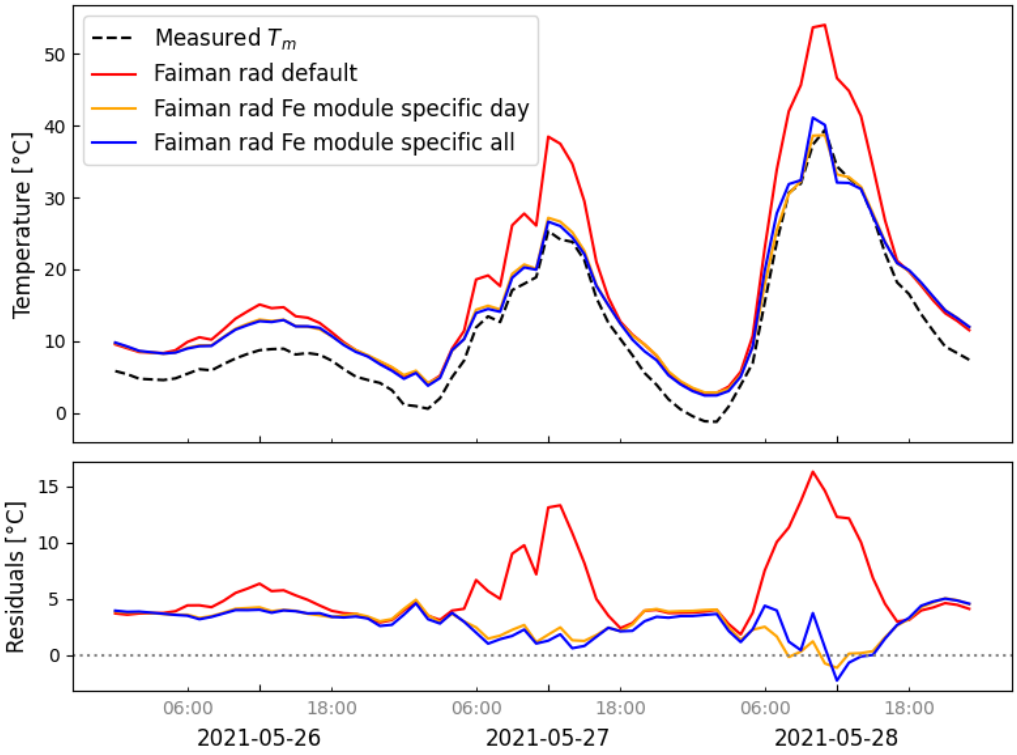

Figure 5.9.1: Temperature estimates from the Faiman model with a radiative term and an empirical parameter Fe with module-specific parameters, tuned for both all data and daytime data only. The measured temperature and the model estimate for the default parameters are also included for comparison. The measurements and estimates are done for the Mono PERC B module.

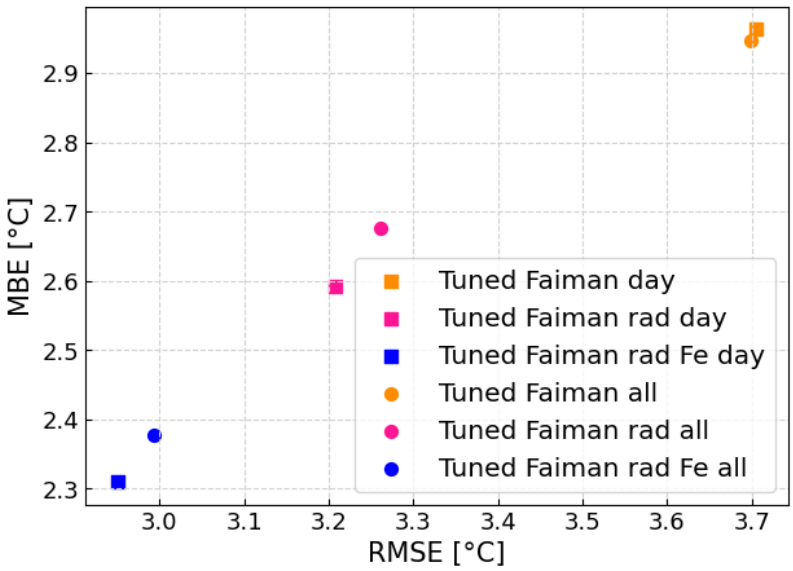

Figure 5.9.2: Comparison of performance of each model tuned for daytime data and all data, when tested on daytime data. All models are tuned for data from both PV test sites. Each model is indicated by a color, where the translucent point is the performance for the model tuned for all data, while the opaque point is for the model tuned for only daytime data. The measurements and estimates are done for the Mono PERC B module.

5.10 Incorporating backside irradiance for bifacial modules

In the model evaluation and development, the bifacial modules have been treated equally to the monofacial modules, despite being designed to absorb more of the backside irradiance. This has been done, as measurements of backside irradiance are not always available, especially in a planning phase. However, as both PV test sites used in this thesis have backside irradiance measurements, a small analysis has been performed on how including the rear-side irradiance in the irradiance term for the bifacial modules will affect the model performance. Each module has a bifaciality factor β, describing the ratio between the rear-side and front-side efficiency [18]. Looking at the PVsyst model in Eq. 2.30, shown to be equal to the Faiman model, we see that the G_{poa} is multiplied with $\alpha(1-\eta_m)$, where α is the absorption and η_m is the module efficiency. This, in principle, leaves us with the part of the irradiance left as heat. When incorporating the backside irradiance, the bifaciality was therefore incorporated as follows

$$G_{eff} = G_{poa,front} + G_{poa,rear}\frac{1-\eta_m\beta}{1-\eta_m}, \tag{5.1}$$

derived by replacing $\alpha \cdot (1-\eta_m) \cdot G_{poa}$ in the original model with $\alpha \cdot (1-\eta_m) \cdot G_{poa,front} + \alpha \cdot (1-\eta_m \cdot \beta) \cdot G_{poa,rear}$, as $\eta_m\beta$ is the rear-side efficiency. As the Faiman and PVsyst models were proven equal in Section 2.4, the factor $\alpha \cdot (1-\eta_m)$ is, in principle, embedded in the empirical parameters for the Faiman model. We can then use G_{eff} as in Eq. 5.1 as the irradiance when tuning and testing for the bifacial modules.

The bifaciality factor β is 65% for Bifacial PERC A [69], and 57% for Bifacial PERC B [45]. The bifaciality factor of the Bifacial PERC C module is not specified in the datasheet, and a typical bifaciality factor for PERC cells of 70% was used [18]. The module efficiency was set to 15% for all modules, as proposed for the PVsyst model [22].

All parameters were tuned again with this effective irradiance, giving new parameter sets which can be found in Appendix B.4. To see the effect of including the rear-side irradiance, we want to again evaluate the models. Figure 5.10.1 shows the model performances for the models tuned with backside irradiance evaluated for all modules marked as triangles. The corresponding models tuned without incorporating the backside irradiance are marked with circles. Default models and tuned models with site-specific parameter sets were not included to avoid clutter. For all the monofacial modules at Kjeller, we see a tendency towards lower biases and slightly lower RMSE for the models where backside irradiance is incorporated for the bifacial modules for the tuning. The differences are, however, often small. The same tendency is seen for the Bifacial PERC B module, while for the Bifacial PERC A module, all models display the opposite. For the Bifacial PERC C module at Gålå, the models incorporating the backside irradiance all have a slightly lower RMSE, but an MBE bigger in magnitude. For the Mono PERC C module, also at Gålå, we see that all models incorporating the backside irradiance have a higher RMSE and an MBE bigger in magnitude than the models tuned without backside irradiance. This shows that incorporating the backside irradiance for the bifacial modules during tuning and testing has varying results for the different modules. All in all, there is no clear ten-

dency across all modules, and it is thus unclear whether incorporating the backside irradiance for bifacial modules will improve the general performance of the model. This should, however, be investigated further, preferably with a larger dataset with more bifacial modules.

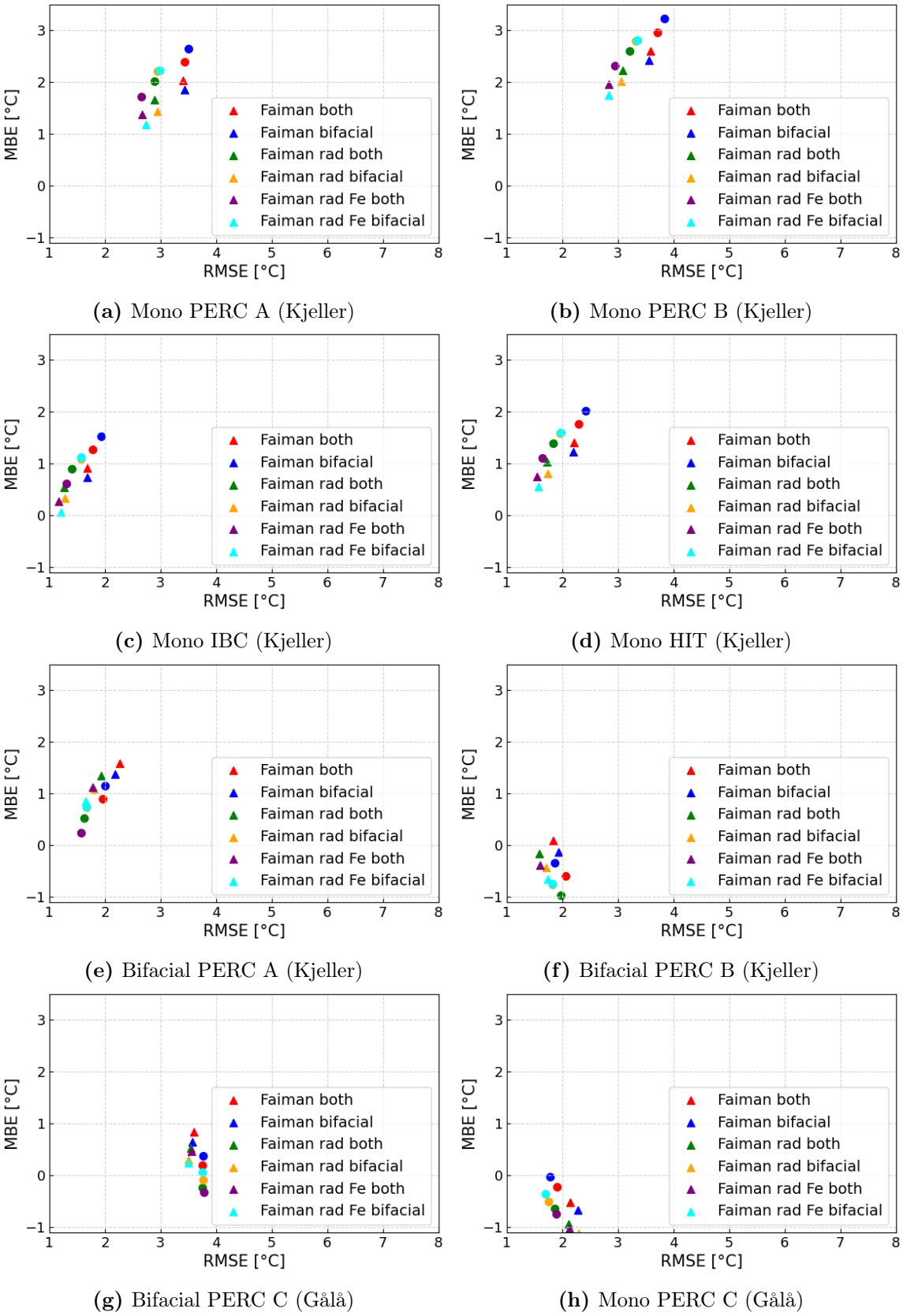

(a) Mono PERC A (Kjeller)

(b) Mono PERC B (Kjeller)

(c) Mono IBC (Kjeller)

(d) Mono HIT (Kjeller)

(e) Bifacial PERC A (Kjeller)

(f) Bifacial PERC B (Kjeller)

(g) Bifacial PERC C (Gålå)

(h) Mono PERC C (Gålå)

Figure 5.10.1: Comparison of model performances for models tuned when backside irradiance is included for the bifacial modules as triangles, and the corresponding models tuned and tested without backside irradiance as circles. The models are tuned and tested for daytime data. The parameter sets plotted for each model are tuned for both PV test sites and bifacial modules only. The models used are the Faiman model, the Faiman model with a radiative term (Faiman rad), and the Faiman model with a radiative term and an empirical term Fe (Faiman rad Fe).

5.11 Comparison of climate-specific models

As site- or module-specific parameters are generally hard to obtain, and are only possible to develop after a PV system has been in operation for some time, a climate-specific parameter set will often be the only option. We therefore want to study which of the models we have tuned performs best with its respective climate-specific parameter set. By climate-specific parameter set, we mean the parameters tuned for both PV test sites. Figure 5.11.1 shows the average RMSE and MBE for each of the three climate-specific models for all modules. The average MBE has been calculated with the absolute value of the MBE for each module, as the bias can be both positive and negative, and we are mostly interested in its magnitude. Both of the Faiman models with a radiative term are significantly better than the Faiman model, which has an average RMSE of 2.89 °C and an average |MBE| of 1.85 °C. The Faiman model with a radiative term and an empirical parameter Fe has a slightly better performance than the Faiman model with a radiative term. The Faiman model with a radiative term and an empirical parameter Fe has an average RMSE of 2.29 °C and an average |MBE| of 1.38 °C, while the Faiman model with a radiative term and an empirical parameter Fe has an average RMSE of 2.09 °C and an average |MBE| of 1.23 °C. Though small differences, we see that the Faiman model with a radiative term and an empirical parameter Fe performs the best when averaged over all modules.

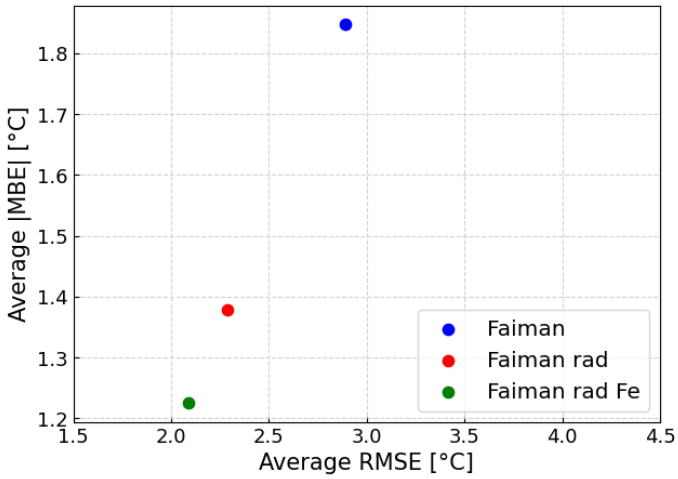

Figure 5.11.1: Average performance over all modules for the climate-specific parameters for the following models: the Faiman model, the Faiman model with a radiative term, and the Faiman model with a radiative term and an empirical parameter Fe. The models are tuned and tested for all data.

Although we observe a better performance for the two Faiman models with a radiative term, it is essential to note that this improvement of up to 0.8 °C in RMSE and 0.63 °C in |MBE|, comes at the cost of a more complex model. The choice of model should therefore be based on the need for accuracy and the available data. For systems where measurements of the downwelling infrared radiation from the sky are not available, the Faiman model with climate-specific parameters is still a good option. Another factor to consider is that for the two Faiman models with a radiative term, we have the best performance for the model treating Fe as an

empirical parameter Fe. F is a view factor, which depends on the tilt angle of the module. In this data set we have modules with tilt angles of 45° at Kjeller and 30° at Gålå, and it is therefore surprising that the model with an empirical Fe performs best when tuned for both test sites equally. This would be interesting to study for more modules with different tilt angles, to see if treating $Fe\epsilon$ as an empirical parameter is always reasonable. The climate-specific model has $Fe = 1.0$, which would correspond to having a view factor of 1 and an emissivity of 1 in the original model. A view factor of 1 corresponds to having a horizontal module, and it is therefore interesting that it works for different tilt angles [36].

5.12 Effect on DC power estimation

In this section, we will study the effect that an improved temperature model can have on the DC power estimations. This is done to put the improvements into perspective and see whether the improved accuracy can have a significant effect on energy yield assessments. The `pvwatts_dc` function presented in Section 3.3.3 was used to make the DC power estimates. The DC power was calculated for the estimated temperatures by the models with and without tuned parameters. For comparison, the DC power calculated with the measured module temperature was used as a ground truth. For the three bifacial modules. the backside irradiance multiplied by the module's respective bifaciality factor was added to the POA irradiance for the DC power estimations.

To give an idea of the effect of improving the temperature model, we want to compare the performance of a commonly used model, the Faiman model with default parameters, with the best-performing models after parameter tuning. Generally, the best performance is seen for the Faiman model with a radiative term, where Fe is tuned. The model with parameters tuned for the specific modules often performs best, and is therefore used along with the Faiman model with default parameters in this DC power estimation.

Figure 5.12.1 shows a comparison of the estimated DC power for the Mono PERC A module using the measured module temperature and the temperature estimated by the default Faiman model for a selected day. Here we see that although the error in the temperature estimation gives an error in the DC power estimation, this is seemingly small. However, at most, we see an error of approximately 7 W at 09:00, which for a DC power of 320 W, is an error of 2.2 %.

Figure 5.12.2 shows all hourly values for the DC power with the measured temperature and the estimated temperature. With a perfect temperature model, all points would lie on the diagonal line, as the two values would be equal. We see that for the default Faiman rad, which is the model shown to perform the worst, the points start deviating for higher DC power values, and we see that the temperature estimation leads to an underestimation of the DC power. However, looking at the corresponding plot for the module-specific tuned temperature model, though we still see deviations, the points are centered along the diagonal line. This shows a clear improvement, as we see that for the default parameters, there is a clear negative bias in the model for the highest DC power values. As the module-specific parameters are rarely a possibility, especially during the planning phase, the same plot is created for the climate-specific parameters, i.e., the parameters tuned for both test sites. We see

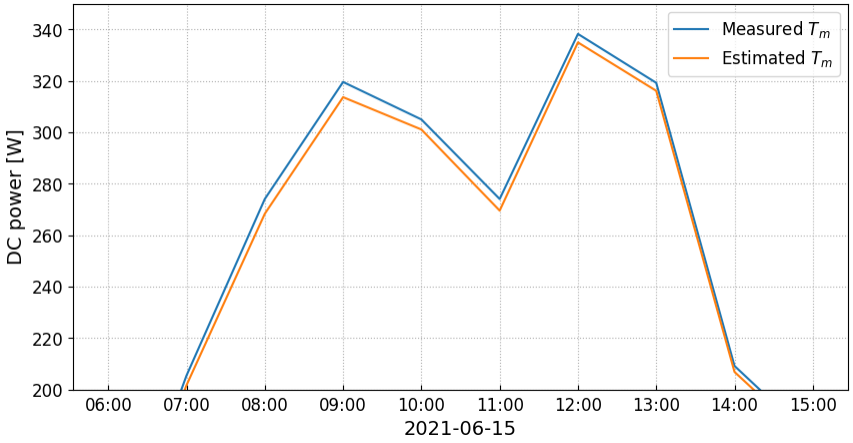

Figure 5.12.1: Comparison of the estimated DC power for the measured temperature and the temperature estimated by the default Faiman model. The module used in the estimations is Mono PERC A.

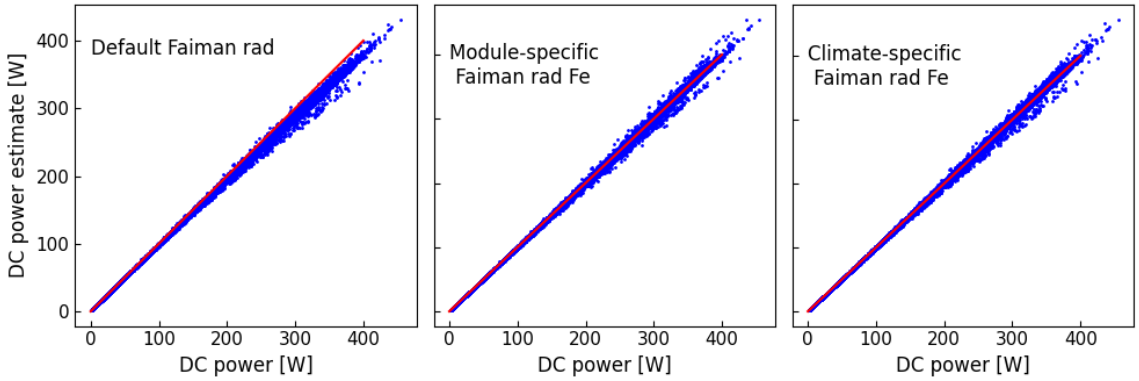

Figure 5.12.2: Estimations made with the measured temperature and the estimated plotted against each other as a scatter plot, for the Faiman model with a radiative term with default values, with module-specific parameters and an empirical factor Fe, and the combined parameters for both test sites with an empirical factor Fe. All modules are included.

that this also gives a clear improvement from the model with the default parameters, as the points are centered around the diagonal line, showing that we have a low bias.

For the Bifacial PERC C module at Gålå, with an installed maximum power of 365 W [51], the yearly error for 2024 when estimating the DC power using the default Faiman model is 22.78 kWh/kWp. The corresponding error for the Faiman model with a radiative term is 68.84 kWh/kWp. However, when using the climate-specific parameters for the Faiman model with a radiative term and an empirical parameter, this error is reduced to 0.22 kWh/kWp. This shows that the yearly error is significantly improved by using a climate-specific temperature model in the DC power estimation.

Figure 5.12.3 shows the yearly error in kWh/kWp as well as the relative error for all modules for the default Faiman model with a radiative term and the module- and climate-specific Faiman model with a radiative term and an empirical parameter Fe. Here, it is clear that parameter tuning reduces the error in the power estimation,

as both of the tuned models have much smaller errors for all modules. For the default Faiman model with a radiative term, we see errors in the range of 2 – 3 % for all modules, while for both of the tuned models, the error never exceeds 0.5 %. We also see that, not surprisingly, the module-specific model generally has a lower error than the climate-specific model, but this difference is small. Considering that the module-specific parameters are essentially the best case for the model, the climate-specific parameters seem to give good results. We also see that using the improved temperature models can improve energy estimations significantly, as an error contribution of 2 – 3 % from the temperature models alone can be reduced to well below 0.5 %.

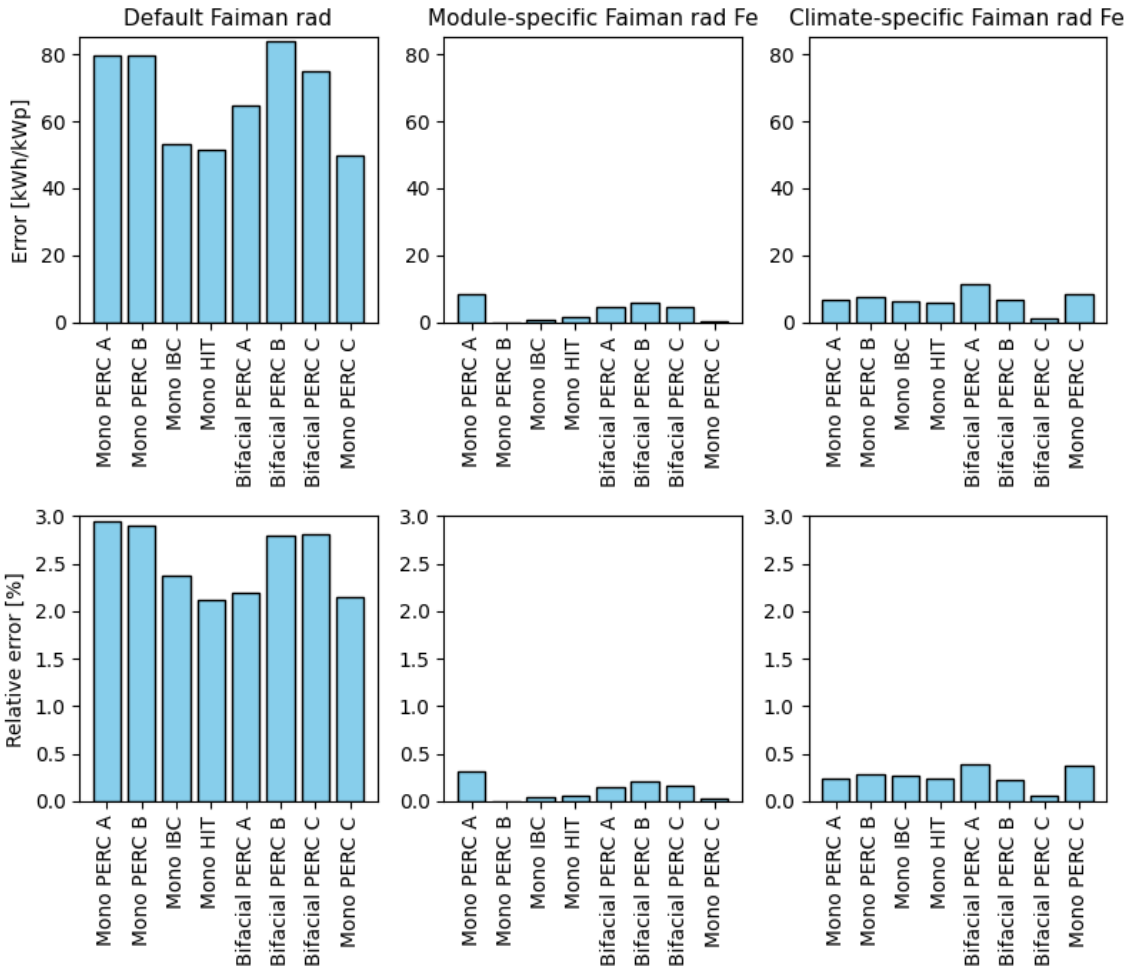

Figure 5.12.3: Yearly error for each module for each model given in kWh/kWp, as well as the relative error. Note that the values for the modules at the Kjeller test site are for the year 2023, while the values for the modules at the Gålå test sites are for 2023.

5.13 Summary and final discussions

In this thesis, we wanted to explore the possibility of improving existing temperature models by parameter tuning. The author's previous work in the project thesis, presented in Chapter 4, showed that existing models performed poorly on the PV test site at IFE, Kjeller. In Section 5.3, the evaluation of existing models was repeated for a PV test site at Gålå, where similar results were found. Though both test sites are in Norway, they are located in different Köppen–Geiger climate zones, as presented in Section 2.6. Kjeller is located in a warm-summer humid continental climate, while Gålå has a subarctic climate. It was therefore interesting to see if it would be necessary with two site-specific parameter sets or if a general model tuned for both of these would perform well enough. For the models we chose to use for parameter tuning, the Faiman model and the Faiman model with a radiative term, the default parameters were tuned in a BWh climate, and a Cfb climate, so it was believed that this could be a source to why the default model estimates had such a large bias. To explore whether a general Nordic model would be possible, we performed all parameter tunings for both sites individually, both sites combined, and each module specifically. In addition, the tunings were performed for only bifacial modules to explore whether an individual bifacial model would be necessary.

In Section 5.8.1 we compared all tuned versions of the three models, the Faiman model, the Faiman model with a radiative term, and the Faiman model with a radiative term and an empirical parameter Fe. Here we could see that the radiative term gives a better performance when the models have been tuned, indicating that the poor performance seen in Sections 4.5 and 5.3 was due to the default parameters. Though it varied between the modules, the Faiman model with a radiative term and an empirical parameter Fe seems to perform the best. It does, however, perform very similarly to the Faiman model with a radiative term, while the Faiman model generally has a slightly higher RMSE and often a higher MBE. We, however, saw that the tuned versions of the Faiman model also were a clear improvement from the default empirical models, and it is therefore a good alternative if one does not have access to reliable measurements of downwelling radiation from the sky, or wants a less complex model.

To evaluate how the choice of data used in the tuning affected the results, we have studied the tuned versions of each model individually. A general trend we saw was that the module-specific parameters often had the best performance, which was an expected result when the parameters are tuned by minimizing the MSE for the specific module. We did, however, find that all tuned parameters gave a significant increase in performance compared to the default parameters. As module-specific parameters is the best fit for a model for the specific module, seeing that the performance of the other tuned parameters is comparable is a good sign for the more general models. The parameters tuned for both PV test sites are generally performing well for all modules, though generally outperformed by the module-specific parameters. As the temperature models are often used in the planning phase of a PV system, data that can be used for site- or module-specific parameters is not generally available, and a set of general Nordic parameters will be the best available option. It is therefore a promising result that we see such a clear improvement in the performance compared to the corresponding models with their default parameters, even for the parameters tuned for both test sites. It is, however, worth mentioning that as the modules we are

evaluating the models on are the same as for the tuning, we do not know for certain that if we tested for an independent PV test site in Nordic conditions that the results would be similar for the general Nordic model. The fact that we do see a significant increase in the performance even when testing the Gålå-specific parameters for the Kjeller test site, and vice versa, is a good sign regarding a general Nordic model. Kjeller and Gålå test sites are in different climate zones, and we have seen from our study of weather parameters that the Gålå site generally has a lower temperature, higher wind speed, and higher relative humidity. Seeing that their parameters could be interchanged while still having a good performance is a positive indicator for a general Nordic model.

As this is only tested for two PV test sites, it would be a good idea to repeat the analysis for more test sites in Nordic conditions, so one could evaluate a model tuned for several test sites on an independent test site. Regarding the module-specific parameters, we now tune and test for single modules at one location, and we therefore do not know if these parameters could be suitable for the same module at another location. To further test this, it would be interesting to gather data from test sites at different locations with the same modules to see if the module alone determines the parameters, or if the location is just as important. In our analysis, we saw that the location-specific parameters had varying levels of success. For some modules, we even saw that the location-specific parameters from the opposite PV test site performed better than the parameters of their respective test site. To better be able to analyse whether the location has a big effect on the best-fitting parameters, an analysis like the one in Section 5.5 performed for more test sites with more modules in each would be beneficial. As the Gålå test site only has two different modules, it is hard to determine whether their parameters lying far apart indicate a low dependency on location or if it is simply a random result for these two modules.

As both PV test sites have bifacial modules, we wanted to explore whether these had such different temperature behavior that we would need an individual set of parameters for these modules. To explore this, a set of parameters for each model was tuned for the bifacial modules only. In Section 5.5, we studied the different parameter sets and found that the module-specific parameters for the three bifacial modules were spread out widely among the other modules. No clear trend was seen for the three modules from studying the parameter plots for each model. To explore this further, the set of parameters tuned for bifacial modules only was also brought into the tuning evaluation in Section 5.7. Here, we saw that the parameters tuned for bifacial modules only generally performed quite similarly to other parameters, and for some modules, even worse than the general model for both PV test sites. All in all, there was no clear result indicating that it was beneficial to have a specific set of parameters for bifacial modules.

All parameter tuning was performed for all data and data where nightly values (Irradiance < 5 W/m^2) had been removed. This was done to study whether tuning specifically for daytime data would improve the model performances significantly during the day. As the temperature models in most cases are used in energy yield estimations, the performance during the day is usually the most important. However, as the nightly temperature estimations can be relevant for uses like degradation studies, the performance at night is not necessarily irrelevant [68]. We therefore wanted to study whether including the nightly values when tuning the parameters would harm the performance of the model during the daytime. In Section 5.9, we saw

that the performance during the daytime was improved slightly by removing nightly values during the parameter tuning. This was, however, an improvement of less than 0.1 °C in both RMSE and MBE, which is within the uncertainty of the temperature measurements. In conclusion, the choice of removing or keeping the nightly values does not have a significant effect on the daytime performance.

As the temperature estimation models are often used for estimation of production, the effect of an improved temperature model on DC power estimation was studied. It was shown that there was a significant difference in performance between the worst- and best-performing temperature models; the default Faiman model with a radiative term and the module-specific Faiman model with a radiative term with an empirical factor Fe. We saw that for a high DC power, the default model had a clear tendency to underestimate the production, while the tuned model generally performed well. It was shown that, though generally small, the error in the high-production times was considerable, and that improving the temperature model had an impact on the DC power estimations.

All in all, we have seen that by performing a simple parameter tuning of the existing empirical models, we can improve their performance greatly. The choice of model, which data to include in the tuning, and whether to include nighttime values or not, should be made based on the need for accuracy for the use, the focus area in the use, and the available data and resources. As we have seen that the parameters tuned for both test sites and the parameters tuned for the opposite test site still improve the performance of each model significantly, the idea of a general Nordic model seems reasonable. From studying the model performances for the two PV test sites included in this thesis, we would propose using the Faiman model with a radiative term and an empirical parameter Fe, with the following parameters: $U_0 = 27.536$ W/(m^2 °C), $U_1 = 6.705$ W/(m^2 °C(m/s)), and $Fe = 1.000$ for daytime data or $U_0 = 25.340$ W/(m^2 °C), $U_1 = 7.518$ W/(m^2 °C(m/s)), and $Fe = 1.000$ for all data. However, for systems where measurements of the downwelling infrared radiation from the sky are not available or if one wants a less complex model, a good alternative is to use the Faiman model with the following climate-specific parameters: $U_0 = 33.236$ W/(m^2 °C) and $U_1 = 7.120$ W/(m^2 °C(m/s)) for daytime data or $U_0 = 33.385$ W/(m^2 °C) and $U_1 = 7.111$ W/(m^2 °C(m/s)) for all data. For these to be robust models suitable for all Nordic climates, more PV test sites should be included in the tuning, preferably spread around in different climate zones in the Nordic countries. However, these parameters seem promising for the two test sites studied in this thesis.

CHAPTER

SIX

CONCLUSION

In this thesis, we have evaluated and further developed commonly used estimation models for the temperature of PV modules. In this work, measurement data from two PV test sites located at Institute for Energy Technology (IFE), Kjeller, and Gålå were used. The evaluation of existing models with default values for the PV test site at Kjeller, performed in the author's specialization project, was reproduced, as it concluded that there was a clear bias for the empirical models, and thus reason to believe that parameter tuning could improve their performance. This analysis was repeated for the test site at Gålå, where similar tendencies were found. As it was shown that all models had a tendency of overestimation, and the empirical models were tuned for warmer climates, we wanted to investigate if a parameter set specifically for the Nordic climate could improve their performance.

As it was shown that the Faiman model, the Sandia Array Performance model, and the PVsyst were nearly identical models, it was decided that only the Faiman model would be brought into the parameter tuning. This was done to better be able to see the effect of adding a term accounting for the radiative loss to the sky, as in the Faiman model with a radiative term. The Faiman model with a radiative term was tuned twice, once as is, and once where the $F \cdot \epsilon$ was treated as an empirical parameter Fe available for tuning. These were then compared as three separate models, where we saw a significant improvement from the default models for all three. We also saw that the radiative term improved the performance considerably, as the Faiman model was outperformed by the two Faiman models with radiative terms. Though small differences, we saw for most modules that tuning an empirical factor Fe also improved the performance.

To study whether a general Nordic set of parameters was a reasonable choice, or if site- or module-specific parameters were necessary, they were all tuned for each model. Though the module-specific parameters generally gave a better performance, we saw that the climate- and site-specific parameters also gave a big improvement in the performance. It was also found that parameters tuned for the opposite PV test sites yielded reliable estimates, reflecting the models' potential as a general Nordic model, since it was tested on independent modules. This supports the conclusion that a general Nordic model, outperforming the default models, is a realistic outcome. To ensure a robust solution, having more test sites spread around the Nordic countries, preferably representing all the climate zones, would be a good idea.

To evaluate whether a set of parameters specifically for bifacial modules could be

beneficial, a set of parameters was tuned for each model. When testing the models, there were no evident results showing a general improvement in performance for the bifacial modules. An analysis of whether incorporating backside irradiance for the bifacial modules in the tuning and testing would improve the performance of the tuned models. There was no evident improvement found in this analysis, but this would be interesting to study further with more modules.

All parameter tuning was performed twice, for all data and for data where the nightly values have been removed. This was done to investigate the effect of removing the nightly values on daytime performance. Though small improvements to the models were seen, these were deemed negligible, and the choice of keeping or removing nightly values will not have a major effect on the daytime performance.

As we have seen that the climate-specific parameters generally perform well for all modules, the average performances of the three climate-specific models, i.e., the models tuned for both PV test sites, were compared. We found that the climate-specific Faiman model with a radiative term and an empirical parameter Fe had an improvement of up to 0.8 °C in average RMSE and 0.63 °C in average |MBE|, when compared to the climate-specific Faiman model. However, as this model requires measurements for downwelling infrared radiation from the sky, and is generally a more complex model, the Faiman model can also be a good choice.

An evaluation was also done for the DC power estimation to see the effect of improving the temperature models. When comparing the default values with tuned models, we could see a significant improvement in the power estimations. It was shown that the bias seen in the default models for a high DC power is improved significantly by the parameter tuning.

From studying the model performances for the two PV test sites, using the Faiman model with a radiative term and an empirical parameter Fe was proposed, with the following parameters: $U_0 = 27.536$ W/(m^2 °C), $U_1 = 6.705$ W/(m^2 °C(m/s)), and $Fe = 1.000$ for daytime data only, or $U_0 = 25.340$ W/(m^2 °C), $U_1 = 7.518$ W/(m^2 °C(m/s)), and $Fe = 1.000$ for all data. However, as measurements of the downwelling infrared radiation from the sky are not always available and as the radiative term adds complexity to the model, a good alternative is also to use the Faiman model with the following climate-specific parameters: $U_0 = 33.236$ W/(m^2 °C) and $U_1 = 7.120$ W/(m^2 °C(m/s)) for daytime data only, or alternatively $U_0 = 33.385$ W/(m^2 °C) and $U_1 = 7.111$ W/(m^2 °C(m/s)) for all data.

All in all, we have shown that by performing a simple parameter tuning, we can improve the performance of existing empirical models significantly. We have also seen that adding a term accounting for a radiative loss to the sky, and additionally making this an empirical term, improves the performance further. We conclude that our results support the idea that a general Nordic model can be beneficial for model performances for Nordic PV systems.

CHAPTER

SEVEN

FURTHER WORK

The aim of this thesis has been to evaluate existing temperature models for PV modules, as well as to further develop the empirical models using parameter tuning. The work has looked into a few different topics where many of which can be researched further.

As we are studying data sets from PV test sites in a Nordic climate, there will be snow cover present in the data sets. In this thesis, the days with clear snow cover were removed, as the temperature models should not account for the effect of snow. The snow days were removed by studying the relation between the irradiance and the production, as a snow cover will give a low production-to-irradiance ratio. However, the probability of this filter losing some snow days due to snow cover on the reference cells measuring the irradiance is high. Video-detection of snow cover would avoid this possible error, and should be explored for a higher certainty in the removal of snow days.

In the evaluation of module-, site-, and climate-specific parameters, one would benefit from having a larger database with more locations and more PV modules at each test site. Having more modules in each test site and more than two test sites would make it easier to see if having a site-specific set of parameters is reasonable. One could then tune module-specific parameters for all modules, and see whether the modules from the same location cluster together. If this is the case, a site-specific model would likely outperform a climate-specific model.

To investigate whether module-specific parameters could be used across different test sites, it would be interesting to have several modules of the same type at different test sites in different climate zones. If these still have similar parameters when tuned, a set of parameters could be developed for each module type, even for use in other test sites.

This thesis has investigated whether creating a parameter set specifically for bifacial modules will give a better performance, and has not shown any clear indications that this is beneficial. However, as data from only 3 modules was used, this could be a random outcome, and it would be interesting to perform this analysis again for more bifacial modules. In addition, an analysis on how incorporating the backside irradiance for the bifacial modules during tuning and testing would affect the results was performed. Again, it was difficult to draw any clear conclusions, as this analysis would benefit from more bifacial modules. These two approaches to improve the temperature estimation for bifacial modules should be investigated further with a

larger dataset.

As mentioned, to create a general set of parameters for the Nordic climate, more test sites should be included. Looking at the climate zone map in Figure 2.6.1, we see at least 5 different climate zones just in Norway, where we are now only representing two of them. If we expect a set of parameters to be suitable for all areas in the Nordic countries and areas with similar climate, these should be tuned and tested for PV test sites spread out in the Nordic countries, preferably in all climate zones. To get a reliable test for whether the climate-specific parameters work well, they should be tested for independent test sites not included in the tuning. This will give a more realistic evaluation, as it tests the model the way it will be used, i.e., on modules in locations not included in the data set. Testing the site-specific parameters on the modules from the other test site did this in principle, but it would be beneficial to repeat on a larger scale.

The model generally performing the best was the Faiman model with a radiative term and an empirical parameter Fe, which removes the tilt angle dependency of the $F\epsilon$ term, regardless of the two PV test sites having different tilt angles. It would therefore be interesting to investigate further whether the same tendencies occur when including more modules with different tilt angles, to ensure a robust model.

As this thesis has only included rack-mounted modules, it would be interesting to investigate the temperature behavior of other configurations. As an example, it would be interesting to see if roof-mounted modules could be included in a Nordic model in any way, or if a specific model or set of parameters needs to be developed. As roof-mounted modules are very common in the Nordic countries, this would be valuable to investigate.

This thesis has focused on improving model performances for PV in a Nordic climate, and has done so by tuning models using data from two PV test sites in a Nordic climate. Notably, these test sites have modern PV modules, while the systems used to tune the models' default parameters could be older modules. As an example, the Faiman model was tuned for data collected in 2006 [7]. The use of newer modules may influence temperature behavior, as the bill of materials has evolved. Therefore, it would be interesting to investigate whether the parameters proposed in this work could also improve model performance for modern PV systems in warmer climates.

REFERENCES

[1] World Meteorological Organization (WMO). "State of the Global Climate 2024". In: (2024). URL: https://library.wmo.int/idurl/4/69455.

[2] United Nations (UN). "Renewable energy - powering a safer future". In: (n.d.). URL: https://www.un.org/en/climatechange/raising-ambition/renewable-energy.

[3] International Energy Agency (IEA). "Renewables 2024 - Analysis and forecast to 2030". In: (Oct. 2024). URL: https://www.iea.org/reports/renewables-2024.

[4] Norges vassdrag- og energidirektorat (NVE). "NVEs svar på oppdrag on solkraft og annen lokal energiproduksjon". In: (Feb. 2024). URL: https://www.nve.no/media/16752/notatet-nves-svar-paa-oppdrag-om-solkraft-og-annen-lokal-energiproduksjon.pdf.

[5] Norges vassdrag- og energidirektorat (NVE). "Oversikt over solkraft i Norge". In: (May 2025). URL: https://www.nve.no/energi/energisystem/solkraft/oversikt-over-solkraftanlegg-i-norge/.

[6] E. D. Aranda et al. "Measuring the I-V curve of PV generators". In: *IEEE Industrial Electronics Magazine* 9 (Sept. 2009), pp. 4–14. DOI: https://doi.org/10.1109/MIE.2009.933882.

[7] D. Faiman. "*Assessing the Outdoor Operating Temperature of Photovoltaic Modules*". In: *Progress in Photovoltaics: Research and Applications* 16 (Feb. 2008), pp. 307–315. DOI: https://doi.org/10.1002/pip.813.

[8] M. Kottek et al. "World Map of the Köppen-Geiger climate classification updated". In: *Metrologische Zetschrift* 15 (3 2006), pp. 259–263. DOI: https://doi.org/10.1127/0941-2948/2006/0130.

[9] World Bank Group. "Norway". In: *Climate Change Knowledge Portal* (2021). URL: https://climateknowledgeportal.worldbank.org/country/norway.

[10] T. A. Finstad. "Modeling of temperature for mono- and bifacial photovoltaics in Nordic conditions". In: *Project thesis, Norwegian University of Science and Technology (NTNU), Available from author upon request* (Dec. 2024).

[11] J. Nelson. *The Physics of Solar Cells*. Imperial College Press, 2003, pp. 1–16.

[12] T. W. Reenaas, S. E. Foss, and E. S. Marstein. "Solceller". In: *Naturen* 133 (6 Jan. 2010), pp. 280–290. DOI: https://doi.org/10.18261/ISSN1504-3118-2009-06-02.

[13] T. Dullweber and J. Schmidt. "Industrial Silicon Solar Cells Applying the Passivated Emitter and Rear Cell (PERC) Concept - A Review". In: *IEEE Journal of Photovoltaics* 6 (Sept. 2016), pp. 1366–1381. DOI: https://doi.org/10.1109/JPHOTOV.2016.2571627.

[14] Solar Magazine. "A Complete Guide to PERC Solar Panels (vs. Other Techs)". In: *Solar Panels* (Mar. 2022). URL: https://solarmagazine.com/solar-panels/perc-solar-panels/ (visited on 12/15/2024).

[15] Solar Magazine. "IBC Solar Cells: Definition, Benefits, vs. Similar Techs". In: *Solar Panels* (Apr. 2022). URL: https://solarmagazine.com/solar-panels/ibc-solar-cells/ (visited on 12/15/2024).

[16] T. Mishima et al. "Develioment status of high-efficiency HIT solar cells". In: *Solar Energy Materials and Solar Cells* 95 (1 Jan. 2011), pp. 18–21. DOI: https://doi.org/10.1016/j.solmat.2010.04.030.

[17] B. Marion et al. "A Practical Irradiance Model for Bifacial PV Modules". In: *2017 IEEE 44th Photovoltaic Specialist Conference (PVSC)* (2017). DOI: https://doi.org/10.1109/PVSC.2017.8366263.

[18] VDMA. "International Technology Roadmap for Photovoltaics (ITRPV)". In: *Photovoltaic Equipment* (May 2024). URL: https://www.qualenergia.it/wp-content/uploads/2024/06/ITRPV-15th-Edition-2024-2.pdf.

[19] J. Schneider et al. "Half-cell solar modules: The new standard in PV production?" In: *Photovoltaics International* (2019). URL: https://publica.fraunhofer.de/entities/publication/3d38a6a0-3887-4c61-9a2c-dab07aa8046a.

[20] I. Santiago et al. "Modeling og photovoltaic cell temperature losses: A review and a practice case in South Spain". In: *Renewable and Sustainable Energy Reviews* 90 (July 2018), pp. 70–89. DOI: https://doi.org/10.1016/j.rser.2018.03.054.

[21] Z. Zhang et al. "*The mathematical and experimental analysis on the steady-state operating temperature of bifacial photovoltaic modules*". In: *Renewable Energy* 155 (Mar. 2020), pp. 658–668. DOI: https://doi.org/10.1016/j.renene.2020.03.121.

[22] PVsyst SA. "Array thermal Loses". In: *PVsyst 7 Help* (1994-2022). URL: https://www.pvsyst.com/help-pvsyst7/index.html?array_losses.htm.

[23] PVlib. "PV temperature models". In: *PVlib* (n.d.). URL: https://pvlib-python.readthedocs.io/en/stable/reference/pv_modeling/temperature.html (visited on 12/12/2024).

[24] J. A. Ruiz-Arias and C. A. Gueymard. "High Concentrator Photovoltaics". In: Springer, Feb. 2015. Chap. Solar Resource for High-Concentrator Photovoltaic Applications. DOI: https://doi.org/10.1007/978-3-319-15039-0_10.

[25] A. K. Soteris. "Chapter 2 - Environmental Characteristics". In: *Solar Energy Engineering (Second Edition)* (2014), pp. 51–123. DOI: https://doi.org/10.1016/B978-0-12-397270-5.00002-9.

[26] U. Schumann. *Atmospheric Physics*. Springer, 2012. DOI: 10.1007/978-3-642-30183-4.

[27] A. Lahiri. *Basic Optics - Principles and Concepts*. Elsevier, 2016. ISBN: 978-0-12-805357-7. DOI: https://doi.org/10.1016/C2015-0-04613-5.

[28] National Renewable Energy Laboratory (NREL). "Solar Resource Glossary". In: (Mar. 2025). URL: https://www.nrel.gov/grid/solar-resource/solar-glossary.

[29] J. A. Coakley. "Reflectance and Albedo, Surface". In: *Encyclopedia of atmospheric sciences* 12 (2003), pp. 1914–1923. URL: http://evasion.imag.fr/~Fabrice.Neyret/images/fluids-nuages/waves/Jonathan/articlesPhysique/Reflectance_Albedo_Surface.pdf.

[30] R. Tapakis and A. G. Charalambides. "Enhanced values of global irradiance due to the presence of clouds in Eastern Mediterranean". In: *Renewable Energy* 62 (Feb. 2014), pp. 459–467. DOI: https://doi.org/10.1016/j.renene.2013.08.001.

[31] P. Kosmopoulos. "Solar irradiance and exploitation of the Sun's power". In: *Planning and Management of Solar Power from Space* (2024), pp. 1–20. DOI: https://doi.org/10.1016/B978-0-12-823390-0.00006-5.

[32] M. J. Reno, C. W. Hansen, and J. S. Stein. "Global Horizontal Irradiance Clear Sky Models: Implementation and Analysis". In: *Sandia report* (Mar. 2012). DOI: https://doi.org/10.2172/1039404.

[33] Sandia National Laboratiories. "pvlib.irradiance.clearsky$_i$*ndex*". In: *PVlib documentation* (2023). URL: https://pvlib-python.readthedocs.io/en/stable/reference/generated/pvlib.irradiance.clearsky_index.html#pvlib.irradiance.clearsky_index.

[34] R. Marquez and C. F. M. Coimbra. "A novel metric for evaluation of solar forecasting models". In: *Journal of Solar Energy Engineering* 135 (2011). DOI: http://dx.doi.org/10.1115/ES2011-54519.

[35] D. L. King, W. E. Boyson, and J. A. Kratochvil. "*Photovoltaic Array Performance Model*". In: *Sandia Report* (Aug. 2004). DOI: https://doi.org/10.2172/919131.

[36] A. Driesse, J. S. Stein, and M. Theristis. "*Improving Common PV Module Temperature Models by Incorporating Radiative Losses to the Sky*". In: *Sandia Report* (Aug. 2022). DOI: https://doi.org/10.2172/1884890.

[37] M. K. Fuentes. "*A Simplified Thermal Model for Flat-Plate Photovoltaic Arrays*". In: *Sandia Report* (May 1987).

[38] A. P. Dobos. "*PVWatts Version 5 Manual*". In: (Sept. 2014). DOI: https://doi.org/10.2172/1158421.

[39] PVsyst SA. "Validations on old versions of PVsyst". In: *PVsyst 7 Help* (n.d.). URL: https://www.pvsyst.com/help-pvsyst7/validations_oldsystems.htm.

[40] R. G. Jr. Ross. "Design Techniques for Flat-Plate Photovoltaic Arrays". In: *The conference record of the 15th IEEE Photovoltaics Specialist Conference 1981, Orlando, FL* (May 1981).

[41] A. Driesse and J. Polo. "PV module operating temperature: Reliable extraction of model parameters from dynamic field data". In: *41st European Photovoltaic Solar Energy Conference and Exhibition* (Sept. 2024). DOI: http://dx.doi.org/10.4229/EUPVSEC2024/4BO.6.6.

[42] A. Driesse, M. Theristis, and J. S. Stein. "PV Module Operating Temperature Model Equivalence and Parameter Translation". In: *2022 IEEE 49th Photovoltaics Specialists Conference (PVSC)* (2022), pp. 172–177. DOI: https://doi.org/10.1109/PVSC48317.2022.9938895.

[43] A. P. Dobos. "PVWatts Version 5 Manual". In: (Sept. 2014). URL: https://pvwatts.nrel.gov/downloads/pvwattsv5.pdf.

[44] M. C. Peel, B. L. Finlayson, and T. A. McMahon. "Updated world map of the Köppen-Geiger climate classification". In: *Hydrology and Earth System Sciences* 11 (2007), pp. 1633–1644. DOI: https://doi.org/10.5194/hess-11-1633-2007.

[45] M. M. Nygård et al. "Elucidating uncertainty in bifacial photovoltaic gain estimation". In: *Solar Energy* 292 (May 2025). DOI: https://doi.org/10.1016/j.solener.2025.113469.

[46] Meteocontrol. "Temperature". In: *Meteocontrol* (n.d.). URL: https://www.meteocontrol.com/en/photovoltaic-monitoring/accessories/sensors/temperature-sensors (visited on 12/14/2024).

[47] Meteocontrol. "Irradiance". In: *Meteocontrol* (n.d.). URL: https://www.meteocontrol.com/en/photovoltaic-monitoring/accessories/sensors/irradiance-sensors (visited on 12/14/2024).

[48] Lufft. "WS500-UMB Smart Weather Sensor". In: *Products* (n.d.). URL: https://www.lufft.com/products/compact-weather-sensors-293/ws500-umb-smart-weather-sensor-1842/ (visited on 12/07/2024).

[49] M. B. Øgaard. *Personal communication with supervisor*. 2025.

[50] SoliTek. "SoliTek Standard M.60-W-365". Datasheet - Mono PERC C. n.d.

[51] SoliTek. "Blackstar Solid Framed Glass/Glass". Datasheet - Bifacial PERC C. n.d.

[52] PV-Blocks. "Si-mV-85 Irradiance Sensor". In: (n.d.). URL: https://www.pvblocks.com/product/si-mv-85-irradiance-sensor/.

[53] EKO Instruments. "MS-80S Pyranometer". In: (n.d.). URL: https://www.eko-instruments.com/media/c2yaig50/ps-eko-ms80s-23-03e_v010.pdf.

[54] NRGSystems. "NRG 40 Anemometer Technical product sheet". In: (July 2020). URL: https://www.nrgsystems.com/assets/resources/NRG-40-Tech-Product-Sheet-2020-V1.pdf.

[55] Campbell Scientific. "HygroVue5". In: (Jan. 2024). URL: https://s.campbellsci.com/documents/us/product-brochures/b_hygrovue5.pdf.

[56] RS Pro. "RS PRO 3 wire PT100 Sensor". In: *Platinum Resistance Temperature Sensors* (). URL: https://docs.rs-online.com/f78d/A700000008848976.pdf.

[57] PVlib. “API Reference - Quality”. In: *PVAnalytics* (n.d.). URL: https://pvanalytics.readthedocs.io/en/stable/api.html (visited on 12/12/2024).

[58] NumPy Developers. “numpy.allclose”. In: (2024). URL: https://numpy.org/doc/2.1/reference/generated/numpy.allclose.html (visited on 05/28/2025).

[59] Norwegian Meteorological Institute. “Historikk - Kjeller”. In: *Yr* (n.d.). URL: https://www.yr.no/nb/historikk/tabell/5-4200/Norge/Akershus/Lillestr%C3%B8m/Kjeller?q=2022 (visited on 09/06/2024).

[60] K. Anderson et al. “pvlib python: 2023 project update”. In: *Journal of Open Source Software* (2023). DOI: https://doi.org/10.21105/joss.05994.

[61] PVlib. “pvlib.location.Location.get$_c$*learsky*”. In: *PVlib* (n.d.). URL: https://pvlib-python.readthedocs.io/en/stable/reference/generated/pvlib.location.Location.get_clearsky.html (visited on 12/12/2024).

[62] S. Zhan and A. Chong. “Data requirements and performance evaluation of model predictive control in buildings: A modeling perspective”. In: *Renewable and Sustainable Energy Reviews* 142 (May 2021). DOI: https://doi.org/10.1016/j.rser.2021.110835.

[63] J. H. Friedman. *The Elements of Statistical Learning: Data Mining Inference and Prediction*. Springer, 2017.

[64] SciPy. “Optimization and root finding (scipy.optimize)”. In: *SciPy API* (n.d.). URL: https://docs.scipy.org/doc/scipy/reference/optimize.html.

[65] M. Mussard et al. “Influence of Temperature Coefficient and Sensor Choice on PV System Performance”. In: *IEEE Journal of Photovoltaics* 13 (Nov. 2023), pp. 920–928. DOI: https://doi.org/10.1109/JPHOTOV.2023.3311896.

[66] SeNorge. “Nysnø og regn”. In: (2025). URL: https://senorge.no/.

[67] K. S. Hayibo et al. “Monofacial vs bifacial solar photovoltaic systems in snowy environments”. In: *Renewable energy* 193 (June 2022), pp. 657–668. DOI: https://doi.org/10.1016/j.renene.2022.05.050.

[68] N. Roosloot. “Comparison of humidity-induced stress levels between floating and ground-mounted photovoltaics”. Manuscript in preparation. 2025.

[69] M. M. Nygård. *Personal communication with supervisor*. 2025.

APPENDICES

A - GITHUB REPOSITORY

Relevant code used in this document is included in the Github repository linked below.

Github repository link

- `https://github.com/toneaf/MasterThesis`

Relevant code used in the project thesis [10], which is often referred to, is included in the following Github repository.

Github repository link

- `https://github.com/toneaf/ProjectThesis`

B.1 Model performance time series

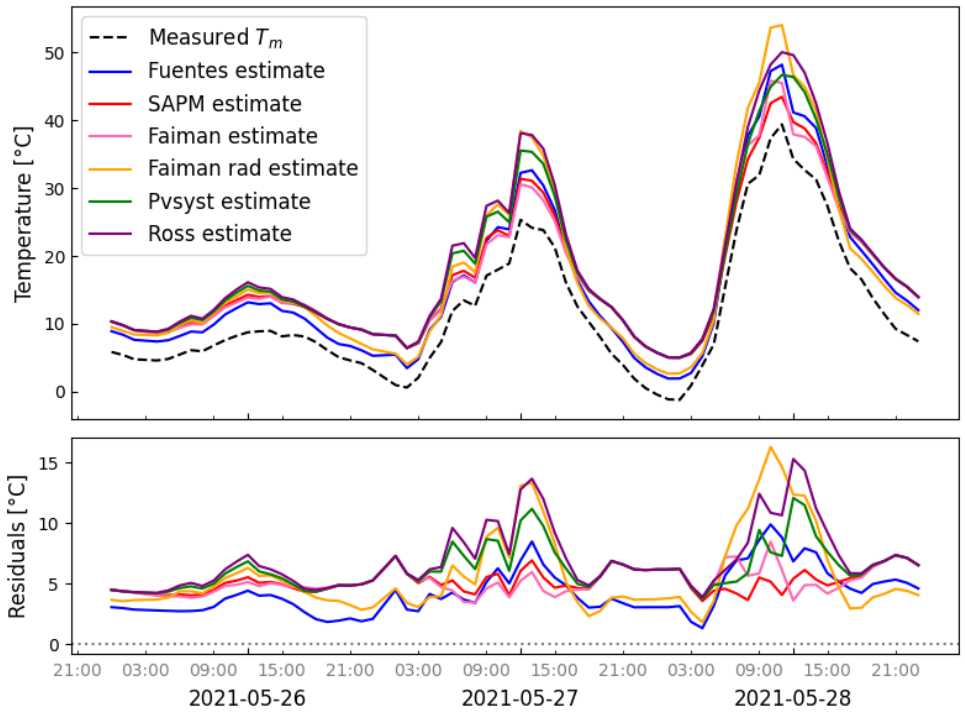

Figure B.1: Comparison of the measured module temperature and the model estimates for module Mono PERC B. The lower section shows the residuals. Taken from [10].

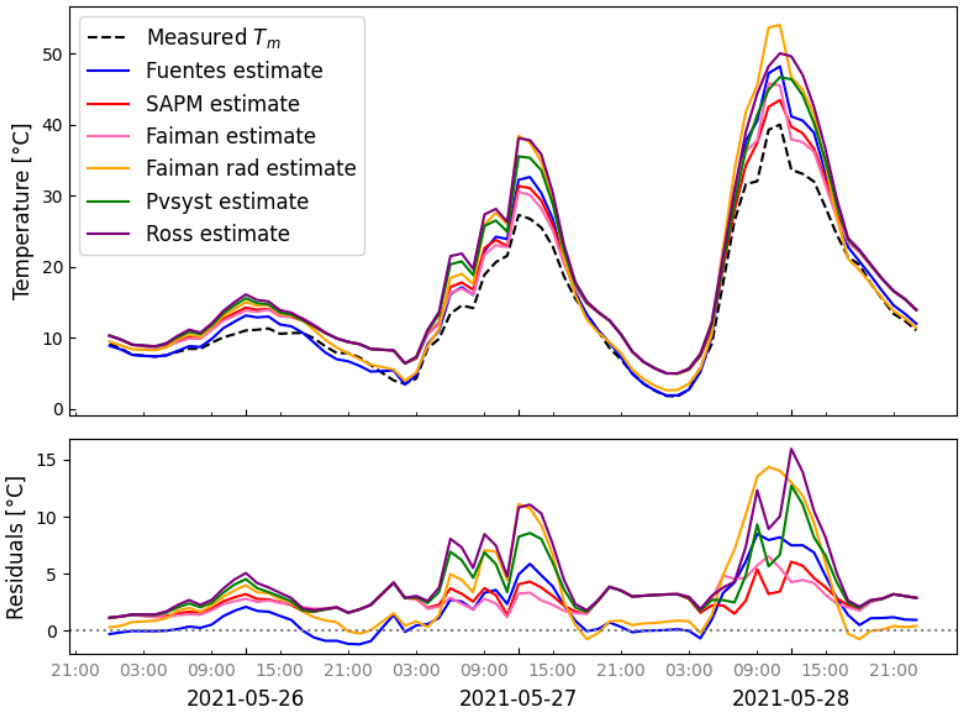

Figure B.2: Comparison of the measured module temperature and the model estimates for module Mono IBC. The lower section shows the residuals. Taken from [10].

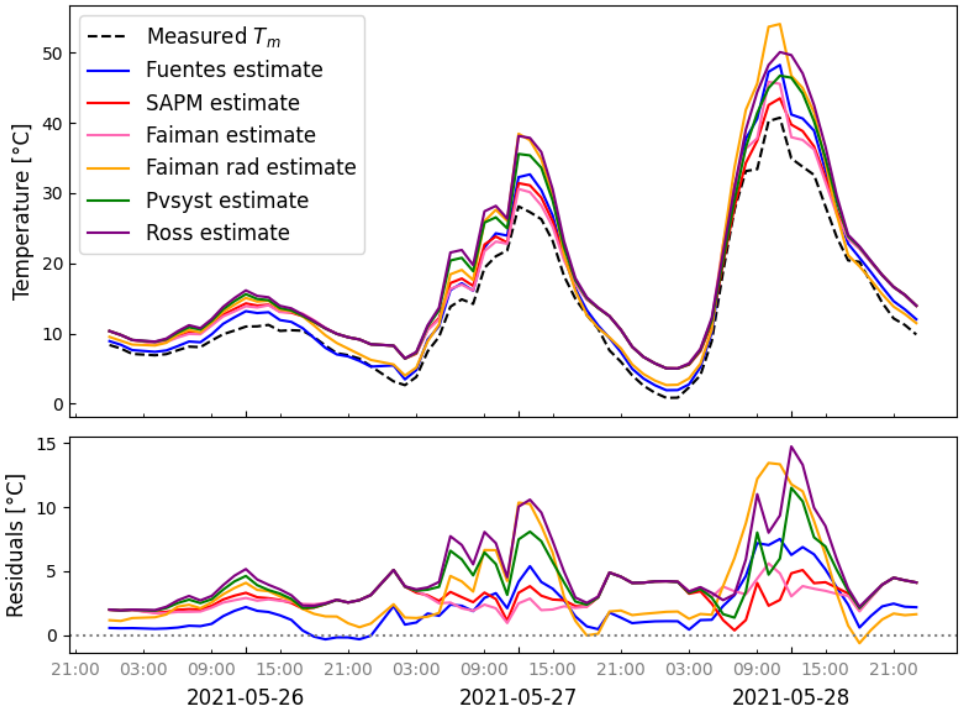

Figure B.3: Comparison of the measured module temperature and the model estimates for module Mono HIT. The lower section shows the residuals. Taken from [10].

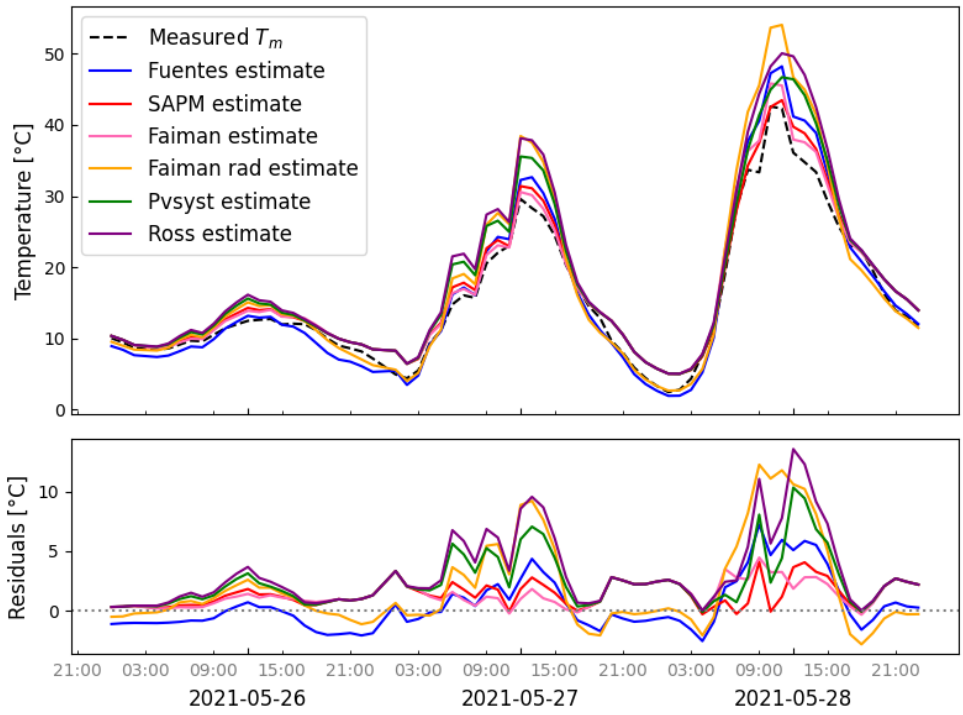

Figure B.4: Comparison of the measured module temperature and the model estimates for module Bifacial PERC B. The lower section shows the residuals. Taken from [10].

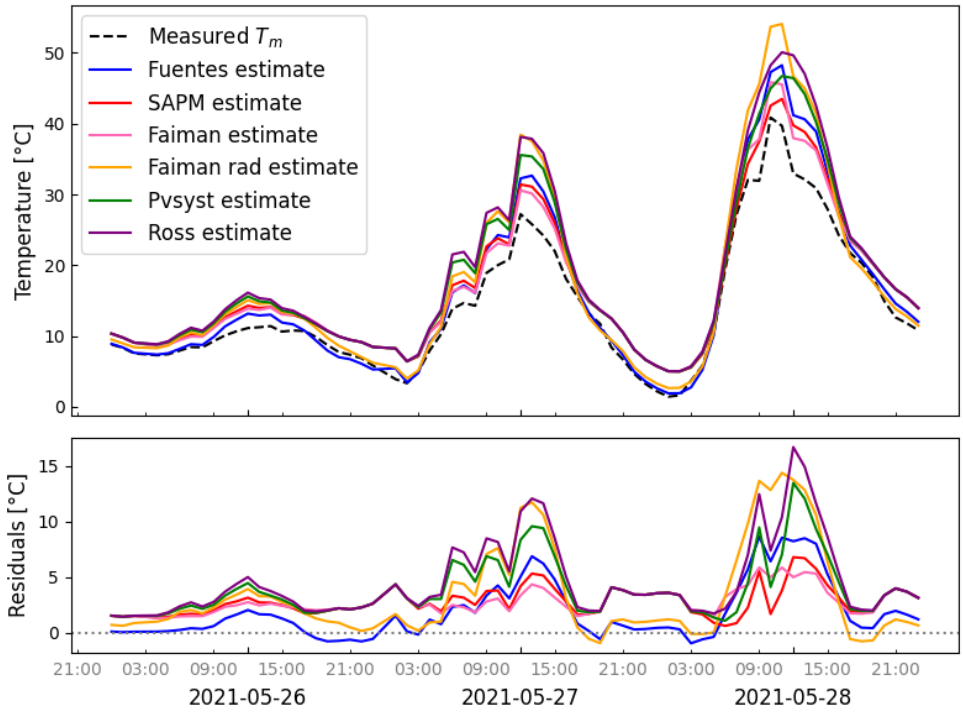

Figure B.5: Comparison of the measured module temperature and the model estimates for module Bifacial PERC A. The lower section shows the residuals. Taken from [10].

B.2 Model comparison with all models

B.2.1 Tuning evaluation on all data

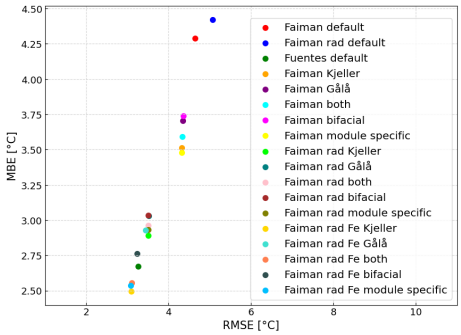

(a) Mono PERC A

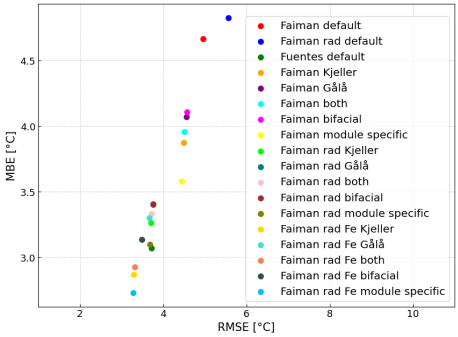

(b) Mono PERC B

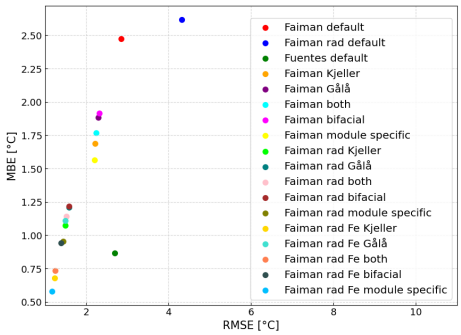

(c) Mono IBC

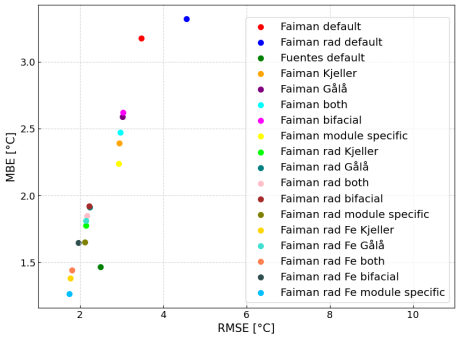

(d) Mono HIT

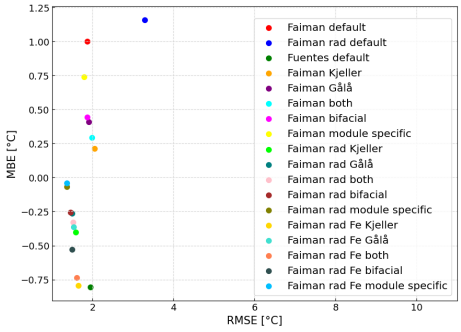

(e) Bifacial PERC A

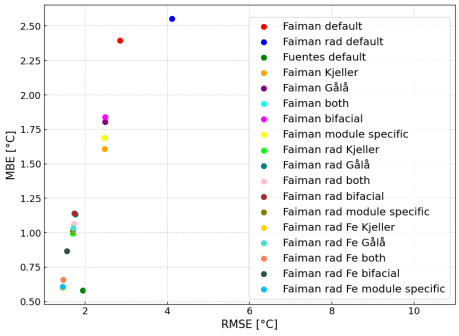

(f) Bifacial PERC B

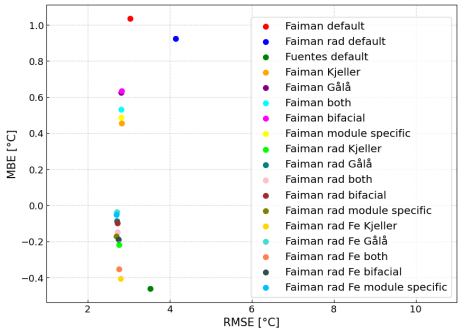

(g) Bifacial PERC C

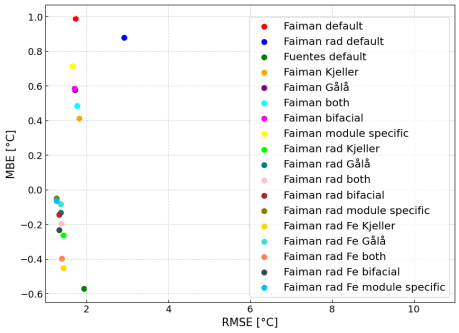

(h) Mono PERC C

Figure B.1: The RMSE and MBE of the different models for all modules at the PV test sites at Kjeller and Gålå. The models tested are the Fuentes model, Faiman model, Faiman model with a radiative term (denoted Faiman rad), tuned versions of the Faiman model, and tuned versions of the Faiman model with a radiative term.

B.2.2 Evaluating models on daytime data

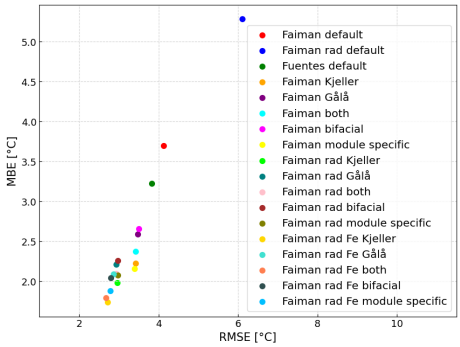

(a) Mono PERC A

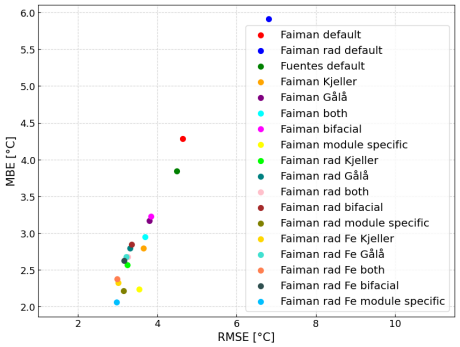

(b) Mono PERC B

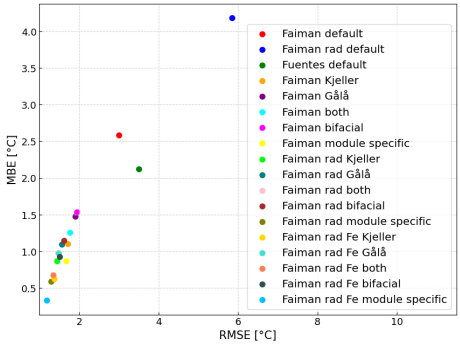

(c) Mono IBC

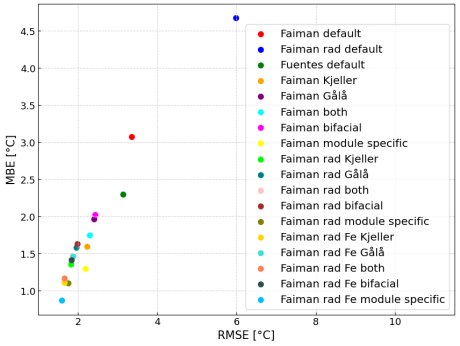

(d) Mono HIT

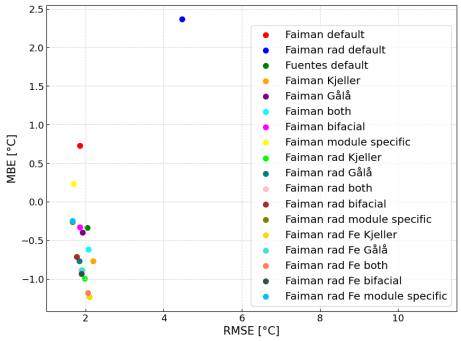

(e) Bifacial PERC A

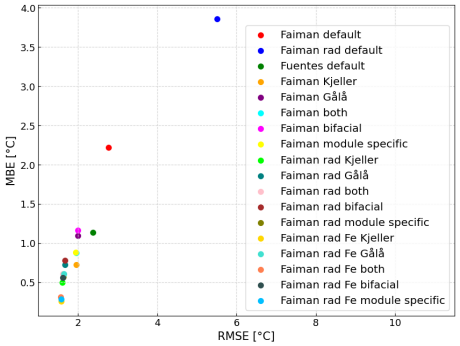

(f) Bifacial PERC B

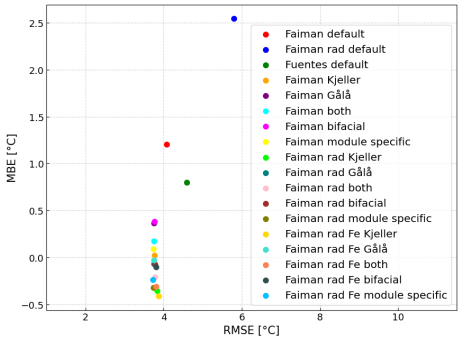

(g) Bifacial PERC C

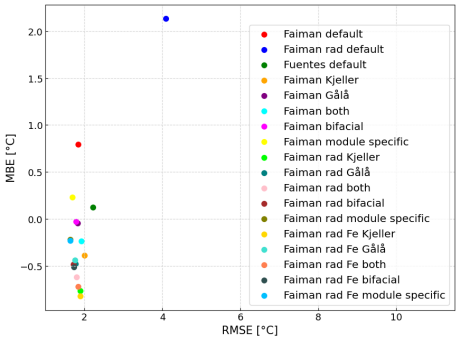

(h) Mono PERC C

Figure B.2: The RMSE and MBE of the different models for all modules at the PV test sites at Kjeller and Gålå. The models tested are the Fuentes model, Faiman model, Faiman model with a radiative term (denoted Faiman rad), tuned versions of the Faiman model, and tuned versions of the Faiman model with a radiative term. Tuned for all the data.

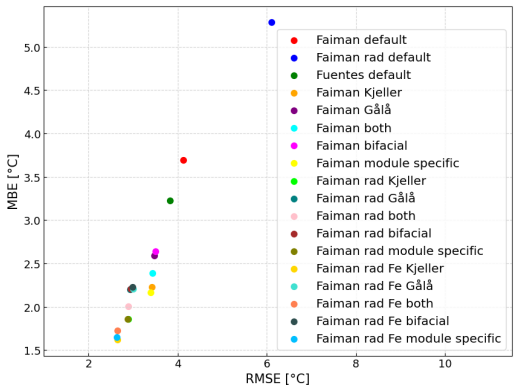

(a) Mono PERC A Kjeller

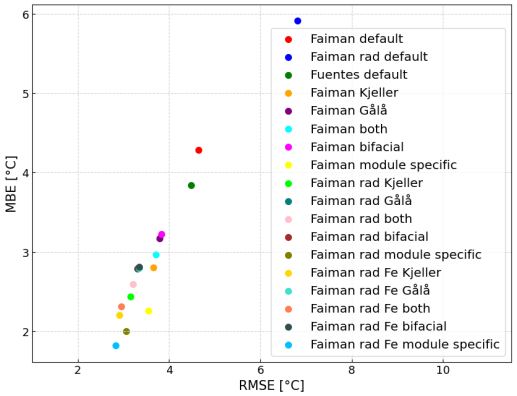

(b) Mono PERC B Kjeller

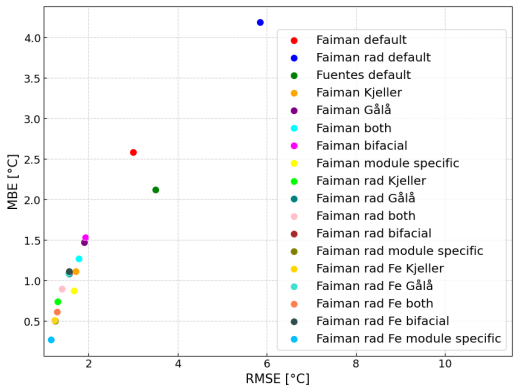

(c) Mono IBC Kjeller

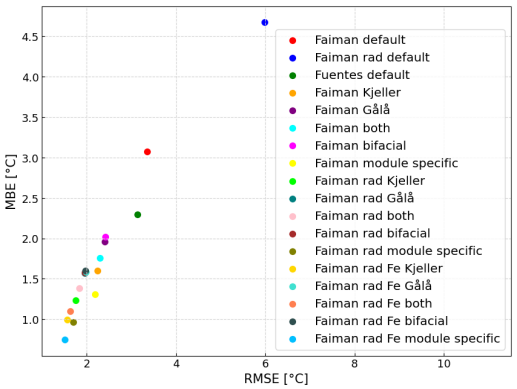

(d) Mono HIT Kjeller

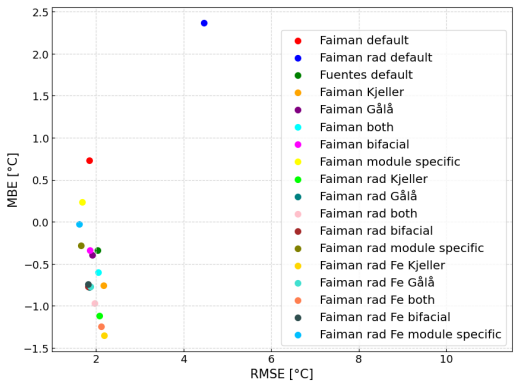

(e) Bifacial PERC A Kjeller

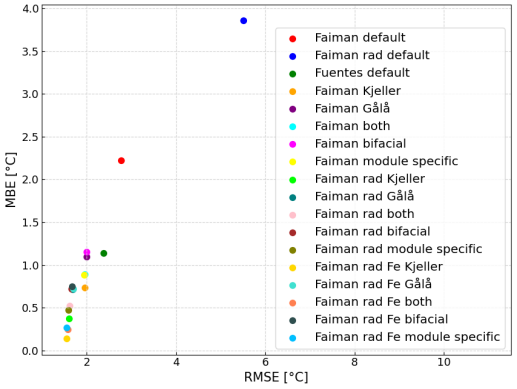

(f) Bifacial PERC B Kjeller

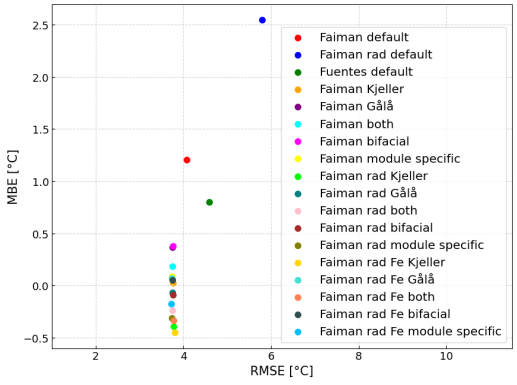

(g) Bifacial PERC C

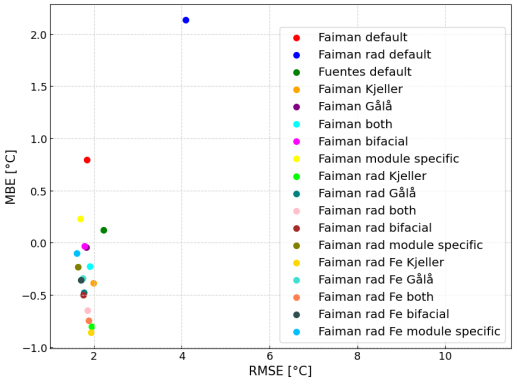

(h) Mono PERC C

Figure B.3: The RMSE and MBE of the different models for all modules at the PV test sites at Kjeller and Gålå. The models tested are the Fuentes model, Faiman model, Faiman model with a radiative term (denoted Faiman rad), tuned versions of the Faiman model, and tuned versions of the Faiman model with a radiative term. The models are tuned for daytime data.

B.3 Comparison between the different models tuned and tested for all data

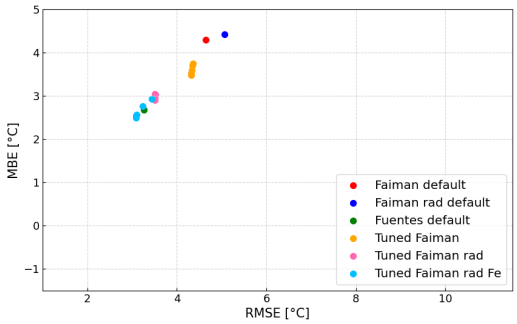

(a) Mono PERC A (Kjeller)

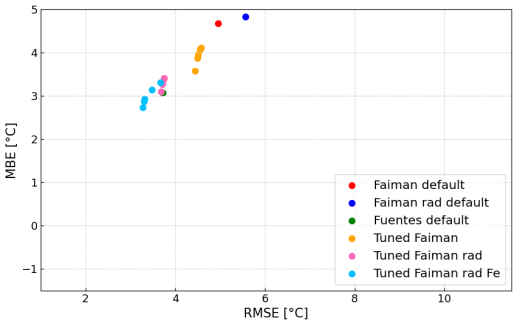

(b) Mono PERC B (Kjeller)

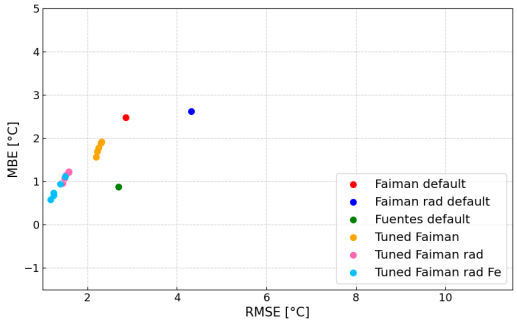

(c) Mono IBC (Kjeller)

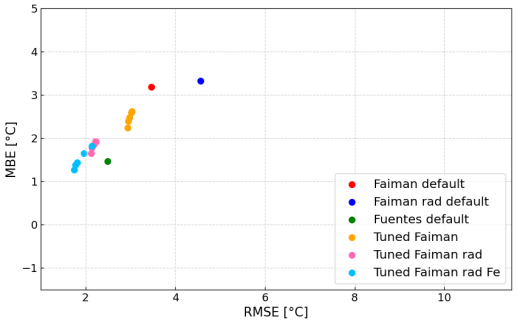

(d) Mono HIT (Kjeller)

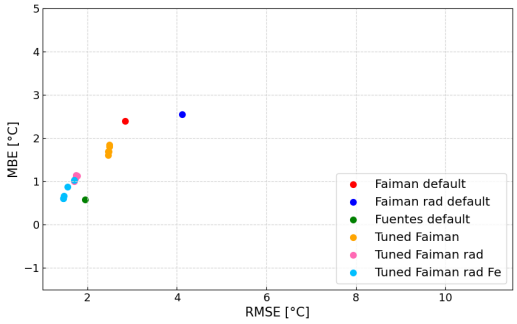

(e) Bifacial PERC A (Kjeller)

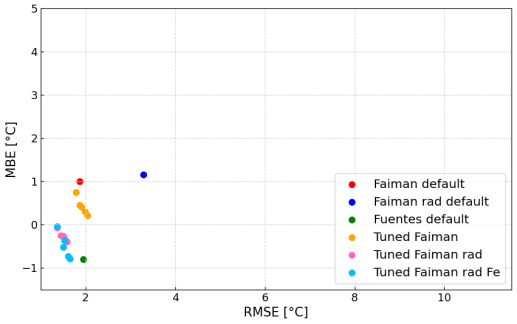

(f) Bifacial PERC B (Kjeller)

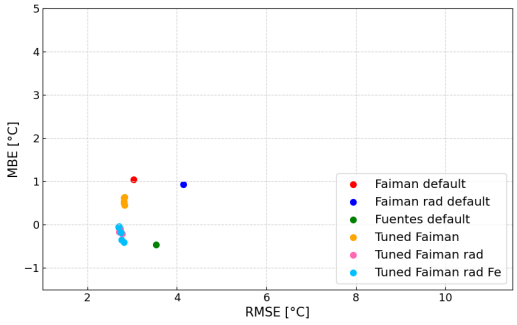

(g) Bifacial PERC C (Gålå)

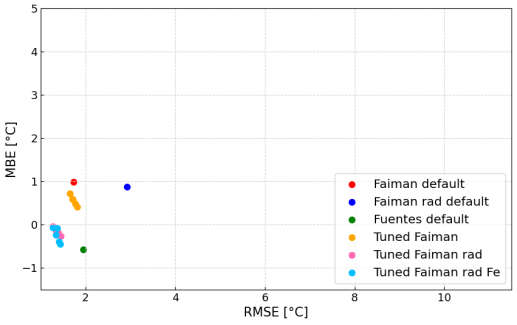

(h) Mono PERC C (Gålå)

Figure B.1: All tuned models are plotted together, where their color indicates which model they are tuned versions of. The performances displayed here are for models tuned and tested for all data. The Faiman model with a radiative term is denoted by Faiman rad, and the Faiman model with a radiative term and an empirical parameter Fe is denoted by Faiman rad Fe.

B.4 Parameters from tuning with rear-side irradiace for bifacial modules

Table B.1: Resulting model parameters (U_0, U_1) for the Faiman model from the parameter tuning using all data and daytime-only data (Irradiance > 5 W/m^2). During the tuning the rear-side irradiance is included for the bifacial modules.

Data set	**All data**		**Daytime only**	
	U_0	U_1	U_0	U_1
Kjeller	34.479	8.396	34.506	8.371
Gålå	35.665	7.169	35.657	7.170
All modules	35.293	7.725	35.389	7.625
Bifacial	35.085	8.406	36.071	8.151
Mono PERC A	36.821	6.351	36.577	6.429
Mono PERC B	39.433	7.440	38.775	7.653
Mono IBC	33.780	8.640	33.456	8.756
Mono HIT	33.470	9.076	33.021	9.237
Bifacial PERC A	35.226	9.831	35.142	9.862
Bifacial PERC B	31.107	8.254	31.067	8.269
Bifacial PERC C	44.926	6.165	44.919	6.166
Mono PERC C	27.031	7.847	27.024	7.848

Table B.2: Resulting model parameters (U_0, U_1) for the Faiman model with a radiative term from the parameter tuning using all data and daytime-only data (Irradiance > 5 W/m^2). During the tuning the rear-side irradiance is included for the bifacial modules.

Data set	**All data**		**Daytime only**	
	U_0	U_1	U_0	U_1
Kjeller	26.096	9.634	29.457	8.310
Gålå	31.137	6.920	31.559	6.788
All modules	28.646	8.205	30.823	7.382
Bifacial	30.372	8.358	31.790	7.908
Mono PERC A	23.607	9.226	30.683	6.569
Mono PERC B	23.766	11.021	32.128	7.827
Mono IBC	25.586	9.786	28.764	8.547
Mono HIT	22.636	11.208	27.786	9.148
Bifacial PERC A	29.506	10.064	30.320	9.752
Bifacial PERC B	27.144	8.152	27.378	8.060
Bifacial PERC C	39.621	6.052	39.975	5.926
Mono PERC C	23.278	7.445	23.621	7.344

Table B.3: Resulting model parameters for the Faiman model with a radiative term from the parameter tuning using all data and daytime-only data (Irradiance $>$ 5 W/m^2). Here, the $Fe\epsilon$ is treated as an empirical parameter Fe, and tuned. During the tuning the rear-side irradiance is included for the bifacial modules.

Data set	**All data**			**Daytime only**		
	U_0	U_1	Fe	U_0	U_1	Fe
Kjeller	24.143	9.562	1.000	27.710	8.138	1.000
Gålå	31.016	6.893	0.832	31.990	6.837	0.698
All modules	27.140	8.125	1.000	29.376	7.271	1.000
Bifacial	29.089	8.161	1.000	30.368	7.768	1.000
Mono PERC A	20.588	9.553	1.000	28.585	6.494	1.000
Mono PERC B	20.000	11.572	1.000	29.721	7.763	1.000
Mono IBC	24.812	9.231	1.000	27.301	8.264	1.000
Mono HIT	21.055	10.929	1.000	26.082	8.919	1.000
Bifacial PERC A	27.768	9.895	1.000	28.581	9.580	1.000
Bifacial PERC B	26.513	8.017	0.855	26.897	7.996	0.797
Bifacial PERC C	39.234	6.004	0.888	38.895	5.852	0.992
Mono PERC C	23.259	7.436	0.802	24.333	7.472	0.602

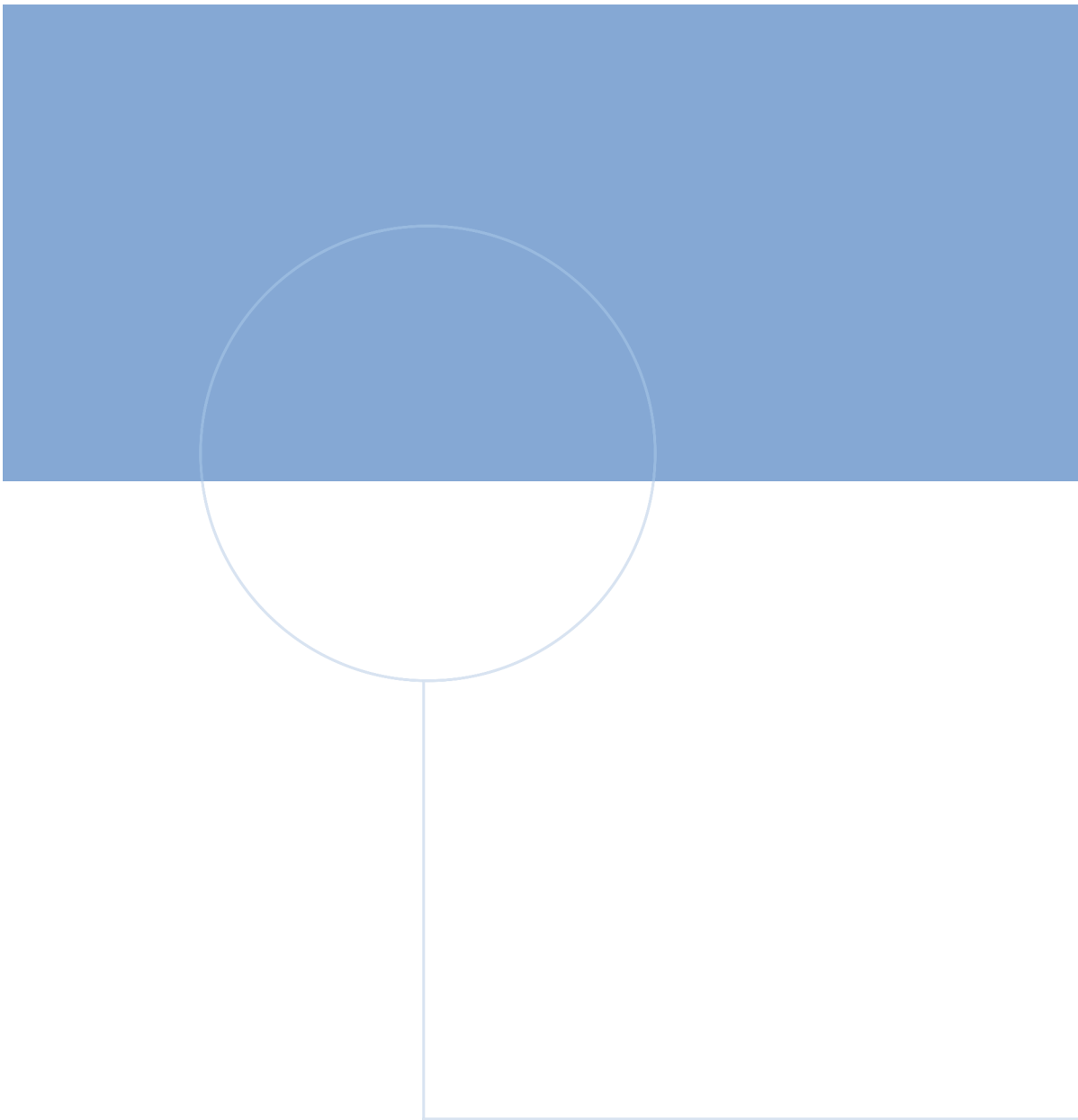

NTNU
Norwegian University of
Science and Technology

IFE Institute for
Energy Technology